



**KTH Information and
Communication Technology**

**Micromachined Epitaxial Colossal Magnetoresistors
for Uncooled Infrared Bolometer**

**Doctoral Thesis by
Joo-Hyung Kim**

Condensed Matter Physics, Laboratory of Solid State Devices
Department of Microelectronics and Information Technology
School of Information and Communication Technology
Royal Institute of Technology (KTH)

Stockholm 2005

Micromachined Epitaxial Colossal Magnetoresistors for Uncooled Infrared Bolometer

A dissertation submitted to Royal Institute of Technology (Kungliga Tekniska Högskolan, KTH), Kista-Stockholm, Sweden, in partial fulfillment of the requirements for the degree of Doctor of Philosophy. The public defense will take place at December 9, 2005 in C1, Electrum, Isafjordsgatan 22, Kista, Sweden.

ISRN KTH/EKT/FR-2005/5-SE

ISSN 1650-8599

TRITA-EKT

Forskningsrapport 2005:5

© Joo-Hyung Kim, November 2005

Royal Institute of Technology (KTH, Kungliga Tekniska Högskolan)

Department of Microelectronics and Information Technology

Electrum 229,

S-164 40, Kista-Stockholm

SWEDEN

Printed by Universitetsservice US AB, Kista-Stockholm 2005

Cover figure: Structural, stoichiometric, electrical and noise characterization results of heteroepitaxial $\text{La}_{0.67}(\text{Sr,Ca})_{0.33}\text{MnO}_3$ (LSCMO) films grown on $\text{Bi}_4\text{Ti}_3\text{O}_{12}/\text{CeO}_2/\text{YSZ}$ buffered silicon substrates and scanning electron microscopy (SEM) images of self-supported LSCMO membranes.

To my family for endless encourage, love and supports.....

Abstract

High quality perovskite manganites, $\text{La}_{1-x}\text{A}_x\text{MnO}_3$ ($A = \text{Ca}, \text{Sr}, \text{Ba}$) are very attractive materials due to their great application potential for magnetic memory, uncooled infrared (IR) microbolometer and spintronics devices. This thesis presents studies of the growth and material characterization (including structural, electrical, magnetic and noise) of epitaxial manganite films on Si and GaAs. Furthermore, investigations about strain effect on structural and electrical properties of manganites, and finally fabrication of self-supported free standing microstructures for uncooled IR bolometer are also demonstrated.

To obtain high quality epitaxial manganite films on semiconductor substrates at room temperature, using a combination of $\text{La}_{0.67}\text{Sr}_{0.33}\text{MnO}_3$ (LSMO) and $\text{La}_{0.67}\text{Ca}_{0.33}\text{MnO}_3$ (LCMO) compounds, $\text{La}_{0.67}(\text{Sr},\text{Ca})_{0.33}\text{MnO}_3$ (LSCMO) films were successfully grown on Si substrates with $\text{Bi}_4\text{Ti}_3\text{O}_{12}$ (BTO)/ CeO_2 /YSZ buffers by pulsed laser deposition (PLD) technique. Crystallographic relations between layers shows *cube-on-cube* for BTO/ CeO_2 /YSZ/Si and *diagonal-on-side* for LSCMO films on BTO layer. $4.4\% \text{K}^{-1}$ maximum temperature coefficient of resistivity ($\text{TCR} = 1/\rho \cdot d\rho/dT$) and $2.9\% \text{kOe}^{-1}$ colossal magnetoresistance (CMR) were obtained at room temperature. Assuming of a prototype of temperature sensor, $1.2\text{ }\mu\text{K}/\sqrt{\text{Hz}}$ of noise equivalent temperature difference (NETD) and $2.9 \times 10^8\text{ cm}\sqrt{\text{Hz}}/\text{W}$ of detectivity are expected to achieve at 294 K, 30 Hz. For GaAs substrates, using MgO buffer layer, LCMO films shows $9.0\% \text{K}^{-1}$ of TCR at 223 K while LSMO exhibits $2\% \text{K}^{-1}$ at 327 K.

Systematic strain effects on structural and electrical properties of $\text{La}_{0.75}\text{Sr}_{0.25}\text{MnO}_3$ (LSMO) films on BTO/ CeO_2 /YSZ-buffered Si, $\text{Si}_{1-x}\text{Ge}_x/\text{Si}$ (compressive strain, $x = 0.05\text{-}0.20$) and $\text{Si}_{1-y}\text{C}_y/\text{Si}$ (tensile, $y = 0.01$) were investigated. The strain induced from $\text{Si}_{1-x}\text{Ge}_x/\text{Si}$ and $\text{Si}_{0.99}\text{C}_{0.01}/\text{Si}$ has a tendency to decrease the roughness of CMR films compared to Si sample. High resistivity and low TCR values are observed for $\text{Si}_{0.8}\text{Ge}_{0.2}/\text{Si}$ and $\text{Si}_{0.99}\text{C}_{0.01}/\text{Si}$ samples due to excessive strains whereas $\text{Si}_{0.9}\text{Ge}_{0.1}/\text{Si}$ and $\text{Si}_{0.95}\text{Ge}_{0.05}/\text{Si}$ show slight improvements of films quality and TCR value.

To fabricate LSCMO manganite bolometer on Si, wet etching with KOH and BHF and dry etching methods with Ar ion beam etching (IBE) were studied. For KOH wet etching, LSCMO films show high chemical resistance with lower than 0.2 nm/min of etch rate. BHF wet etching shows high etching selectivity over photoresist mask and silicon substrates. The etch rates for LSCMO and BTO layers are 22 and 17 nm/min. For Ar IBE, LSCMO films and oxide buffer layers show similar etch rates, 16-17 nm/min that are lower compared to 24 nm/min for Si.

Free standing, self-supported heteroepitaxial LSCMO/BTO/ CeO_2 /YSZ membranes for bolometer pixels on Si was successfully fabricated by Ar IBE and ICP etching techniques using a preannealed photoresist. The structural investigation by TEM revealed the sharp interfaces between layers. The electrical property of the free standing membrane was slightly degraded due to strain release and multi-step etching effect. These results demonstrate feasibility to use heteroepitaxial oxide structures as a thermally isolated membrane with conventional photoresist patterning.

Key words: manganites, $\text{La}_{0.67}(\text{Sr},\text{Ca})_{0.33}\text{MnO}_3$ (LSCMO), $\text{La}_{0.67}\text{Sr}_{0.33}\text{MnO}_3$ (LSMO), $\text{La}_{0.67}\text{Ca}_{0.33}\text{MnO}_3$ (LCMO), Si, GaAs, SiGeC, colossal magnetoresistance (CMR), bolometer, infrared (IR), micromachining, fabrication, strain, etching.

Contents

<i>Abstract</i>	<i>v</i>
<i>Acknowledgment</i>	<i>ix</i>
<i>List of appended papers</i>	<i>xi</i>
<i>Used Abbreviations</i>	<i>xv</i>
1. Introduction	1
1.1 Infrared radiation	1
1.2 Infrared detector	2
1.3 Bolometer	4
1.3.1 General aspects of bolometer	4
1.3.2 Noise characteristics of bolometer	6
1.4 About this work	8
References	9
2. Colossal magnetoresistive manganites	11
2.1 Electrical behavior of manganites	11
2.2 Double exchange model and magnetic behavior	13
2.3 Structural tolerance factor	16
2.4 Strain effect on CMR manganites	17
2.5 Device applications of manganites	19
References	22
3. Epitaxial CMR film growth	23
3.1 CMR manganite film growth techniques	23
3.1.1 Pulsed laser deposition	23
3.1.2 Metal organic chemical vapor deposition	24
3.1.3 Magnetron sputtering	24
3.1.4 Molecular beam epitaxy	24
3.1.5 Sol-gel technique	25
3.2 Substrates and buffer layers	25
3.2.1 CMR manganites on silicon substrates	25
3.2.2 CMR manganites on GaAs	26
3.3 Strain effect on CMR manganites using $\text{Si}_{1-x}\text{Ge}_x$ and $\text{Si}_{1-y}\text{C}_y$ layers on Si	27
References	29

4. Characterization of CMR manganite films	31
4.1 X-ray diffraction	31
4.2 Reciprocal lattice mapping (RLM)	35
4.3 Rutherford backscattering spectroscopy (RBS)	38
4.4 Transmission electron microscopy (TEM)	39
4.5 Atomic force microscopy (AFM).....	41
4.6 Scanning spreading resistance microscopy (SSRM)	42
4.7 Magnetic force microscopy (MFM)	46
4.8 Noise measurement	48
4.9 Electrical/Magnetic transport measurements	51
References	55
5. Microfabrication of IR CMR bolometer	57
5.1 General aspects	57
5.2 Patterning for CMR manganites.....	57
5.3 Etching of CMR manganites.....	58
5.4 Fabrication of free standing manganite membrane	59
References	61
6. Free standing micromachined epitaxial CMR membrane for uncooled infrared bolometer	63
6.1 Wet and dry etching results.....	63
6.2 Microfabrication of free standing epitaxial manganite films for IR bolometer	68
References	72
7. Summary and conclusions	73
8. Future works	75
9. Summary of appended papers	77
Appended papers	79

Acknowledgements

At first, I would like to thank my academic supervisor, Professor Alexander M. Grishin in division of Condensed Matter Physics, Laboratory of Solid State Devices (SSD), Department of Microelectronics and Information Technology (IMIT), Royal Institute of Technology (KTH). Without his guidance and perceptive discussions, I have never finished my Ph. D study. Спасибо!

Special thanks go to Dr. S. Khartsev, who is a wonderful mentor and adviser in our group. I have learned many scientific things from him. He is both experimental physicist and electrical engineer! Always he shares his valuable time with me to discuss scientific issues and problems. Thanks a lot! Спасибо!

Many thanks go to the former and current members of our group, Dr. Peter Johnsson, Dr. Sören Karl, Dr. Vasyl Denysenkov, Dr. Mats Blomqvist, my old roommate-Dr. Jürgen Brünahl, Dr. Jhigang Jhang in China, Rickard Fors and Petra Johansson. It was very valuable time to share with all of you. Tack så mycket! Danke Schon!

I also appreciate the Korean colleague group *called KOSAS*, Dr. Sang-Ho Yoon, Dr. Hyun-Sun Park, Dr. Choon-Rae Cho who introduced me to our laboratory, Dr. Jung-Hyuk Koh, Dr. Moo-Young Kim, Dr. Ki-Bok Min, Dr. Chan-Bae Park, Dr. Sang-Mo Koo, Jang-Yong Kim and Hyung-Seok Lee for time sharing with valuable discussions, sport activities. I wish a good luck to Jang-Yong Kim and Hyung-Seok Lee for finalizing Ph. D study! The best wishes go also to new comer, Sung-Woo Cho and other Korean Ph. D students and researchers in Karolinska, Uppsala and other Swedish University (Högskolan) in KOSAS members.

I give my gratitude other groups and persons - Prof. Sebastian Lourdudoss, Thomas Aggerstam who is my best Swedish friend, nice helper during Ph. D period, Audrey Barrier, my SPM technique teacher Dr. Olivier Douheret in IMEC, Belgium, Dr. Krishnan Baskar in India, Julius Hållstedt, Maciej Wolborski, Dr. Erdal Suvar and Docent Henry H. Radamson who introduced me to SiGeC material and high resolution X-ray world and Dr. Birger Emmoth who taught and assisted me to get the license of Rutherford backscattering system in Uppsala University. Special thanks go to Zandra Lundberg who always helps me with very kind administrative works, and Dr. Y.-B. Wang, Timo Söderqvist, Cecilia Aronsson in Replisaurus, Susanne Almqvist in Acreo for nice information and discussions. Additional thanks go to Radamson and Aggerstam for helping me with improving my thesis.

Very special thanks go to members of Korean church named *Koreanska Församlingen i Stockholm*: Pastor Seong-Seob Lee called as Hope, Hee-Pal Song with his whole families (Kyu-Jin Song called as *Seon-Bae-Nim* and Kyu-Whan Song), Woo-Seok Park with his family, Dong-Kyu Shin with his family, Si-Chun Lee with his family, Myung-Sook Choi who serves my family a lot with nice cooking technology. Boo-Mi-Ja Lim with her sister, Mi-Young Cho with her family, Dr. Kyu-

Nam Choi with his family, Dr. Sook-Young Lee with her family, Moon-Song Jeon with his family in Korea, Dr. Park in Sungshin woman university and Dr. Koo in Ulsan university in Korea, Dong-Ho Jang with Seri Park in Germany, and all of new and former members. Also, let me give my thanks to former Pastor Seong-nam Park with his family in Masan city, Korea and Keun-Wan Kim with his family in Täby. Many thanks to Kyung-Joo Park with his husband in Gröndal, Jin-Ha Kim with his family in Russia, Mr. Kang in Oriental Sushi in Stockholm central and Chang-Hun's family in Korea. Without their helping, the life in Sweden should be much harder then I had expected.

Same thanks go to the Korean school in Sweden where I served as a teacher in advanced Korean class, my long-term students Edith Pelkonen Ahlberg, Sofia Petersen, Gillis Nygren, Marie Lousie Eriksson. Good luck to your learning of Korean language. I hope all of you will speak Korean fluently soon! In addition, I wish to give my thanks to other Korean teachers, Nan-Hee Lee and Hyun-Sook Litonen.

I would like to thank my whole family who support me in spirit and mind. Very special thanks to my mother Myung-Soon Jeon, mother's brother Ki-Sun Jeon, mother's sister Kyung-Ja Jeon with her family (Bae-Chun Lee and Jae Won) and my father and mother-in-law Jong-Hong Park and Sun-Shim Choi (including Se-Eun, Sun-Chul, Ji-Hyun, Sang-Hee with their families) for their never-forgettable endless supports and praying from very beginning of Ph. D study in Sweden.

Finally, I never forget the ultimate and endless supports from my wife, Jin-Young, during studying in KTH, Sweden. Without support and encourage from her, it would be too hard to finish my Ph. D. Seong-Won and Jun-Won my lovely sons! You are my great happiness during staying period in Sweden. 사랑한다~.

This work was financially supported by the Swedish Foundation for Strategic Research (SSF). Thank you.

Tack så mycket!
Thank you!
Danke schon!
Спасибо!
감사합니다.

Joo-Hyung Kim

Kista-Stockholm, Sweden
November 1, 2005

Appended Papers

1. **Epitaxial colossal magnetoresistive $\text{La}_{0.67}(\text{Sr,Ca})_{0.33}\text{MnO}_3$ films on Si**
J.-H. Kim, S. I. Kharsev, and A. M. Grishin, Appl. Phys. Lett. **82**(24), 4295 (2003).
2. **Epitaxial Colossal Magnetoresistive/Ferroelectric Heteostructures**
A. M. Grishin, S. I. Kharsev, J.-H. Kim and Jun Lu, Integrated Ferroelectrics **67**, 69 (2004).
3. **Microfabricated heteroepitaxial oxide structures on silicon for bolometric arrays**
J.-H. Kim, A. M. Grishin, NSTI Nanotech 2005 Proceeding, Vol. **3**, 521 (2005).
4. **Free standing epitaxial $\text{La}_{1-x}(\text{Sr,Ca})_x\text{MnO}_3$ membrane on Si for uncooled infrared microbolometer**
J.-H. Kim, A. M. Grishin, Appl. Phys. Lett. **87**, 033502 (2005).
5. **Integration of colossal magnetoresistors with GaAs**
S. I. Khartsev, J.-H. Kim and A. M. Grishin, J. Crystal Growth **284**, 1-5 (2005).
6. **The effect of strained $\text{Si}_{1-x}\text{Ge}_x$ and $\text{Si}_{1-y}\text{C}_y$ layers for $\text{La}_{0.75}\text{Sr}_{0.25}\text{MnO}_3$ films grown on oxide-buffered Si substrates**
J.-H. Kim, A. M. Grishin, H. H. Radamson, will be published in J. Appl. Phys. (2005).
7. **Mircofabrication of epitaxial $\text{La}_{1-x}(\text{Sr,Ca})_x\text{MnO}_3$ IR bolometer on Si**
Joo-Hyung Kim, Alexander M. Grishin, will be published in Integrated Ferroelectrics (2005).
8. **Wet etching study of $\text{La}_{0.67}(\text{Sr}_{0.5}\text{Ca}_{0.5})_{0.33}\text{MnO}_3$ films on silicon substrates**
Joo-Hyung Kim, Alexander M. Grishin, submitted to J. Microelectromech. Systems (2005).
9. **Wet and dry etching of $\text{La}_{0.67}(\text{Sr,Ca})_{0.33}\text{MnO}_3$ films on Si**
Joo-Hyung Kim, Alexander M. Grishin, submitted to Thin Solid Films (2005).

Related work not included in the thesis

1. **Epitaxial $\text{La}_{0.67}(\text{Sr,Ca})_{0.33}\text{MnO}_3$ Films on Si for IR Bolometer Applications**
A. M. Grishin, S. I. Khartsev, J.-H. Kim, Jun Lu, Mater. Res. Soc. (MRS) Proceedings Vol. **811**, E3.2 (2004).
2. **The structural/electrical properties of $\text{La}_{0.75}\text{Sr}_{0.25}\text{MnO}_3$ films with strain effects of $\text{Si}_{1-x}\text{Ge}_x$ and $\text{Si}_{1-y}\text{C}_y$ on Si substrates**
Joo-Hyung Kim, Alexander M. Grishin, Henry Radamson, submitted to Thin Solid Films (2005).

Presentations (Oral, Poster and Invited talks)

1. **Novel CMR material on Silicon for bolometric application (Invited Talk)**
Joo-Hyung Kim, presented at Perovskites for Chemistry and Physics, Angstrom Laboratory, Uppsala University, Uppsala, Sweden, February (2004).
2. **Epitaxial Colossal Magnetoresistive/Ferroelectric Heterostructures on Si (Invited Talk)**
A. M. Grishin, S. I. Khartsev, J.-H. Kim, Jun Lu, 16th International Symposium on Integrated Ferroelectrics (ISIF 2004), Gyeongju, Korea, April (2004).
3. **Epitaxial $\text{La}_{0.67}(\text{Sr,Ca})_{0.33}\text{MnO}_3$ Films on Si for IR Bolometer Applications (Oral Presentation)**
A. M. Grishin, S. I. Khartsev, J.-H. Kim, Jun Lu, Mater. Res. Soc. (MRS) Spring Meeting, San Francisco, USA, April (2004).
4. **Etching of Heteroepitaxial $\text{La}_{0.67}(\text{Sr,Ca})_{0.33}\text{MnO}_3/\text{Bi}_4\text{Ti}_3\text{O}_{12}/\text{CeO}_2/\text{YSZ}/\text{Si}$ Film Structures for IR Bolometer Applications (Poster Presentation)**
Joo-Hyung Kim, Sergey I. Khartsev, Alexander M. Grishin, Mater. Res. Soc. (MRS) Fall Meeting H8.6, Boston, USA, December (2004).
5. **Epitaxial $\text{La}_{0.67}\text{Ca}_{0.33}\text{MnO}_3$ and $\text{La}_{0.67}\text{Sr}_{0.33}\text{MnO}_3$ Films on GaAs (Oral Presentation)**
Sergey I. Khartsev, Joo-Hyung Kim and Alexander M. Grishin, Mater. Res. Soc. (MRS) Fall Meeting H7.11, Boston, USA, December (2004).
6. **Microfabrication of epitaxial $\text{La}_{0.67}(\text{Sr,Ca})_{0.33}\text{MnO}_3$ IR Bolometer On Silicon (Oral Presentation)**
Joo-Hyung Kim, Alexander M. Grishin, 17th International Symposium on Integrated Ferroelectrics (ISIF 2005), Shanghai, China, April 22-24. (2005).
7. **Microfabricated heteroepitaxial oxide structures on silicon for bolometric arrays (Poster Presentation)**
J.-H. Kim, A. M. Grishin, The Nanotechnology Conference and Trade Show (NSTI Nanotech 2005), Anaheim, CA., USA, May 8-12 (2005).
8. **The wet and dry etching study of thin $\text{La}_{0.67}(\text{Sr,Ca})_{0.33}\text{MnO}_3$ films on silicon substrates (Poster Presentation)**
Joo-Hyung Kim, Alexander Grishin, 13th International Congress on Thin Films/ 8th International Conference on Atomically Controlled Surfaces, Interfaces and Nanostructures (ICTF 13/ACSIN 8)-P36, Stockholm, Sweden, June 20-23 (2005).
9. **The Structural/electrical properties of $\text{La}_{0.75}\text{Sr}_{0.25}\text{MnO}_3$ films with strain effects of $\text{Si}_{1-x}\text{Ge}_x$ and $\text{Si}_{1-y}\text{C}_y$ on Si substrates (Oral Presentation)**
Joo-Hyung Kim, Alexander Grishin, Henry Radamson, 13th International Congress on Thin Films/ 8th International Conference on Atomically Controlled

Surfaces, Interfaces and Nanostructures (ICTF 13/ACSIN 8)-O10, Stockholm, Sweden, June 20-23 (2005).

10. Exploiting the properties of Silicon nanocrystals in silica-based intergrated optics (Poster Presentation)

Dainese Matteo, Sychugov Ilya, Joo-Hyung Kim, Swillo Marcin, 13th International Congress on Thin Films/ 8th International Conference on Atomically Controlled Surfaces, Interfaces and Nanostructures (ICTF 13/ACSIN 8)-P394, Stockholm, Sweden, June 20-23 (2005).

Used Abbreviations

AF	: Anti-ferromagnetic
AFI	: Anti-ferromagnetic insulating
AFM	: Atomic force microscopy
BHF	: Buffered hydrofluoric acid, 87.5% NH_4OH +12.5% HF
BTO	: Bismuth titanite, $\text{Bi}_4\text{Ti}_3\text{O}_{12}$
CMR	: Colossal magnetoresistance
EBL	: Electron beam lithography
F	: Ferromagnetic
FeFET	: Ferroelectric field effect transistor
FIB	: Focused ion beam
FWHM	: Full width at half maximum
GaAs	: Gallium arsenide
HRXRD	: High-resolution X-ray diffraction
IBE	: Ion beam etching
ICP	: Inductively coupled plasma
IR	: Infrared
KOH	: Potassium hydroxide
LBMO	: $\text{La}_{0.67}\text{Ba}_{0.33}\text{MnO}_3$
LCMO	: $\text{La}_{0.67}\text{Ca}_{0.33}\text{MnO}_3$
LSCMO	: $\text{La}_{1-x}(\text{Sr},\text{Ca})_x\text{MnO}_3$, $\text{La}_{0.67}(\text{Sr},\text{Ca})_{0.33}\text{MnO}_3$
LSMO	: $\text{La}_{1-x}\text{Sr}_x\text{MnO}_3$, $\text{La}_{0.67}\text{Sr}_{0.33}\text{MnO}_3$, $\text{La}_{0.75}\text{Sr}_{0.25}\text{MnO}_3$
LWIR	: Long wavelength infrared
MEMS	: Micro-electro-mechanical systems
MFM	: Magnetic force microscopy
MR	: Magnetoresistance
MRAM	: Magnetic random access memory
MWIR	: Middle wavelength infrared
MOCVD	: Metal organic chemical vapor deposition
NGO	: Neodymium gallate, NdGaO_3
NEP	: Noise equivalent power
NEMFD	: Noise equivalent magnetic field difference
NETD	: Noise equivalent temperature difference
NIL	: Nano imprint lithography
PLD	: Pulsed laser deposition
P	: Paramagnetic
PR	: Photoresist
RLM	: Reciprocal lattice mapping
RPCVD	: Reduced pressure chemical vapor deposition
RIE	: Reactive ion etching
RTA	: Rapid thermal annealing
RBS	: Rutherford backscattering microscopy
RMS	: Root mean square
SEM	: Scanning electron microscopy
Si	: Silicon
$\text{Si}_{1-x}\text{Ge}_x$: Silicon germanium layer

$\text{Si}_{1-y}\text{C}_y$: Silicon carbon alloy layer
SSRM	: Scanning spreading resistance microscopy
SNR	: Signal to noise ratio
STO	: Strontium titanate, SrTiO_3
TEM	: Transmission electron microscopy
TCR	: Temperature coefficient of resistance
TF	: Tolerance factor
YSZ	: Yttrium stabilized zirconia
XRD	: X-ray diffraction
XRL	: X-ray lithography

1. Introduction

1.1 Infrared radiation

The infrared (IR) is a certain range of wavelength longer than visible light. This IR radiation was discovered only 200 years ago by William Herschel's prism splitting of sunlight. Using his own invented monochromator, he measured the radiation energy and classified it according to the color range. However, the radiation energy was still detectable within invisible range over red color area called *infrared*.

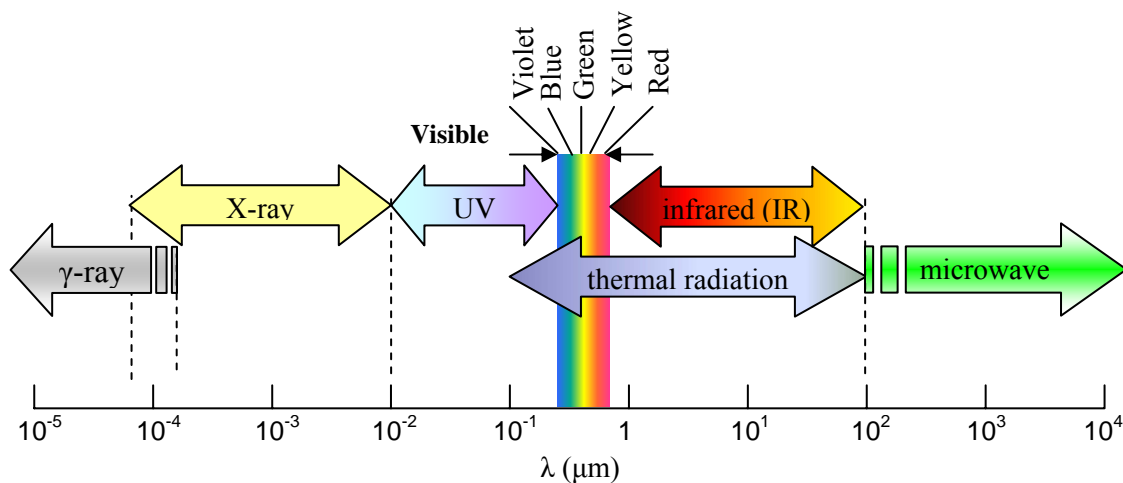


Figure 1-1. Spectra of electromagnetic radiation.

After this experiment, many experiments had been attempted to detect the IR radiation energy. *Seebeck*, in 1921, discovered the thermoelectric effect (*Seebeck effect*) from the ends of connection of two different wires, later called thermocouple. After that, using this thermoelectric effect, first thermopile was demonstrated in 1929.

Therefore, the IR detector is a transducer to convert energy from radiation to measurable signal. Using the detective ability of un-visible wavelength generated from radiation energy, there are many different applications: explorer of space objects military, security guard, medical investigation, night-vision system for automobile, fire detecting, industrial and constructional areas in any kinds of weather condition. Nowadays, the range of IR can be classified into middle wavelength IR (MWIR, 3-5 μm), long wavelength IR (LWIR, 8-14 μm) and far IR (FIR, 30-1000 μm).

To understand radiation characteristics, a *blackbody* concept is very useful. A blackbody, which is an ideal surface, has three important properties [1]:

- (i) All incident radiation is absorbed by a blackbody, regardless of wavelength and direction.
- (ii) Any kind of surfaces cannot emit more energy than a blackbody for a defined temperature and wavelength.

(iii) A blackbody emits radiation as a function of wavelength and temperature, but this radiation is independent of direction. Therefore, blackbody is a dispersed emitter.

This radiation energy of a blackbody can be expressed by Stefan-Boltzmann law:

$$E_b = \int_0^\infty \pi \frac{2hc_o^2}{\lambda^5 (e^{\frac{hc_o}{\lambda kT}} - 1)} d\lambda = \int_0^\infty \frac{C_1}{\lambda^5 (e^{\frac{C_2}{\lambda T}} - 1)} d\lambda = \sigma \cdot T^4 \quad (1-1)$$

where h , k , c_o , and σ are the Planck constant (6.6256×10^{-34} J·s), the Boltzmann constant (1.38×10^{-23} J/K), the speed of light in vacuum (2.998×10^8 m/s) and the Stefan-Boltzmann constant (5.67×10^{-8} W/m²·K⁴). From Eq. 1-1, total radiation energy can be calculated given the absolute temperature, T . From the maximum point of blackbody spectral distribution, Wien's displacement law can provide the corresponding wavelength, given by

$$\lambda_{\max} T = 2897.8 \mu\text{m} \cdot \text{K} \quad (1-2)$$

For example, solar radiation has a wavelength of 0.5 μm positioned in the middle of the visible spectrum. Therefore, the approximated surface temperature of the sun is 5800K. Because most viewed images in our surroundings are near 300 K, the corresponding wavelength distribution is around 10 μm with approximation of black or gray body. Therefore, most of thermal imaging systems operate in MWIR or LWIR ranges. Figure 1-1 shows the spectra of electromagnetic radiation.

1.2 Infrared detector

To detect infrared wavelength, there are many attempt to investigate different sensing materials and detecting technologies. In generally, there are two different infrared detecting categories: **photon detector** and **thermal detector** [2-5].

Photon detector: The principle of the photon detector, shown in Fig. 1-2, is that the absorbed radiation affects electronic energy distribution in the sensing material by electron interaction to produce the output signal. Therefore, it has a fast responsivity and low signal to noise level. However, disadvantage of these type detectors is cooling. To get the high performance photon detecting, cryogenic cooling system is required.

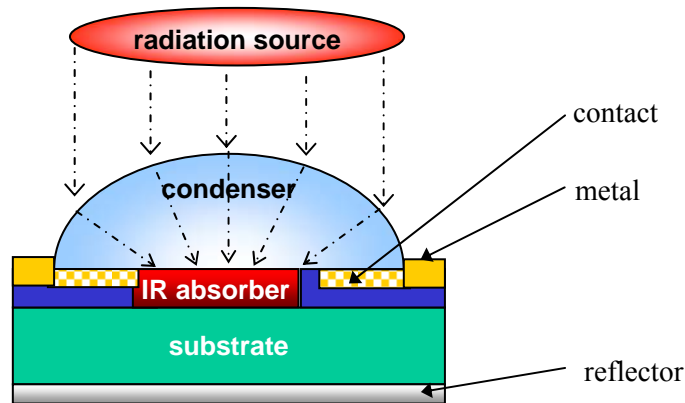


Figure 1-2. Concept of photon detector (after [2]).

Thermal detector: The thermal detector absorbs photon in the sensing material and the absorbed photon is thermalized. Therefore incoming radiation energy changes the electrical properties of the detecting material resulting in a modulation of electrical current passing through it. This modulation can be measured by temperature dependant resistivity so called *bolometer*, thermoelectric-induced voltage (*thermopile*), and pyroelectric effect. However, these thermal detectors must be constructed on the thermally isolated structure from the thermal surrounding. The drawback of thermal detector is vacuum packaging to minimize thermal effect from the surrounding.

The representative IR sensing materials for thermal and photon detectors are summarized in Table I [2].

Table I. Summary of thermal and photon IR detectors [2].

Type		Principles	Materials	Advantages	Disadvantages
T H E R M A L	thermopile	induced thermoelectric voltage	BiTe-TiSbTe <i>poly</i> -Si	- low cost - operated in room temperature - rugged system	- slow response time - low detectivity at high frequency
	pyro-electric	change of polarization or charge	(Ba,Sr)TiO ₃ Pb(Sc _{0.5} Ta _{0.5})O ₃ , LiTaO ₃		
	bolometer	resistance change	VO _x <i>a</i> -Si SiGe manganite oxide		
P H O T O N	intrinsic	optical excitation of free carriers (electron or hole) ➔ photoconductive or photovoltaic effect	IV-VI (➔ PbS, PbSe) II-VI (➔ HgCdTe) III-V (➔ InGaAs)	- stable material	- high thermal expansion coefficient - large permittivity
	extrinsic		Si:Ga Si:As Ge:Cu	- detect long wave-length - simple technique	- high thermal generation -operated at very low temperature
	free carrier		PtSi Pt ₂ Si IrSi	- low cost - high yield	- low efficiency - low temperature operation
	quantum wells		III-V (GaAs/AlGaAs , InGaAs/AlGaAs)	- matured material - multi color	- high thermal generation
			III-V (InAs/InGaSb, InAs/InAsSb)	- low Auger recom-bination rate - easy wavelength control	- complicated design - films growth difficulty
	quantum dots		InAs/GaAs InGaAs/InGaP Ge/Si	- low thermal generation	- complicated design - films growth difficulty

1.3 Bolometer

1.3.1 General aspects of bolometer

Fig. 1-3 illustrates a concept of bolometer. The detecting area of the thermal detector can be expressed by a **thermal capacitance** [J/K] C_{th} , called **thermal mass**, the absorbing volume to store heat energy. Since this sensing area is thermoelectrically coupled (= linked) to the supporting structure, **thermal conductance** [W/K] G_{th} , thermal insulating materials as a supporting membrane are required to minimize the heat flow.

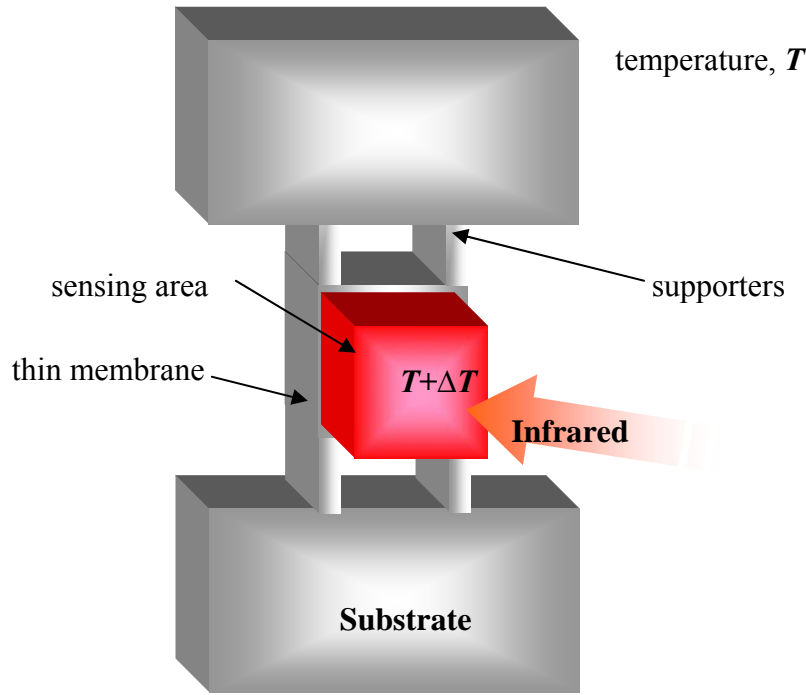


Figure 1-3. Schematic of infrared bolometer

To develop highly sensitive thermal detector, the corresponding temperature change must be as large as possible [2, 3].

$$\Delta T = \frac{\alpha \cdot \Psi}{(G_{th}^2 + \omega^2 C_{th}^2)^{1/2}} \quad (1-3)$$

where α , Ψ , ω are the radiation absorption coefficient, the incident radiation energy flux, and the angular frequency, respectively. To maximize the temperature sensitivity in Eq. 1-3, thermal mass of detecting area (C_{th}) and the structurally coupled thermal conductance (G_{th}) should be minimized. Therefore small size pixel design and thermally isolation by microfabrication are necessary to achieve the higher temperature changes.

In general, thermal time constant of thermal detectors is longer than for photon detectors. Due to tradeoff relation between ΔT and ω from Eq. 1-3, high sensitivity of thermal detectors can be obtained in the low frequency range.

To define the performance of the thermal detector, there are several important parameters figure of merits [3-5, 13]. Here, another figure of merits related to noise are explained in Chap 1.3.2.

- TCR ($= 1/R \cdot dR/dT$) is the relative rapid resistance change with temperature. This is dependant to the electrical transport property of sensing material.
- Thermal time constant, τ_{th} can be defined by the ratio of thermal mass over thermal conductance.

$$\tau_{th} = \frac{C_{th}}{G_{th}} \quad (1-4)$$

where C_{th} and G_{th} are strongly related to the sensing material properties and geometries of the bolometer.

- Responsivity (\mathfrak{R}_V , V/W) is the ratio of output signal to input radiation power, given by [11-13]

$$\mathfrak{R}_V = \frac{\Delta voltage}{\Delta power} = \frac{I_{bias} \cdot R \cdot TCR \cdot \alpha}{G_{th} (1 + \omega^2 \tau_{th}^2)^{1/2}} \quad (1-5)$$

where I_{bias} and R are the applied bias current and the resistance of detecting material, respectively.

To achieve high sensitive bolometer by minimization of G_{th} , Wood *et al* employed thermal isolated silicon nitride supporting structure in uncooled VO_x bolometer on Si wafer [6]. The isolated structure, $50 \mu m \times 50 \mu m$ with $0.5 \mu m$ thick Si_3N_4 membrane, was supported by two legs and had small thermal mass ($C_{th} \sim 10^{-9}$ J/K) and thermal conductance ($G_{th} \sim 10^{-7}$ W/K). The isolated membrane structure and corresponding image of microbolometer are shown in Fig. 1-4.

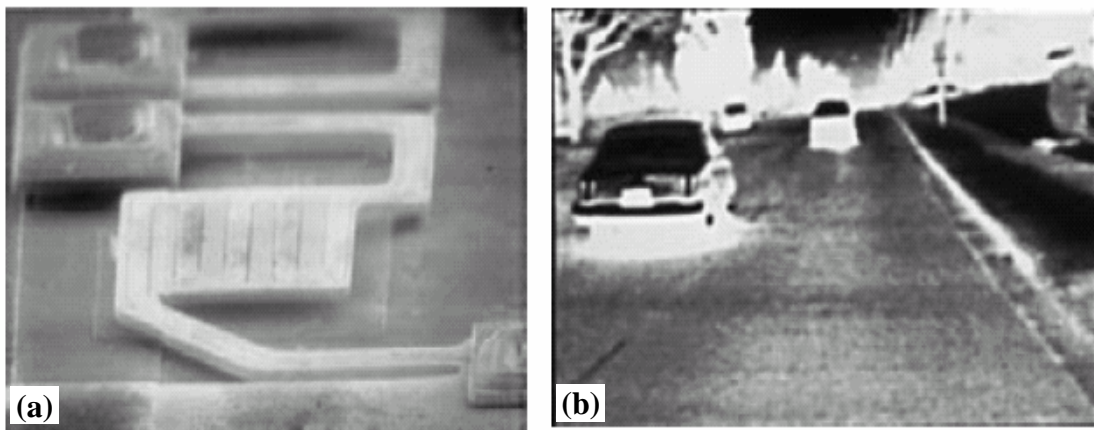


Figure 1-4. IR microbolometer with isolated supporting membrane (a) pixel structure (b) captured image of 240×336 pixels arrays bolometer (after [6]).

Another attempt to minimize thermal mass, Almasri *et al* demonstrated a self-supporting thin Y-Ba-Cu-O (YBCO) microbolometer without any supporting structure on $LaAlO_3$ substrates [7]. They utilized polyimide sacrificial layer, which was easily

removed by a chemical solution after device fabrication. Only two metal electrodes were used for supporting the thin Y-Ba-Cu-O microbolometer with 3.52×10^{-10} J/K of thermal mass. Recently, bendable YBCO microbolometer on polyimide substrate named Kepton was presented for flexible device application by Yaradanakul *et al* from the same group [8].

From another fabrication approach, Niklaus *et al* investigated the wafer-level membrane transfer bonding technique to minimize damages to bolometer arrays during the microfabrication process. This transfer bonding technique allows for low temperature process for integrated circuits. Bonding technique also can be useful for unstressed and very thin membrane for bolometric supporting structure [9].

1.3.2 Noise characteristics of bolometer

The sensitivity of a thermal detector is strongly affected by various noise sources. Noise can be defined as *unwanted disturbance*. The main noise sources in bolometer and its readout circuits are Johnson noise, low frequency noise called $1/f$ noise and thermal noise. Three main types of noise mechanism are briefly explained [10, 13].

1) **Johnson noise**, first observed by Johnson in 1927 and theoretically analyzed by Nyquist in 1928, stems from random thermally excited vibration of charge carriers in a conductor. Since electrons move randomly above 0 K, where the movement is temperature dependent, the motion of these carriers is similar to Brownian motion. This Johnson noise is present in all kinds of system related to resistance. Therefore, it can be assumed as a noiseless resistor. By assumption of the non-steady state, the voltage by the noise variation is given by

$$V_J = \sqrt{4kT \frac{R_{Load} \cdot R_{Bolo}}{R_{Load} + R_{Bolo}} \Delta f} \quad (1-6)$$

where R_{Load} , R_{Bolo} and Δf are the load resistance, the resistance of bolometer pixel and the noise bandwidth, respectively.

2) **Shot noise** is composed of random fluctuations, known as a thermal noise, of the electron current flowing in an electrical conductor. Therefore, the strength of shot noise has an increasing tendency by growing magnitude of the average current passing through the conductor. However, this noise must be distinguished from an equilibrium current fluctuation.

The voltage variance of random fluctuations (= thermal noise) by a biased voltage applied to a microbolometer is express by,

$$V_{th} = \sqrt{\frac{k \cdot V_{bias}^2 \cdot R_{Load} \cdot R_{Bolo} \cdot TCR \cdot T^2}{(R_{Load} + R_{Bolo})^2 \cdot C_{th} \cdot [1 + TCR \cdot \Delta T \frac{R_{Bolo} - R_{Load}}{R_{Bolo} + R_{Load}}]^2}} \quad (1-7)$$

where T and ΔT are the bolometer temperature and the temperature elevation of bolometer.

3) **Low frequency noise ($1/f$)** exhibits several unique properties. As frequency increases, spectral density of $1/f$ increases infinitely. Noise power follows $1/f^\alpha$ characteristics, where α is from 0.8 to 1.3. The importance of $1/f$ in semiconductor

devices is the traceable property that is depends on the material surface. To decrease $1/f$, surface treatment is important in semiconductor processing. The $1/f$ noise voltage in the biased bolometer can be expressed as

$$V_{1/f} = \sqrt{\log\left(\frac{f_2}{f_1}\right) \cdot C_f \cdot V_{bias}^2 \left[\frac{R_{Load} \cdot R_{Bolo}}{(R_{Load} + R_{Bolo})^2} \right]^2} \quad (1-8)$$

where f_1 , f_2 , C_f , V_{bias} are the lower frequency limit, the cutoff frequency of the readout circuit, $1/f$ noise constant and the biased voltage, respectively.

Because temperature changes in the sensing materials give the output signal which are equal to the RMS noise, the performance of bolometer can be evaluated by equivalent noise characterization.

- Noise equivalent power (NEP, W/ $\sqrt{\text{Hz}}$) is sensitivity of bolometer to fluctuation in incident energy [11-13]. The overall noise variation voltage can given by

$$V_{noise} = \sqrt{V_J^2 + V_{th}^2 + V_{1/f}^2} \quad (1-9)$$

With assumption of negligible photon noise from the incident radiation and readout circuit noise, NEP can be given by [11, 12]

$$NEP = \sqrt{\frac{4kT^2 G_{th}}{\alpha^2} + \frac{4kTR}{\Re_v^2} + \frac{S_v(f)}{\Re_v^2}} \quad (1-10)$$

where R , S_v are absorption coefficient, resistance of material and spectral noise fluctuation. First term in Eq. 1-10 stems from phonon noise by thermal fluctuation that is from random exchange of energy between the bolometer and heat sink via thermal conductance. Second and third terms are caused by Johnson noise and background (= excess) noise from surrounding.

- The output signal must be compared to the background noise [12]. The signal to noise ratio (SNR) is given by

$$SNR = \sqrt{\frac{P}{R}} \cdot \frac{\frac{dR}{dT} \Delta T}{\sqrt{4kTR\Delta f}} = I_{bias} \frac{\frac{dR}{dT} \Delta T}{\sqrt{4kTR\Delta f}} \quad (1-11)$$

where P is the constant power supplied from power supply.

- Noise equivalent temperature difference (NETD, K/ $\sqrt{\text{Hz}}$) with an optical system can be expressed as [13]

$$NETD = 1.57 \times 10^4 \frac{F^2 \cdot V_{noise}}{\Re_v \cdot A} \quad (1-12)$$

where $F (= f/\#)$, V_{noise} , A and 1.57 are the optical system performance, the total noise voltage from both readout circuit and bolometer, the detecting area, and the dimensional conversion for $m^2 \cdot K/W$, respectively.

■ Detectivity (D^* , $cm \cdot \sqrt{Hz}/W$), sensitivity of bolometer, is defined as [13]

$$D^* = \frac{\sqrt{A \cdot B}}{NEP} \quad (1-13)$$

where B is the electrical bandwidth.

1.4 About this work

Nowadays, the uncooled IR bolometer is very attractive devices both for space and terrestrial applications. For highly sensitive bolometric applications, the new temperature dependant materials with large resistance change have caught much attention. The temperature coefficient of resistance of VO_x ($TCR \sim 2-2.5 \% K^{-1}$), polycrystalline $SiGe$ ($3 \% K^{-1}$), $YBa_2Cu_3O_{7-\delta}$ ($3.5 \% K^{-1}$) are suggested as the IR sensing materials on Si_3N_4 , SiO_2 and N_xO_ySi membranes. [6, 14-16]

Perovskite metal-oxide manganites $La^{+3}_{1-x}A^{+2}_xMnO_3$ ($A^{+2} = Ca, Sr, Ba, Pb$) with colossal magnetoresistance effect (CMR) have also been suggested for uncooled IR bolometer [17]. In these materials, the maximum of the TCR occurs in close vicinity of semiconductor-to-metal phase transition temperature T_c . They can be tailored by alloying at room temperature and reaches magnitudes as high as $35 \% K^{-1}$ at 266 K [18]. In spite of the potential for those devices, there is no report for CMR manganite bolometer. Moreover, just few reports for CMR films on semiconductor substrates have been reported because of the difficulties in growing these films. By developing CMR manganites on Si substrates, new applications for these materials such as bolometric and spintronics devices can be realized.

Therefore, the main objectives of this thesis are

- (1) To grow high quality CMR manganite films on semiconductor substrates (Si and GaAs) for bolometric application including structural, electrical, magnetic and noise characterizations.
- (2) Systematic studies of strain effects on structural and electrical properties of CMR manganite films by applying $Si_{1-x}Ge_x$ and $Si_{1-y}C_y$ layers on Si substrates.
- (3) Wet and dry etching of CMR films/buffer oxide layers grown on Si substrates.
- (4) Microfabrication of $20 \mu m \times 30 \mu m$ size, self-supported free standing CMR manganite membranes on silicon substrates for a bolometric application. Here the feasibility of microfabrication for bolometric array of manganite films is the main issue. Note that the bolometric performances were evaluated without a readout circuit and an optical system.

References

- [1] Frank P. Incropera and David P. De Witt, *Fundamentals of Heat and Mass Transfer*, 3rd ed., John Wiley & Son, Singapore, (1990).
- [2] A. Rogalski, *Progress in Quantum Electronics* **27**, 59 (2003); J. Piotrowski, A. Rogalski, *Infrared Phys. Technol.* **46**, 115 (2004).
- [3] L. Méchin, J.-C. Vilégier, D. Bloyet, *IEEE Tran. Appl. Supercond.* **7**(2), 2382 (1997).
- [4] P. W. Kruse, 9th IEEE International Symposium on Application of Ferroelectrics. 643 (1995).
- [5] G. H. Rieke, *Detection of Light from the Ultraviolet to the Submillimeter*, Cambridge University Press, New York (1994).
- [6] B. E. Cole, R. E. Higashi, R. A. Wood, *Proc. IEEE* **86**, 1679 (1998); B. E. Cole, R. E. Higashi, J. A. Ridley, patent US 6287940 B1, Sep. 11, (2001).
- [7] M. Almasri, D. P. Butler, Z. Çelik-Butler, *J. Microelectromech. Sys.* **10**(3), 469 (2001).
- [8] A. Yaradanakul, D. P. Butler, Z. Ç. Bulter, *IEEE Trans. Electron Devices* **49**(5), 930 (2002).
- [9] F. Niklaus, E. Kälvesten, G. Stemme, *J. Micromech. Microeng.* **11**, 509 (2001).
- [10] C. D. Motchenbacher, J. A. Connelly, *Low-Noise Electronic System Design*, John Wiley & Son, New York (1993).
- [11] B. Lakew, J. C. Brasunas, S. Aslam, D. E. Pugel, *Sensors and Actuators, A* **114** 36 (2004).
- [12] A. Lisauskas, S. I. Khartsev, A. Grishin, *J. Appl. Phys.* **89**(5), 6961 (2001); Alvydas Lisauskas, *Electrical Noise in Colossal Magnetoresistors and Ferroelectrics*, Doctoral Thesis, Royal Institute of Technology, Sweden (2001).
- [13] B. Li, S. Huang, X. Zhang, *Proc. of SPIE* **5564**, 123 (2004).
- [14] N. Oda, Y. Tanaka, T. Sasaki, A. Ajisawa, A. Kawahara, S. Kurashina, *NEC Res. & Develop.* **44**, 171 (2003).
- [15] S. Sedky, P. Fiorini, M. Caymax, C. Baert, L. Hermans, R. Mertens, *IEEE Electron Device Lett.* **19**, 376 (1998).
- [16] R. Haakenaasen, D. K. Fork, J. A. Golovchenko. *Appl. Phys. Lett.* **64**, 1573 (1994); C. M. Travers, A. Jahanzeb, D. P. Butler, Z. Ç-Bulter, *J. Micoelectromech. Sys.* **6**, 271 (1997).
- [17] A-M Haghiri-Gosnet, J-P Renard, *J. Phys. D:* **36** R127 (2003).
- [18] S. I. Khartsev, A. M. Grishin, *Mat. Res. Soc. Symp. Proc.* **666**, F7.12 (2001); Alvydas Lisauskas, S. I. Khartsev, A. M. Grishin, *Appl. Phys. Lett.* **77**, 756 (2000).

2. Colossal magnetoresistive manganites

Mixed-valence perovskite manganites, formulated by $\text{La}_{1-x}\text{A}_x\text{MnO}_3$ (where $\text{A}^{+2} = \text{Ca, Sr, Ba, Pb}$), are very interesting materials due to their great potential for devices. They exhibit colossal magnetoresistance (CMR) effect in close vicinity of the metal-semiconductor (ferro- to para-magnetic) phase transition temperature (Curie temperature) T_c . erromagnetic (F) metallic behavior with spin-dependent transport properties occurs around $x \approx 0.3$, whereas anti-ferromagnetic insulating behaviors were found at low or high values of x [1, 2].

This metal-semiconductor phenomenon was early explained by double exchange model theory [3]. In case of $\text{Mn}^{+3}\text{-O-Mn}^{+4}$, Mn ions can exchange their valence between Mn^{+3} and Mn^{+4} with simultaneous jumping of e_g electrons in the 3d shell from Mn^{+3} to Mn^{+4} ions. However, anti-ferromagnetic behavior occurs for $\text{Mn}^{+3}\text{-O-Mn}^{+3}$ whereas antiferro/ferromagnetic interaction is observed for $\text{Mn}^{+4}\text{-O-Mn}^{+4}$.

Fig. 2-1 illustrates the structure of a $\text{La}_{1-x}\text{A}_x\text{MnO}_3$ CMR film. The *tri*-valence La_{1-x}^{+3} and A_x^{+2} are located at all-corners of the unit perovskite cell. Oxygen ions occupy the center of the faces in the unit cell. The smallest Mn ions exist in the center of the octahedral oxygen ions.

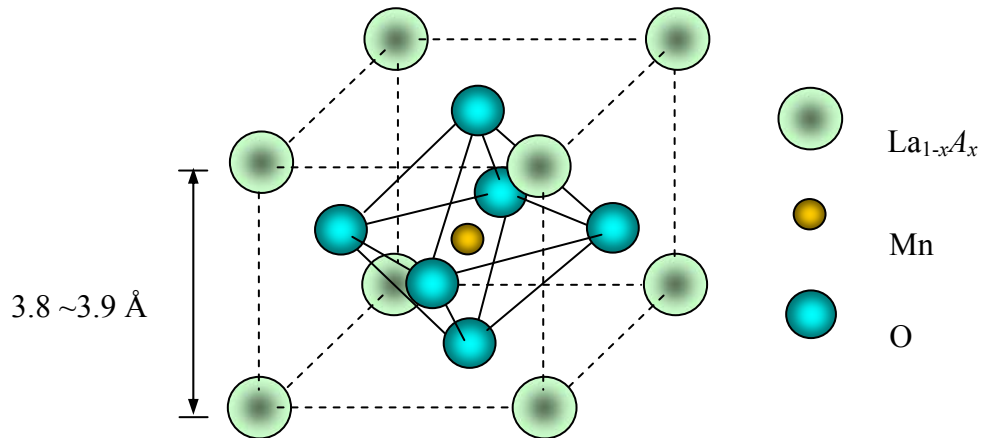


Figure 2-1. Schematic of perovskite manganites $\text{La}_{1-x}\text{A}_x\text{MnO}_3$.

2.1 Electrical behavior of manganites

The representative temperature dependent resistivity of CMR manganite $\text{La}_{0.67}\text{Sr}_{0.33}\text{MnO}_3$ and $\text{La}_{0.67}\text{Ca}_{0.33}\text{MnO}_3$ films on oxide buffered silicon substrates are presented in Fig. 2-2. The resistivity curves can be divided into three different electrical regions:

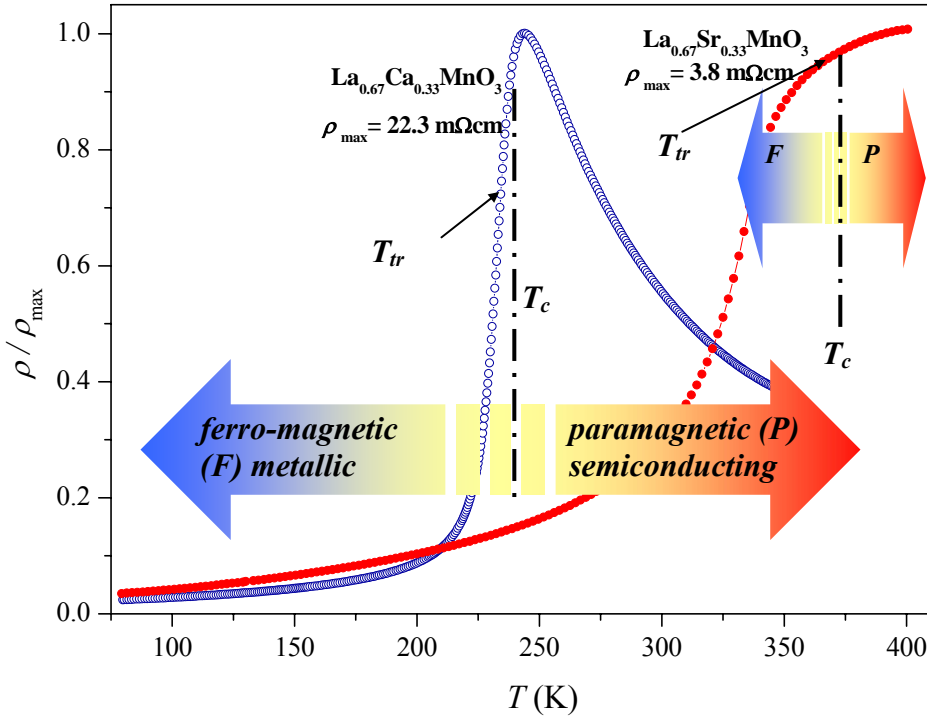


Figure 2-2. Normalized temperature dependent resistivity of $\text{La}_{0.67}\text{Sr}_{0.33}\text{MnO}_3$ and $\text{La}_{0.67}\text{Ca}_{0.33}\text{MnO}_3$ films on oxide buffered Si (T_c and T_{tr} represent Curie temperature and transition temperature).

■ **Low temperature range:** Electrical resistivity tends to increase with increasing temperature, Mn spins alignment allow delocalization of e_g electrons, therefore low resistivity ferro-magnetic (F) phase occurs with

$$\rho = \rho_0 + a_1 T^2 + a_2 T^4 \quad (2-1)$$

where, a_1 and a_2 are field dependent. By external magnetic field, this alignment of Mn ions can be controlled in the range of $T \leq T_c$ [4].

■ **Near metal-to-semiconductor transition:** The most prominent behavior, called CMR effect, occurs in temperature range near T_c due to metal to semiconductor transition as early mentioned. Moreover, the manganite films show pressure dependent and external magnetic field dependent resistance [5, 6].

■ **Paramagnetic area:** The electrical behavior in the paramagnetic region, shown in Fig. 2-2 following three main laws:

First, Mott variable-range-hopping (VRH), expressed by

$$\rho = \rho_\infty e^{(T_0/T)^{1/4}} \quad (2-2)$$

was suggested by localization of e_g electrons [7, 8].

Second is adiabatic polaron hopping by local lattice distortion given by

$$\rho \sim T \cdot e^{(E_0/k_B T)} \quad (2-3)$$

This lattice distortion, *John-Teller distortion*, due to lattice mismatch could induce the movement of charge carrier [9, 10].

Third is related to thermal activation law by existence of pseudo gap at the Fermi level in the paramagnetic phase [11].

$$\rho = \rho_\infty e^{(E_0/k_B T)} \quad (2-4)$$

2.2 Double exchange model and magnetic behavior

If the electron is on the Mn^{4+} , it will have two energy states: line up parallel or anti-parallel to spin S_1 . The transfer of e_g electron, S_2 , between Mn^{3+} and Mn^{4+} can be written by $t = t_0 \cos(\theta/2)$ where θ is the angle between S_1 and S_2 [12]. The two energy levels of $E_0 \pm t$, where E_0 is the energy level at $t = 0$, can be produced by the electron transfer process in Fig. 2-3 [13]. Therefore, the F metallic behavior can be revealed by parallel spin configuration with maximized t at $\theta = 0$ and anti-parallel at $\theta = \pi$.

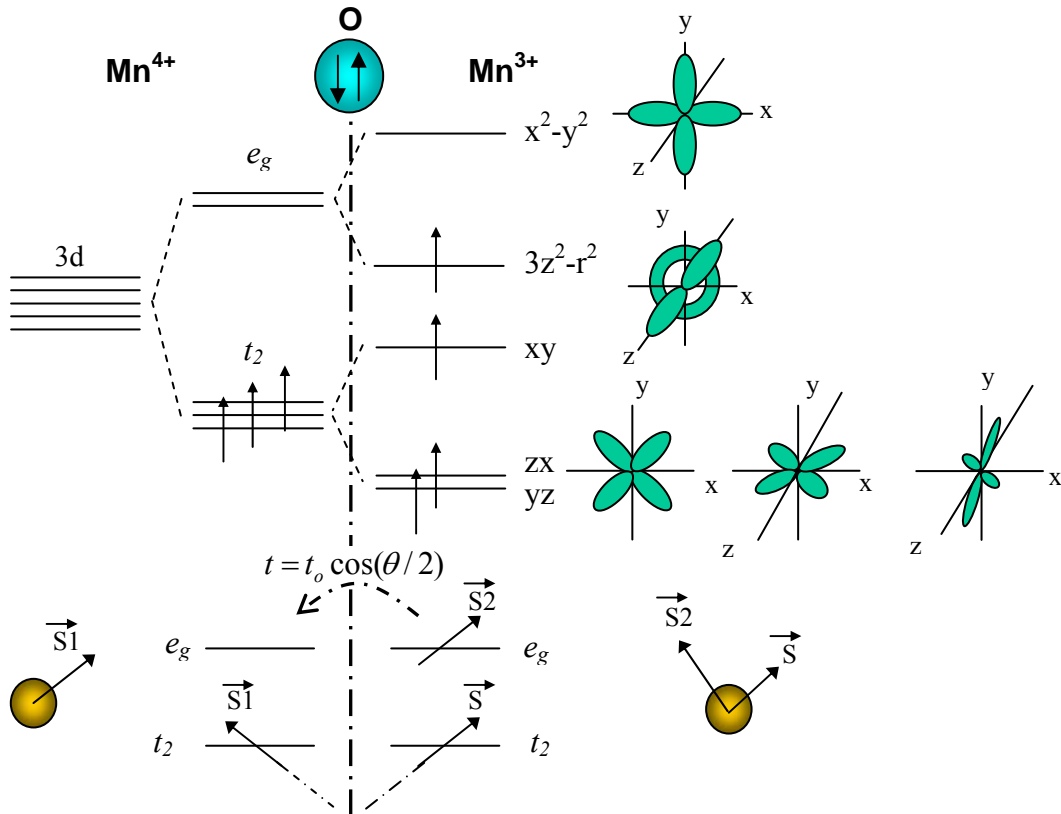


Figure 2-3. Schematic of energy level and double exchange mechanism of Mn^{4+} -O- Mn^{3+} ions (after [13]). Here S are spins of 3d shells.

Using *semicovalent-covalent* exchange theory with double exchange model, Goodenough *et al* described the qualitative of perovskite-type manganites [14]. The structural, electrical and magnetic properties depend on x value (= fraction of Mn^{4+}) can be divided into nine regions: α , $\alpha+\beta$, β , $\beta+\gamma$, γ , $\gamma+\delta$, δ , $\delta+\epsilon$ and ϵ . Predicted intensity of magnetization of manganites and the corresponding qualitative qualities are presented in Fig. 2-4 and Table II.

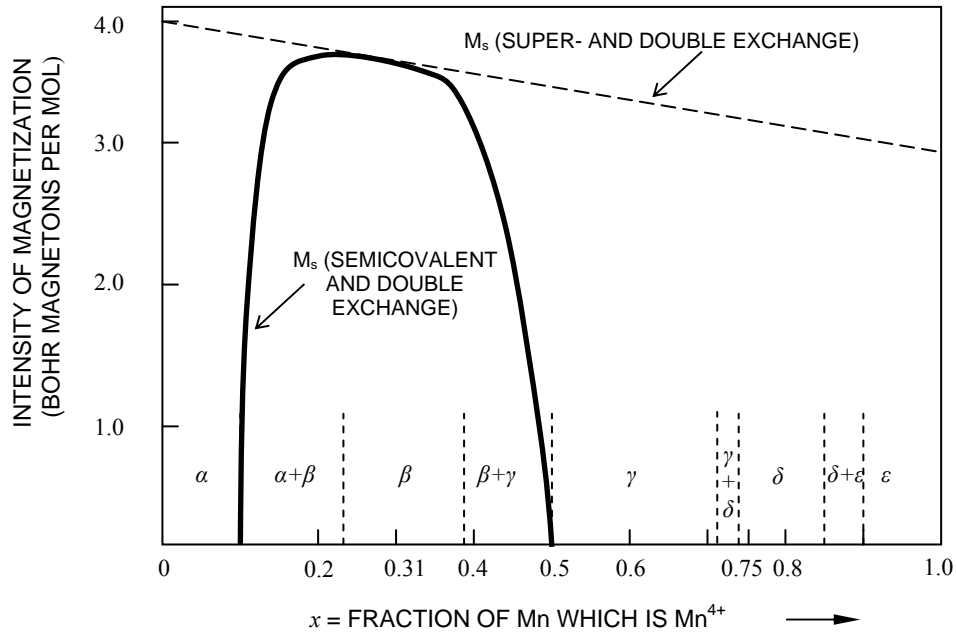


Figure 2-4. Predicted magnetization of perovskite-type manganites with covalent bond and *semicovalent* exchange model (from [14]).

Especially in the β region ($0.25 < x < 0.375$), the disordered lattice (= *cubic structured*) has a relatively high Curie temperature. Moreover, low resistivity of the disordered lattice occurs due to *metallic*-like bonding. Therefore, due to the maximum Curie temperature and minimum resistivity related to double-exchange mechanism, the optimized point of the double-exchange mechanism must be at a certain composition. This optimized point occurs in a certain disordered composition where the largest number of Mn^{+3} ions bring to only one Mn^{+4} ion. The optimum value of $x = 0.31$ was obtained by the calculation of the largest number of Mn^{+3} with only one Mn^{+4} ion in a random matrix of Mn^{+4} and Mn^{+3} [14].

Wollan *et al* intensively studied magnetic structure series of $\text{La}_{1-x}\text{Ca}_x\text{MnO}_3$ by neutron diffraction method [15]. They classified the magnetic structure as followed: type-*A*, *B*, *C*, *D*, *E*, *F* and *G*. Also, Ling *et al* explained the magnetic structures of $\text{La}_{2-2x}\text{Sr}_{1+2x}\text{Mn}_2\text{O}_7$ with following schematic illustrations for anti-ferromagnetic (AF), ferromagnetic (F), anti-ferro insulating (AFI)-type *A*, AFI-type *C*, AFI-type *C** and AFI-type *G* [16]. Fig. 2-5 shows the schematics of magnetic structures of manganite films.

Table II. Prediction of structural, magnetic and electrical properties of perovskite manganite oxides. x is the fraction of Mn^{+4} ion (from [14]).

Phase	Structure	Magnetic property	Electrical resistivity (ρ)
α	orthorhombic	anti-ferro (AF)-type A ($T_o^* > T_c = T_{cs}^{**}$ at $x = 0$)	High
$\alpha+\beta$	orthorhombic + cubic	AF-type A + ferro (F)	As x increases, 1) T_o decreases; 2) T_c increases; 3) ρ decreases sharply
β	cubic (rhombohedral possible)	F	Low
$\beta+\gamma$	cubic + tetragonal I ¹⁾	F + AF-type CE	max T_c and min ρ around $x = 0.3$
γ	tetragonal I	AF-type CE	High
$\gamma+\delta$	tetragonal I + tetragonal II ²⁾	AF-type CE and C	high
δ	tetragonal II	AF-type C	high
$\delta+\varepsilon$	tetragonal II + cubic	AF-type C and G	high
ε	cubic	AF-type G	high

¹⁾ tetragonal I ($c/a < 1$)²⁾ tetragonal II ($c/a > 1$)^{*)} T_o is the covalent bond ordering temperature^{**)} T_{cs} is Curie temperature for *semicovalent* exchanges

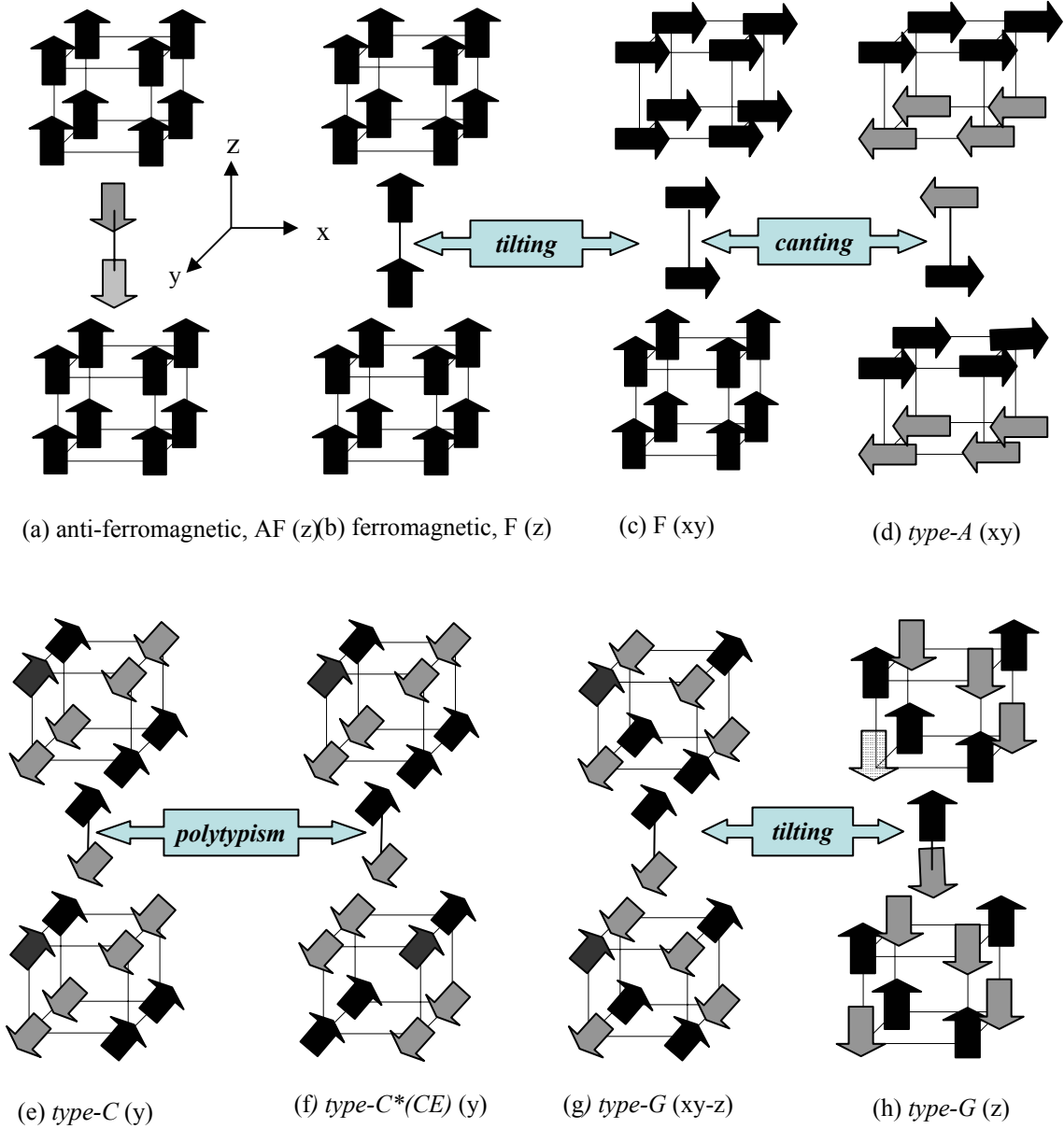


Figure 2-5. Magnetic structures of perovskite CMR manganites. The arrows represent spin orientation of Mn ion sites (a) anti-ferromagnetic, AF (b) ferromagnetic, F ($x = 0.3$) (c) F at $x = 0.4$ (d) anti-ferro-insulating, AFI type-A (e) AFI type-C (f) AFI type-C*(CE) (g) AFI type-G and (h) AFI type-G at $x = 1$ (from [15, 16]).

2.3 Structural tolerance factor

To understand the relation between structural and electrical properties of manganite films, Whang *et al* investigated structural-electrical correlation of CMR manganite films using T_c and tolerance factor (TF) given by [17]

$$TF = \frac{d_{(A_{0.7}A_{0.3})-O}}{\sqrt{2} \cdot d_{Mn-O}} \quad (2-5)$$

where $d_{(A_{0.7}A'_{0.3})-O}$ is the distance between A site ($A_{0.7}A'_{0.3}$) and oxygen (O) ions and d_{Mn-O} is for the distance between Mn and O ions.

Higher maximum T_c can be obtained in the range of $TF = 0.93$ in Fig. 2-6. Because the corresponding ionic radii are around 1.24 Å, $La_{0.7}Sr_{0.3}MnO_3$, $La_{0.7}(Ca,Sr)_{0.3}MnO_3$, $La_{0.7}(Sr,Ba)_{0.3}MnO_3$ and $La_{0.7}(Sr,Ba)_{0.3}MnO_3$ will be promising candidates for room temperature devices.

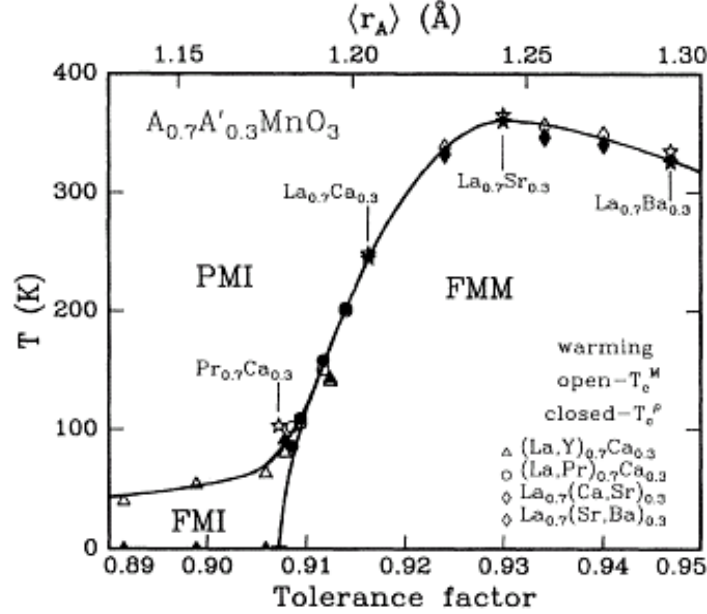


Figure 2-6. Phase diagram of temperature versus tolerance factor for $A_{0.7}A'_{0.3}MnO_3$ (after [17]).

2.4 Strain effect on CMR manganites

The electrical and magnetic properties are related to the lattice mismatch including a lattice deformation of films. The lattice mismatch between substrate and thin films can be defined by

$$\delta = \frac{a_{\text{substrate}} - a_{\text{bulk_film}}}{a_{\text{substrate}}} \quad (2-6)$$

In case of $a_{\text{substrate}} > a_{\text{bulk_film}}$, positive values imply tensile strain on the deposited films where the film layer is elongated inside the *in-plane* direction and compressed along the *out-of-plane*.

In the opposite case, negative values represent compressive strain and the unit cells of films must be stretched along the perpendicular direction of the film surface whereas shrunk in the film's plane.

The conceptual schematic of strain effects induce by substrates are shown in Fig. 2-7.

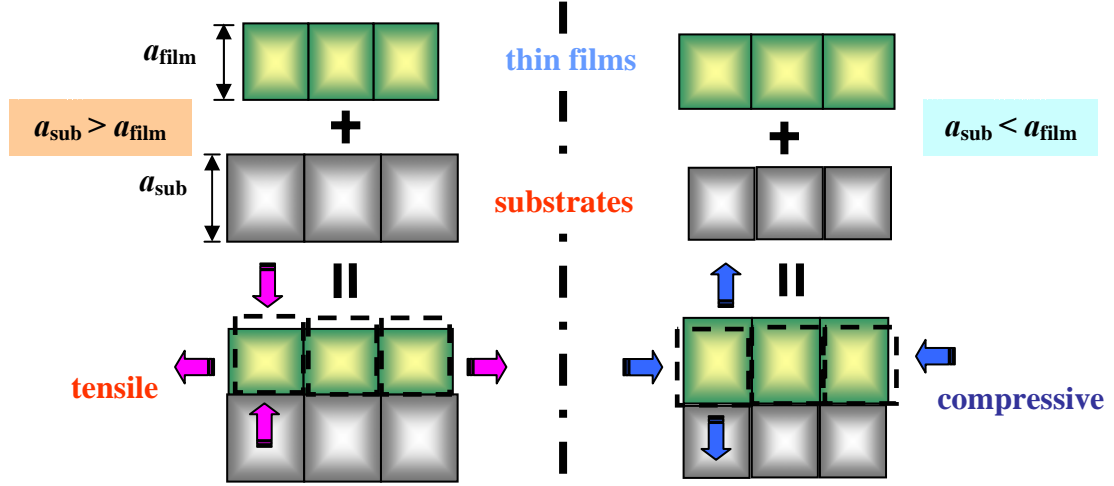
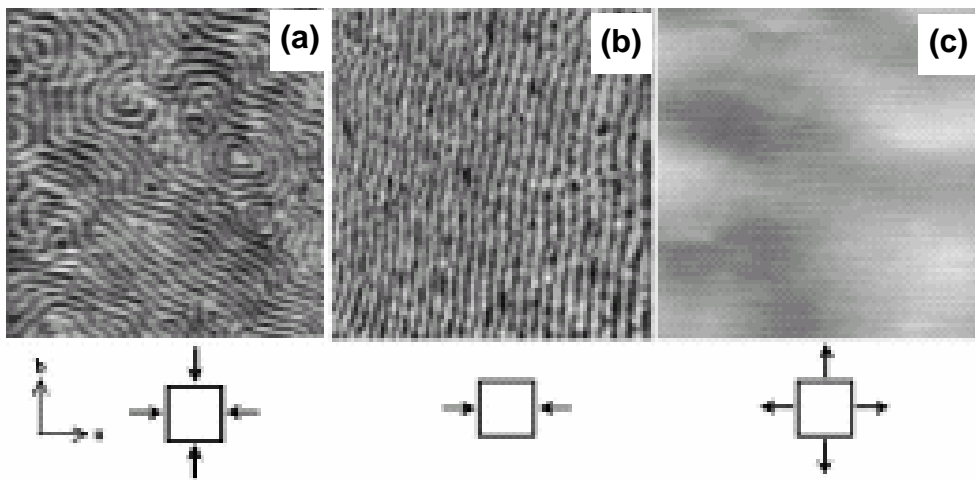


Figure 2-7. Tensile or compressive strains on epitaxial films induced by substrates.

$\text{La}_{0.7}\text{Sr}_{0.3}\text{MnO}_3$ films on SrTiO_3 (STO), lattice mismatch δ is 0.81%, have the smallest and tensile strain. These LSMO films on STO show single crystalline relation by perfect epitaxial growth. In case of LaAlO_3 (LAO), $\delta = 2.2\%$ compressive, it also shows single crystal relation except *in-plane* or *out-of-plane* dislocation-like defects [18]. According to the different strain types, compressive or tensile, on $\text{La}_{0.7}\text{Sr}_{0.3}\text{MnO}_3$ films, magnetic domains have different patterns from *feather-like* to *maze-like* strips, shown in Fig. 2-8 [19, 20]. According to moderate value of stress induced by substrate with $\text{La}_{0.5}\text{Ca}_{0.5}\text{MnO}_3$ (LCMO) on Si and oxide substrates, Rubi *et al* reported formations of ferromagnetic (F) domains and metallic percolate path [21]. Moreover, Lin *et al* investigated the dielectric constant change and tenability of $(\text{Pb,Sr})\text{TiO}_3$ film by induced anisotropic strain [22]. For thickness dependency of manganite films, Abrutis *et al* studied structural, electrical and magnetic properties of LSMO on LAO, NdGaO_3 (NGO) and STO, shown in Fig. 2-9 [23].


 Figure 2-8. Magnetic force microscopic (MFM) images of (a) *feature-like* domain on LaAlO_3 (b) *anisotropic* domain on NdGaO_3 (c) *maze-like* domain on STO (from [20]).

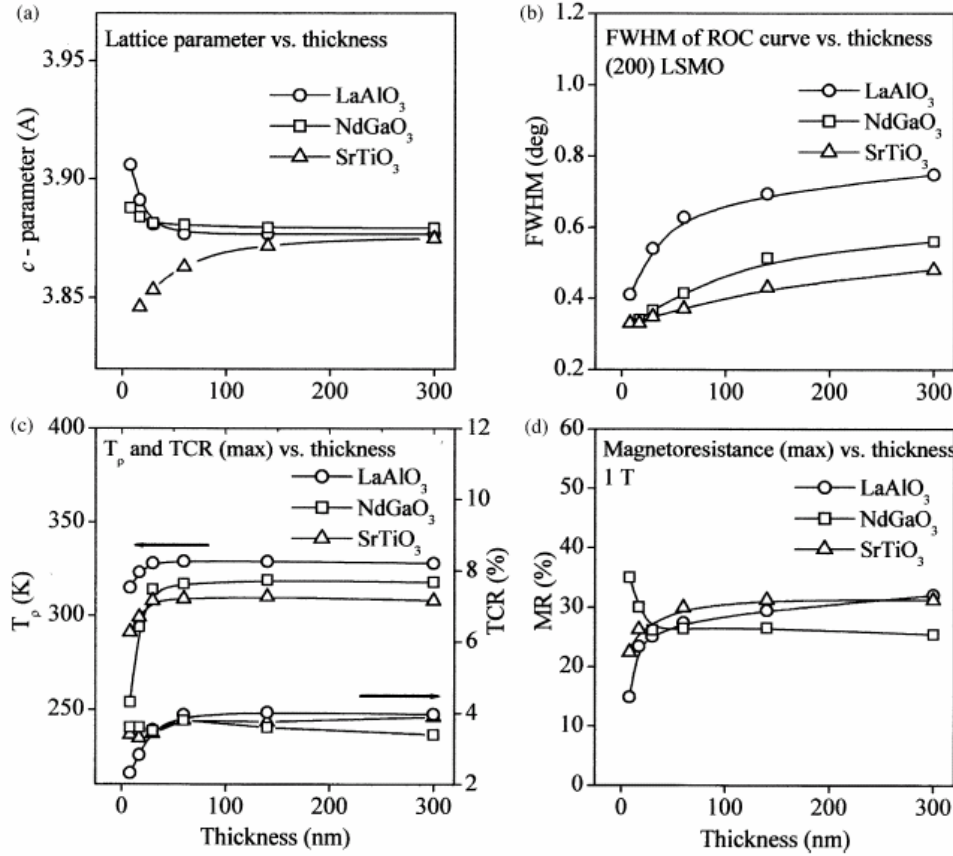


Figure 2-9. The substrate and thickness effects on structural, electrical and magnetic properties of $\text{La}_{1-x}\text{Sr}_x\text{MnO}_3$ films (from [23]).

2.5 Device applications of manganites

In spite of intensive fundamental studies for CMR manganites in 1950's and 1960's, there are not so many publications for device applications mainly due to the large lattice mismatch between manganites to semiconductor substrates, difficulty of film growth and lack of fabrication experiments. Recently, in order to utilize their metal-semiconductor transition and CMR effect of thin manganite films, the device-related works have been intensively investigated and appeared from last 10 years.

Gosnet *et al* and Venkatesan *et al* classified device applications of CMR manganite thin films [13, 24].

- **magnetic application**: spin valve, vertical and planar junctions for non-volatile memory and microwave application using colossal magnetoresistive properties ($\text{MR} = 1/\rho \cdot d\rho/dH$)
- **electrical application**: SrTiO_3 gate and ferroelectric gates in field effect transistor.
- **bolometric application**: metal to semiconductor transition (high temperature coefficient of resistivity)

■ low temperature hybrid high temperature superconducting: CMR devices

The conventional memory, dynamic random access type (DRAM) and static random access one (SRAM), have one critical problem. They are volatile! To retain data in the memory, the power consumption for refreshing it periodically, is necessary because of leakage current in circuits. Spin polarization of thin manganite films can be applied for magnetic random access memory (MRAM). The main advantage of MRAM is nonvolatile characteristics. Lu *et al* demonstrated the switching of CMR $\text{La}_{0.7}\text{Sr}_{0.3}\text{MnO}_3(500 \text{ \AA})/\text{STO}(60 \text{ \AA})/\text{La}_{0.7}\text{Sr}_{0.3}\text{MnO}_3$ junction with maximum 83 % of MR ratio at low magnetic field [25]. Recently, Dumont *et al* investigated critical current reductions in LSMO/YBCO spin injector. They found the heating in the LSMO manganites, due to dissipation of the polarization current, results these current reduction [26].

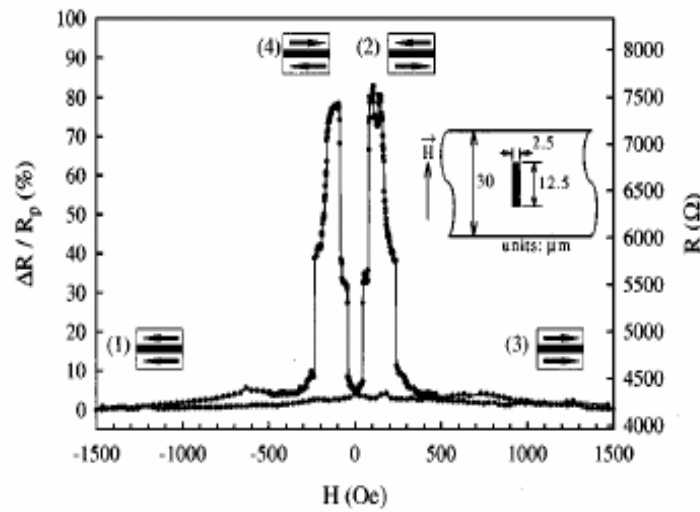


Figure 2-10. Tunneling electron microscopy image and corresponding MR ratio of $\text{La}_{0.7}\text{Sr}_{0.3}\text{MnO}_3/\text{SrTiO}_3/\text{La}_{0.7}\text{Sr}_{0.3}\text{MnO}_3$ vertical junction (after [25]).

Another application is the field effect transistor (FET). Using semiconductor channeling, the $\text{La}_{0.8}\text{Ca}_{0.2}\text{MnO}_3$ based-ferroelectric FET on silicon substrates was investigated by Zhao *et al*. Maximum 20% of modulation without magnetic field and 50% under 1 Tesla were obtained near the transition temperature [27].

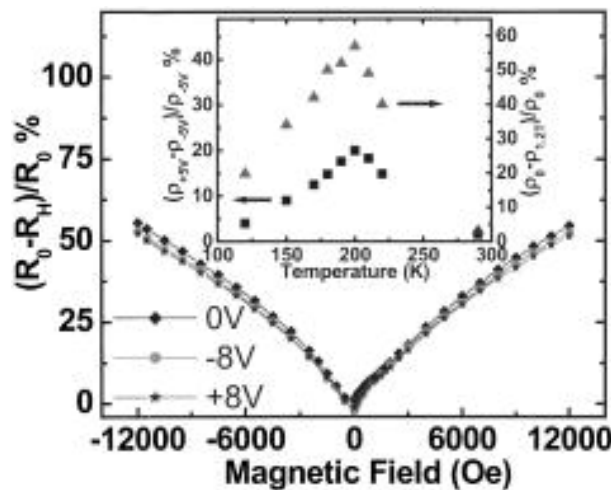


Figure 2-11. Ferro-electric field effect transistor. Schematic structure and magnetic field dependent MR at 200 K (after [27]).

Finally, making use of the large change of temperature dependant resistivity near T_c , uncooled infrared (IR) bolometer was considered at room temperature application. $7.4\% \cdot K^{-1}$ temperature coefficient of resistivity ($TCR = 1/\rho \cdot d\rho/dT$) of $La_{0.7}(Pr_{0.63}Sr_{0.37})_{0.3}MnO_3$ films on $LaAlO_3$ was demonstrated with relatively low excess noise by Lissauskas *et al* [28]. TCR is one of the main figure of merits for bolometric materials. In general, higher TCR values are achieved at low temperatures by materials such as $La_{0.67}Ca_{0.33}MnO_3$ (LCMO). High T_c with low TCR values was obtained in $La_{0.67}Sr_{0.33}MnO_3$ (LSMO) and $La_{0.67}Ba_{0.33}MnO_3$ (LBMO) on oxide substrates.

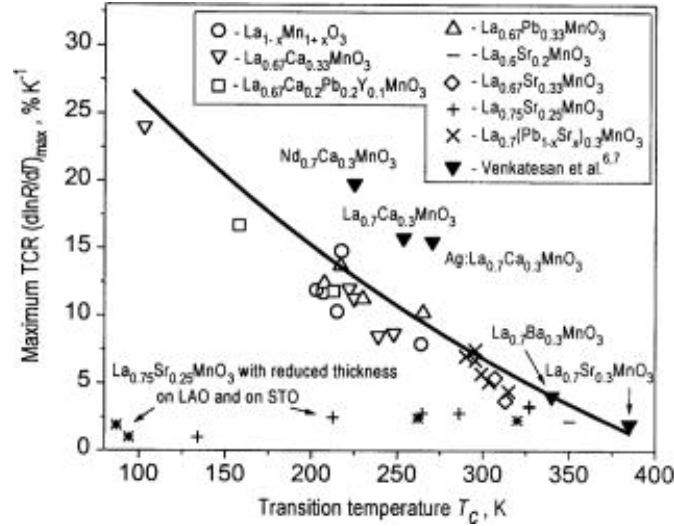


Figure 2-12. Maximum TCR values according to transition temperature T_c of manganite films for bolometric application (after [28]).

Achieving high TCR values at room temperature (RT) is the ultimate goal for bolometric application. Using alloying – fabrication of a continuous series of solid solutions taking two base compositions with T_c above - $La_{0.67}Sr_{0.33}MnO_3$ (LSMO) - and below - $La_{0.67}Ca_{0.33}MnO_3$ (LCMO) - room temperature, we demonstrated $La_{0.67}(Sr,Ca)_{0.33}MnO_3$ manganite films on Si substrates by central point combination of LCMO and LSMO for uncooled bolometric application [29].

References

- [1] G. H. Jonker and J. H. Van Santen, *Physica* **16**(3), 337 (1950).
- [2] J. H. Van Santen and G. H. Jonker, *Physica* **16**(7-8), 599 (1950).
- [3] Clarence Zener, *Phys. Rev.* **82**(3), 403 (1951).
- [4] J. L. Coln, *J. Supercond.* **13**(2), 291 (2000).
- [5] M. Fäth, S. Freisem, A. A. Menovsky, Y. Tomioka, J. Aarts, J. A. Mydosh, *Science* **285**, 1540 (1999).
- [6] T. Roch, S. Yaghoubzadeh, F. S. Razavi, B. Leibold, R. Praus, H.-U. Habermeier, *Appl. Phys. A* **67**, 723 (1998).
- [7] N. F. Mott and E. A. Daviers, *Electronic Process in Noncrystalline Solids*, 2nd ed. (Oxford University Press, New York, 1979); N. F. Mott, Talyer and Francis, London, (1974).
- [8] M. Viret, L. Ranno, and J. M. D. Coey, *Phys. Rev. B* **55**(13), 8067 (1997).
- [9] N.-C. Yeh, R. P. Vasquez, D. A. Beam, C.-C. Fu, J. Huynh and G. Beach, *J. Phys.: Condens. Matter.* **9**, 3713(1997).
- [10] A. J. Millis, Boris I. Shraiman, and R. Mueller, *Phys. Rev. Lett.* **77**(1), 175 (1996).
- [11] M. Jhuang, W. Zhang, and N. Ming, *Phys. Rev. B* **56** (22), 14547 (1997).
- [12] P. W. Anderson and H. Hasegawa, *Phys. Rev.* **100** (2), 675 (1955).
- [13] A-M Haghiri-Gosnet and J-P Renard, *J. Phys. D: Appl. Phys.* **36**, R127 (2003).
- [14] J. B. Goodenough, *Phys. Rev.* **100** (2), 564 (1955)
- [15] E. O. Wollan, W. C. Koehler, *Phys. Rev.* **100** (2), 545 (1955).
- [16] C. D. Ling, J. E. Millburn, J. F. Mitchell, D. N. Argyriou, J. Linton, H. N. Bordallo, *Arxiv/cond-mat/0007253* (2000).
- [17] H. Y. Hwang, S.-W. Cheong, P. G. Radaelli, M. Marezio, and B. Batlogg, *Phys. Rev. Lett.* **75**(5), 914 (1995).
- [18] W. Prellier, Ph. Lecoeur, B. Mercey, *J. Phys.: Condens. Matter* **13**, R915 (2001).
- [19] C. Kwon, M. C. Robson, K.-C. Kim, J. Y. Gu, S. E. Lofland, S. M. Bhagat, Z. Trajanovic, M. Rajeswari, T. Venkatesan, A. R. Kratz, R. D. Gomez, and R. Ramesh, *J. Magn. Magn. Mater.* **172**, 229 (1997).
- [20] Joonghoe Dho, Y. N. Kim, Y. S. Hwang, J. C. Kim, and N. H. Hur, *Appl. Phys. Lett.* **82**(9), 1434 (2003).
- [21] D. Rubi, S. Duhalde, M. C. Terzzoli, G. Leyva, G. Polla, P. Levy, F. Parisi, R. R. Urbano, *Physica B* **320**, 86 (2002).
- [22] Y. Lin, X. Chen, S. W. Liu, C. L. Chen, Jang-Sik Li, Y. Lee, Q. X. Jia, A. Bhalla, *Appl. Phys. Lett.* **84**, 577 (2004).
- [23] A. Abrutis, V. Plausinaitiene, V. Kubilius, A. Teiserskis, Z. Saltyte, R. Butkute, J. P. Senateur, *Thin Solid Films* **413**, 32 (2002).
- [24] T. Venkatesan, M. Rajeswary, Zi-Wen Dong, S. B. Ogale, R. Ramesh, *Phil. Trans. R. Soc. Lond. A* **356**, 1661 (1998).
- [25] Yu Lu, X. W. Li, G. Q. Gong, G. Xiao, A. Gupta, P. Lecoeur, J. Z. Sun, Y. Y. Wang, V. P. Dravid, *Phys. Rev. B* **54**(12), R8357 (1996).
- [26] J. Dumont, M. Moraguès, B. Leridon, J. Lesueur, J. P. Contour, *Eur. Phys. J. B* **35**, 331 (2003).
- [27] T. Zhao, S. B. Ogale, S. R. Shinde, R. Ramesh, R. Droopad, J. Yu, K. Eisenbeiser, J. Misewich, *Appl. Phys. Lett.* **84**(5), 750 (2004).
- [28] Alvydas Laisauskas, S. I. Khartsev, A. Grishin, *Appl. Phys. Lett.* **77**(5), 756 (2000).
- [29] J.-H. Kim, S. I. Khartsev, A. Grishin, *Appl. Phys. Lett.* **82**(24), 4295 (2003).

3. Epitaxial CMR film growth

Due to industrial demands for high quality films with good electrical and magnetic properties, it is an important issue to grow epitaxial films on conventional semiconductor substrates. In general, there are several methods to grow CMR manganite films on different substrates. In this chapter, several epitaxial films growth techniques and substrates including corresponding buffer layers and strain effects will be discussed.

3.1 CMR manganite film growth techniques

3.1.1 Pulsed laser deposition

Pulsed laser deposition (PLD) technique is the most straightforward method to grow high quality perovskite materials due to the mechanical simplicity and stoichiometric transfer of the ceramic target material [1-3]. After the laser ablation in PLD process, the plume of melt ceramic part occurs and condenses on a heated substrate. Varying ablation energy, base vacuum level, background oxygen pressure, distance between target and substrate and the temperature of substrates can optimize the deposition rate and structural quality. Another advantage of PLD technique is direct monitoring of *cell-by-cell* growth by reflective high-energy electron diffraction (RHEED) pattern [4, 5]. In general, laser sources of PLD are used with KrF (248 nm) [6, 7], ArF (193 nm) [8, 9] and Nd-YAG (266 or 355 nm) [10]. The set-up of a PLD system is shown in Fig. 3-1. All CMR manganite samples in this thesis are prepared by the PLD technique.

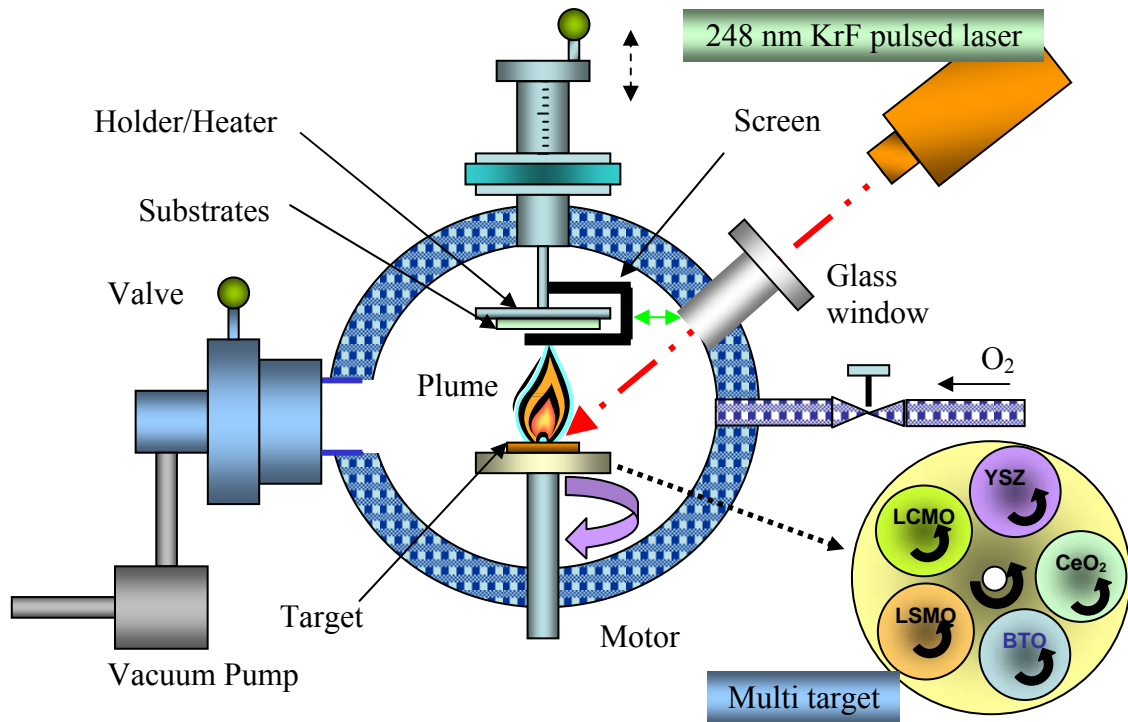


Figure 3-1. Pulse laser deposition (PLD) set-up with multi target.

3.1.2 Metal organic chemical vapor deposition

Metal organic chemical vapor deposition (MOCVD) technique can be utilized to grow different compositions of thin CMR manganite films. Recently, Gorbenko *et al* used single source MOCVD technique to grow $(\text{La,Pr})_{0.7}(\text{Sr,Ca})_{0.3}\text{MnO}_3$, $\text{La}_{0.5}\text{Sr}_{0.5}\text{CoO}_3$ and $\text{La}_{1-x}\text{Na}_x\text{CoO}_3$ [11, 12].

The principle of MOCVD is vaporization of sources. Vaporizer is generally used for vaporization process of liquid and solid precursors. To obtain stoichiometric CMR films, adjusting the mixture of precursors is very important parameter. Therefore, for precise control of evaporation rates and reproducibility of thin film quality, fine adjusting of temperature and pressure are necessary in MOCVD technique. The main obstacle of MOCVD for high temperature superconductor (HTS) and manganite oxides is the lack of thermally stable precursors.

3.1.3 Magnetron sputtering

Sputtering is the most widely used for commercial fabrication process in semiconductor industry. The main advantage of sputtering is that it is a *non*-thermal process. The basic concept of sputtering is ejection of surface atoms from the target surface by momentum transfer by bombarding ions. One of advantage of sputtering is to be utilized for etching process as well as deposition depending on the ion energy.

Radio frequency (RF) or DC magnetron sputtering techniques are other popular methods for growing high quality manganite films. Sputtering with transverse magnetic field has several advantages compared to other sputtering depositions: low heating of substrate, low radiation damage. Therefore, magnetron sputtering techniques are suitable for temperature sensitive or surface sensitive material deposition.

Grigorov *et al* investigated structure and stoichiometric composition of YBaCuO and LSMO films grown by magnetron sputtering on SrTiO_3 using Rutherford backscattering (RBS) and x-ray diffraction [14]. Also Park *et al* investigated magnetic properties of LCMO films grown by sputtering and sol-gel method [15].

3.1.4 Molecular beam epitaxy

Molecular beam epitaxy (MBE), called *element-by-element* growth technique, is utilized to grow sequential epitaxial CMR manganite films. The film composition can be properly selected by accurate control of atomic ratio of each metallic electron beam sources. The basic concept of MBE is that metallic sources are evaporated or sublimed from individual ovens into an ultra-high vacuum chamber. The beam of the source is directed onto the substrate. The growth rate is about one monolayer per second, and shutters in front of the various sources can be opened and closed to control the growth [16].

Nikolaev *et al* demonstrated a heterostructure consisting of CMR ferromagnetic $\text{La}_{2/3}\text{Ba}_{1/3}\text{MnO}_3$ and paramagnetic LaNiO_3 spacers by MBE technique [17]. O'Donnell *et al* investigated anisotropic magnetoresistances of MBE grown LCMO films. They showed that the magnetoresistance depends on the angle between electrical transport current and magnetization [18].

3.1.5 Sol-gel technique

Without high vacuum environment, thin manganite films can be grown by the sol-gel method. Sol-gel is a chemical solution based deposition where precursors are mixed in a solution and through hydrolysis and condensation, finally a sol is formed. After that, this sol is spin coated on substrates and becomes a gel thin film. By optimized heat treatment, crystallized manganite films on substrate can be obtained. This technique is suitable for large area film deposition.

Shankar *et al* demonstrated the $\langle 110 \rangle$ directed stoichiometric LSMO nanowire grown by sol-gel method [19]. In addition, monolithic LCMO nanowire on nano channel alumina (NCA) was investigated by Ma *et al* [20].

3.2 Substrates and buffer layers

To grow an epitaxial manganite film, the substrate should meet the following requirements: (i) minimize lattice mismatch between manganite film ($c \sim 3.8\text{-}3.9 \text{ \AA}$) and substrate (ii) match film-substrate thermal expansion coefficients, (iii) eliminate the chemical reaction between substrate and deposited films. The most common substrates for CMR manganite oxide is single crystal oxide such as, SrTiO_3 (STO), MgO , LaAlO_3 (LAO) and NdGaO_3 (NGO) [21-24].

However, single oxide crystal substrates are expensive and do not allow large size of growth. From an industrial viewpoint, silicon (up to 12" size for mass-production) and GaAs are the best candidates for CMR manganite thin films. However, semiconductor materials cannot comply with the above requirements. Therefore, template layers called buffer layers must be introduced to accommodate mechanical and chemical disaccords between CMR manganite films and semiconductor substrates.

3.2.1 CMR manganites on silicon substrates

Yttrium stabilized zirconia (YSZ) [25, 26], CeO_2 [27, 28] and $\text{Bi}_4\text{Ti}_3\text{O}_{12}$ (BTO) [26, 29] are selected as single or multi-buffer layers for silicon substrates. YSZ is widely used for protective buffering between Si and manganite/HTSC films, while BTO is found to be perfect for highly oriented growth due to its elongated c -axis (32.8 \AA). CeO_2 can improve the crystalline quality of BTO layer due to minimized lattice mismatch.

To get high TCR manganite films in room temperature, deposition of CMR manganite films was performed alternating stoichiometric $\text{La}_{0.67}\text{Sr}_{0.33}\text{MnO}_3$ (LSMO) and $\text{La}_{0.67}\text{Ca}_{0.33}\text{MnO}_3$ (LCMO) targets to compensate both higher TCR value in lower T_c and lower TCR in higher T_c (see Fig. 2-2). Finally, fabricated LSCMO/BTO/ CeO_2 /YSZ/Si heterostructure was *in-situ* post-annealed at 730°C for 5 minutes in 500 Torr of oxygen gas. Different cooling rate from 5 to $35^\circ\text{C}/\text{min}$ doesn't affect the CMR manganite film quality.

There is an *in-plane* relation "side-to-diagonal" match of BTO-to-LSMO/LCMO unit cells while "cube-to-cube" relations of substrate-to-BTO layer. Moreover, this additional buffer layer makes multi-layered structure very resistant against the thermal stress.

The optimized deposition conditions used on this work are listed in Table III. All layers were deposited without breaking the vacuum at target-to-substrate distance of 70 mm and a laser repetition rate of 20 Hz.

Table III. Optimized deposition conditions for growing of CMR manganite films.

Layer	Deposition conditions				
	Fluence (J/cm ²)	$T_{\text{substrate}}$ (°C)	P_{oxygen} (mTorr)	Rate (Å/pulse)	Thickness (Å)
YSZ	6	800	0.4	0.10	300
CeO ₂	6	750	1.5	0.13	400
Bi ₄ Ti ₃ O ₁₂	5	650	440	0.27	1000
La(Sr,Ca)MnO ₃	6	750	330	0.11	500

3.2.2 CMR manganites on GaAs

The growth of CMR manganite thin films on GaAs substrates is another big challenge. MgO is commonly used as a buffer layer due to its good insulating property and nice buffering for perovskite materials [30, 31]. Detailed deposition conditions of CMR LSMO and LCMO films are summarized in Table IV.

Table IV. Summary of deposition condition of LSMO and LCMO on GaAs.

Layer	Deposition conditions				
	Fluence (J/cm ²)	$T_{\text{substrate}}$ (°C)	P_{oxygen} (mTorr)	Rate (Å/pulse)	Thickness (Å)
MgO	5	590	200	0.12	700
La _{0.67} Ca _{0.33} MnO ₃	5	730	270	0.6	3500
La _{0.67} Sr _{0.33} MnO ₃	5	730	270	0.6	3500

Table V. Properties of selected materials for CMR manganite films.

	Material	crystal structure	lattice parameter (Å)	thermal extension coefficient (1/K) @ 300 °C**
	SrTiO ₃ (STO)	cubic	3.905	10.4×10^{-6}
	LaAlO ₃ (LAO)	<i>pseudo</i> -cubic	3.79	9.4×10^{-6}
substrate	NdGaO ₃ (NGO)	orthorhombic	5.43	1.1×10^{-5}
			5.50	
			7.71	
	Si	cubic	5.43	2.5×10^{-6}
	GaAs	cubic	5.65	5.4×10^{-6}
buffer	YSZ 77-2286*	cubic	5.14	10.3×10^{-6}
	CeO ₂ 04-0593*	cubic	5.41	-
	Bi ₄ Ti ₃ O ₁₂ (BTO) 80-2143*	orthorhombic	5.41, 5.43, 32.82	$\sim 11 \times 10^{-6}$
	MgO	cubic	4.21	$\sim 11 \times 10^{-6}$

3.3 Strain effect on CMR manganites using Si_{1-x}Ge_x and Si_{1-y}C_y layers on Si

Silicon-germanium (Si_{1-x}Ge_x) is an interesting material due to low cost and matured technology. The wide industrial applications in electronic and optoelectronic devices, including high frequency FET, optical detectors and laser, are available due to high carrier mobility and radiative recombination from strained thin Si_{1-x}Ge_x [32-34].

To investigate the influence of strain on the layer quality of LSMO films, both compressive Si_{1-x}Ge_x and tensile Si_{1-y}C_y layers can be applied on silicon substrates by choosing an appropriate Ge or C amount. The structural concept of Si_{1-x}Ge_x and Si_{1-y}C_y layers on Si is shown in Fig. 3-2.

Si_{1-x}Ge_x and Si_{1-y}C_y layers were grown on Si (100) substrates in the reduced pressure chemical vapor deposition (RPCVD) Epsilon 2000 ASM reactor. Si wafers were chemically cleaned using a standard procedure before they were loaded into the nitrogen-purged load locks. The growth temperature for Si_{1-x}Ge_x and Si_{1-y}C_y layers were 650 and 575 °C, respectively. To deposit Si_{1-x}Ge_x layers on Si substrate, silane (SiH₄) for silicon precursor and germane (GeH₄) for germanium were supplied with H₂ carrier gas. For Si_{1-y}C_y layer, silane and methyl-silane (SiH₃CH₃) were used.

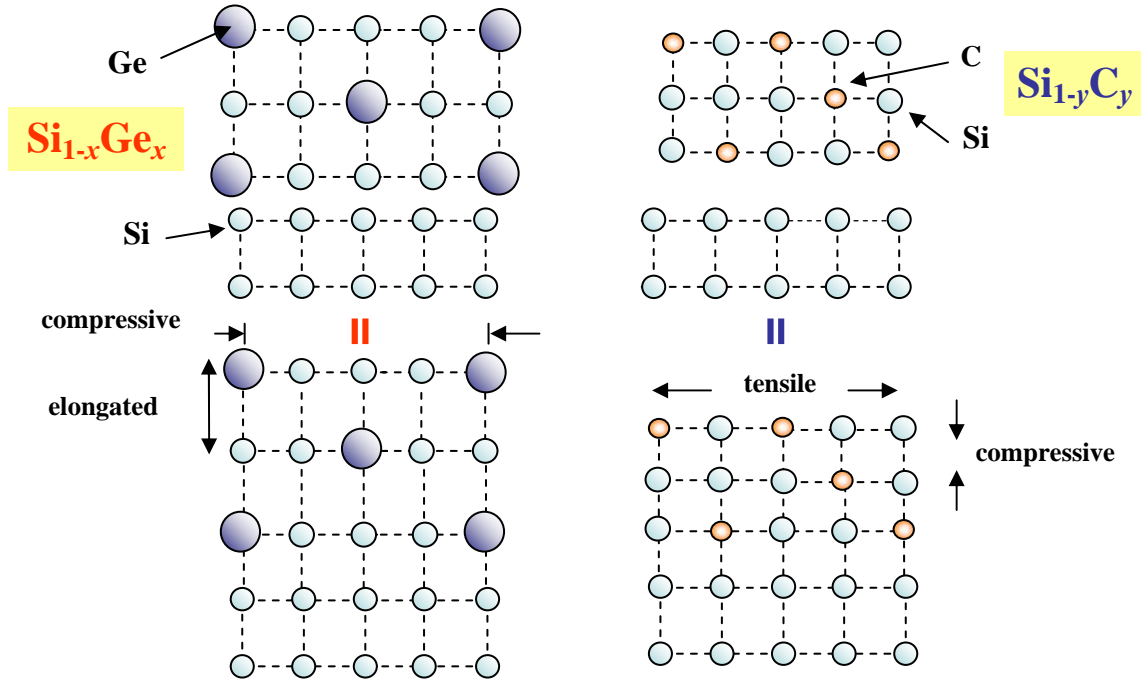


Figure 3-2. Concept of strain induced by $\text{Si}_{1-x}\text{Ge}_x$ and $\text{Si}_{1-y}\text{C}_y$ layers on Si substrate.

The peak positions and lattice parameters of $\text{Si}_{1-x}\text{Ge}_x$ and $\text{Si}_{1-y}\text{C}_y$ layers on Si substrates were determined by software (X'Pert Epitaxy 3a). The thickness of PRCVD grown $\text{Si}_{0.95}\text{Ge}_{0.05}$, $\text{Si}_{0.9}\text{Ge}_{0.1}$ and $\text{Si}_{0.8}\text{Ge}_{0.2}$ was 1050, 1030 and 1200 Å, respectively [39, 40].

After deposition of $\text{Si}_{1-x}\text{Ge}_x$ or $\text{Si}_{1-y}\text{C}_y$ layers on Si substrates, a stack of $\text{Bi}_4\text{Ti}_3\text{O}_{12}$ (100nm)/ CeO_2 (40nm)/YSZ (30nm) buffer layers was deposited and finally 50 nm thick $\text{La}_{0.75}\text{Sr}_{0.25}\text{MnO}_3$ films were grown by PLD technique at 750 °C and 400 mTorr of oxygen. After PLD process, heteroepitaxial film structure was *in-situ* annealed at 730 °C for 5 min in 500 Torr O_2 .

References

- [1] D. B. Chrisey and G. K. Hubler, *Pulse Laser Deposition of Thin Films*, John & Wiley & Sons, New York, (1993).
- [2] P. R. Willmott, *Progress in Surface Science* **76**, 163 (2004).
- [3] Wenbin Wu, K. H. Wong, C. L. Choy, *J. Phys. D: Appl. Phys.* **32**(15), L57 (1999).
- [4] C. Cantoni, D. K. Christen, M. Varela, J. R. Thompson, S. J. Pennycook, E. D. Specht, A. Goyal, *J. Mater. Res.* **18**(10), 2387 (2003).
- [5] Guus J.H.M. Rijnders, G. Koster, Dave H. A. Blank and H. Rogalla, *IEEE Tran. Appl. Supercond.* **9**(2), 1547 (1999).
- [6] D.-W. Kim, T. W. Noh, H. Tanaka, T. Kawai, *Solid State Comm.* **125**, 305 (2003).
- [7] R. J. Choudhary, A. S. Ogale, S. R. Shinde, S. Hullavarad, S. B. Ogale, T. Venkatesan, R. N. Bathe, S. I. Patil, R. Kumar, *Appl. Phys. Lett.* **84**(19), 3846 (2004).
- [8] H. Nishikawa, S. Hontsu, M. Nakamori, H. Tabata, T. Kawai, *IEEE Tran. Appl. Supercond.* **13**(2), 2725 (2003).
- [9] H. Oshima, Y. Ishihara, M. Nakamura, K. Miyano, *Phys. Rev. B* **63**, 094420 (2001).
- [10] M. Baran, S. L. Gnatchenko, O. Yu. Gorbenko, A. R. Kaul, *Phys. Rev. B* **60**(13), 9244 (1999).
- [11] O. Y. Gorbenko, A. R. Kaul, A. A. Molodyk, V. N. Fuflyigin, M. A. Novozhilov, A. A. Bosak, U. Krause, G. Wahl, *J. Alloy and Compound* **251**, 337 (1997).
- [12] M. Bibes, O. Gorbenko, B. Martínez, A. Kaul, J. Fontcuberta, *J. Magn. Magn. Mater.* **211**, 47 (2000).
- [13] T. Nakamura, R. Tai, T. Nishimura, K. Tachibana, *J. Appl. Phys.* **97**, 10H712 (2005).
- [14] K. Grigorov, V. Tsaneva, A. Spasov, W. Matz, R. Groetzschel, H. Reuther, *Vacuum* **69**, 315 (2003).
- [15] S.-I. Park, K. H. Jeong, Y. S. Cho, C. S. Kim, *J. Magn. Magn. Mater.* **242-245**, 692 (2002).
- [16] Krishna Seshan, *Handbook of Thin-Film Deposition Processes and Techniques*, 2nd ed., Noyes Publications, New York, (2002).
- [17] K. R. Nikolaev, A. Yu. Dobin, I. N. Krivorotov, W. K. Cooley, A. Bhattacharya, A. L. Kobrinskii, L. I. Glazman, R. M. Wentzovitch, E. Dan Dahlberg, A. M. Goldman, *Phys. Rev. Lett.* **85**(17), 3728 (2000).
- [18] J. O'Donnell, M. Onellion, M. S. Rzchowski, J. N. Eckstein, I. Bozovic, *J. Appl. Phys.* **81**(8), 4961 (1997).
- [19] K. Shantha Shankar, A. K. Raychaudhuri, *Nanotechnology* **15**, 1312 (2004).
- [20] X. Ma, H. Zhang, J. Xu, J. Niu, Q. Yang, J. Sha, D. Yang, *Chem. Phys. Lett.* **363**, 579 (2002).
- [21] A. Goyal, M. Rajeswari, R. Shreekala, S. E. Lofland, S. M. Bhagat, T. Boettcher, C. Kwon, R. Ramesh, and T. Venkatesan, *Appl. Phys. Lett.* **71**(17), 2535(1997).
- [22] A. Laisauskas, J. Bäck, S. I. Khartsev, A. M. Grishin, *J. Appl. Phys.* **89**, 6961 (2001).
- [23] L. Meda, K. H. Dahmen, S. Hayek, H. Garmestani, *J. Crystal Growth* **263**, 185 (2004).
- [24] A. M. Haghiri-Gosnet, J. Wolfman, B. Mercey, Ch. Simon, P. Lecoeur, M. Korzenski, M. Hervieu, R. Desfeux, G. Baldinozz, *J. Appl. Phys.* **88**(7), 4257 (2000).

- [25] P.-J. Kung, D. B. Fenner, D. M. Potrepka, J. I. Budnick, *Appl. Phys. Lett.* **69**(3), 427 (1996).
- [26] Z. Trajanovic, C. Kwon, M. C. Robson, K.-C. Kim, M. Rajeswari, R. Ramesh, T. Venkatesan, S. E. Lofland, S. M. Bhagat, D. Fork, *Appl. Phys. Lett.* **69**(7), 1005 (1996).
- [27] A. L. Vasiliev, G. V. Tendeloo, Yu Boikov, E. Olsson, Z. Ivanov, *Supercond. Sci. Technol.* **10**, 356 (1997).
- [28] V. Trtik, C. Ferrater, F. Sánchez, M. Varela, J. Fontcuberta, M. Bibes, B. Martínez, *J. Crystal Growth* **209**, 842 (2000).
- [29] T. Ami, M. Suzuki, *Mater. Sci. Eng. B* **54**, 84 (1998).
- [30] H. Shimakage, A. Kawakami, Z. Wang, *IEEE Tran. Appl. Supercond.* **9**(2), 1645 (1999).
- [31] S. I. Khartsev, J.-H. Kim, A. M. Grishin, *J. Crystal Growth*, **284**, 1 (2005).
- [32] V. Ligatchev, T. K. S. Wong, S. F. Yoon, *J. Appl. Phys.* **95**(12), 7681 (2004).
- [33] E. Koppensteiner, G. Bauer, H. Kibbel, and E. Kasper, *J. Appl. Phys.* **76**(6), 3489 (1994).
- [34] J. P. Dismukes, L. Ekstrom, E. F. Steigmeier, I. Kudman, and D. S. Beers, *J. Appl. Phys.* **35**(10), 2899 (1964).

4. Characterization of CMR manganite films

4.1 X-ray diffraction

Diffraction is a coherent and elastic scattering phenomenon of an incident electromagnetic wave. A diffracted beam can be defined as a beam composed of a large number of scattered rays mutually reinforcing one another. Therefore, x-ray diffraction (XRD) is useful method to identify crystal structure and investigate thin film crystalline quality by detecting the diffracted x-ray. Early, Bragg investigated a crystal pattern and formulated the relation called Bragg's law given by [1].

$$2d \cdot \sin \theta = n\lambda \quad (4-1)$$

where d is distance between parallel planes of crystal, λ is the wavelength of x-ray source and θ is the angle between incident x-ray beams and crystal plane. Generally, reflected order n is 1. Fig. 4-1 shows a schematic of Bragg diffraction condition.

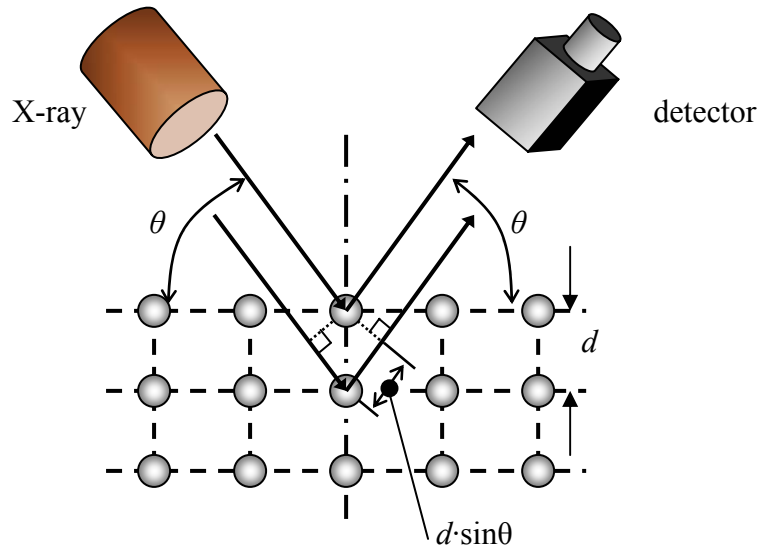


Figure 4-1. Schematic of X-ray Bragg diffraction.

In our study, to investigate the highly epitaxial grown LSMO, LCMO and LSCMO films, XRD measurements were executed with powder diffractometer Siemens D5000 (Cu $K\alpha$) and high resolution system Philips MRD X'Pert (Cu $K\alpha_1$, $\lambda = 1.54056 \text{ \AA}$). Here three major scans of XRD are explained (see Fig. 4-2).

- **θ - 2θ scan:** It provides (i) crystal orientation of substrate and thin films (ii) lattice parameter (iii) film thickness.
- **ω scan:** Crystal texturing or mosaic of thin films can be investigated by this measurement.

■ ϕ scan: It is used to reveal the relation between layer and substrates or layers and under-lying layers. Oblique planes of layer and substrate were commonly used to determine in-plane orientation

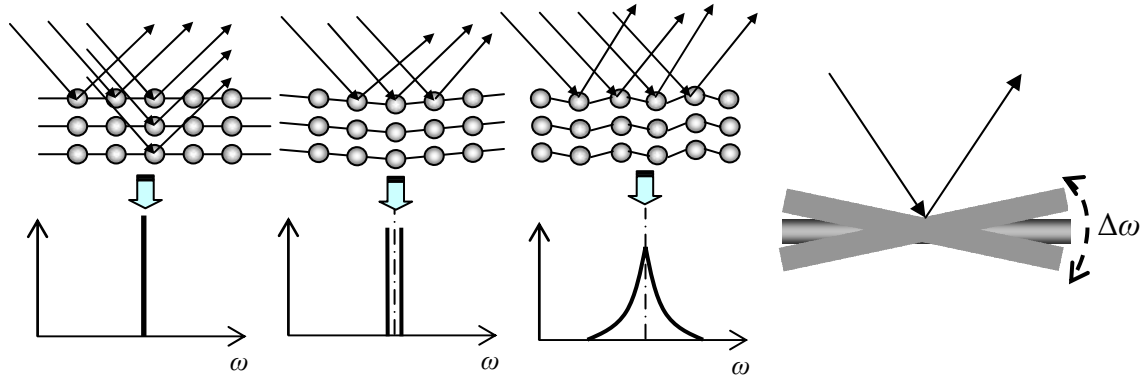


Figure 4-2. Concept of rocking curve measurement by XRD.

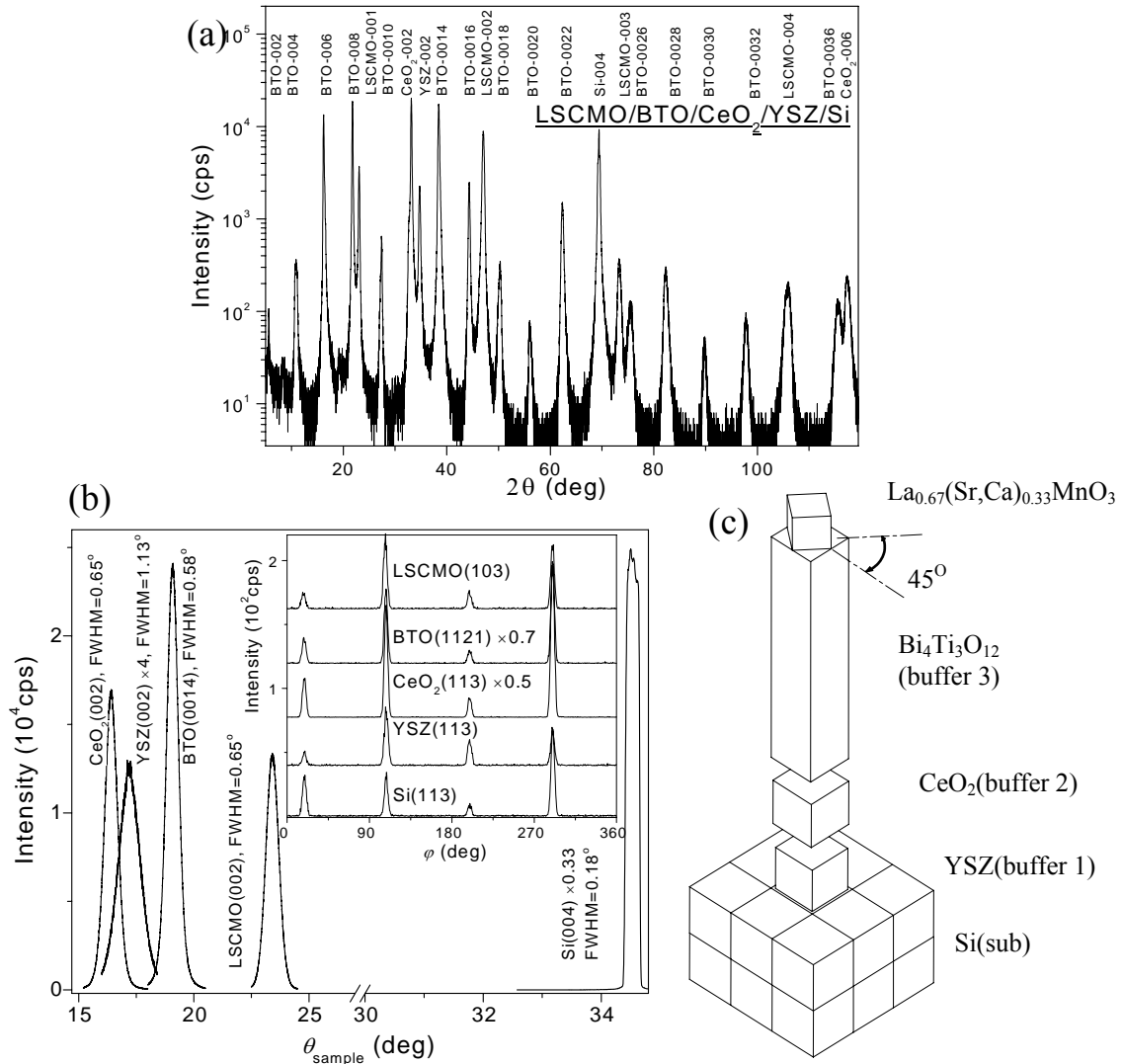


Figure 4-3. X-ray diffraction results of $\text{La}_{0.67}(\text{Sr,Ca})_{0.33}\text{MnO}_3/\text{Bi}_2\text{Ti}_2\text{O}_2/\text{CeO}_2/\text{YSZ}$ on Si (a) θ - 2θ scan (b) rocking curve of each layers and substrate. Inset is ϕ scan (c) growth relation. All measurements was performed by Siemens D5000.

The measured θ - 2θ , ω and ϕ scans of PLD grown CMR LSCMO/BTO/CeO₂/YSZ films on Si are shown in Fig. 4-3. The θ - 2θ measurement shows strong (00 l) orientation for all oxide layers with no other peaks. From (113) and (103) oblique ϕ scans, sequential relations - “cube-on-cube” of YSZ-CeO₂-BTO and “diagonal-on-side” orientation of LSCMO-on-BTO unit cells are revealed. From here, LSCMO films on BTO layer are 45° rotated to minimize lattice mismatch ($3.8 \text{ \AA} \times \sqrt{2} \sim 5.43 \text{ \AA}$).

Growth of CMR La_{0.67}Ca_{0.33}MnO₃ (LCMO) and La_{0.67}Sr_{0.33}MnO₃ (LSMO) films on other semiconductor substrates *e.g.* GaAs were also investigated. The PLD-grown of LSMO and LCMO of the results of XRD measurements are shown in Fig. 4-4 and Fig. 4-5. Strong (00 l) orientations of LCMO and LSMO on MgO buffered GaAs are revealed including 45° rotation between MgO (113) and CMR films (103) crystal planes.

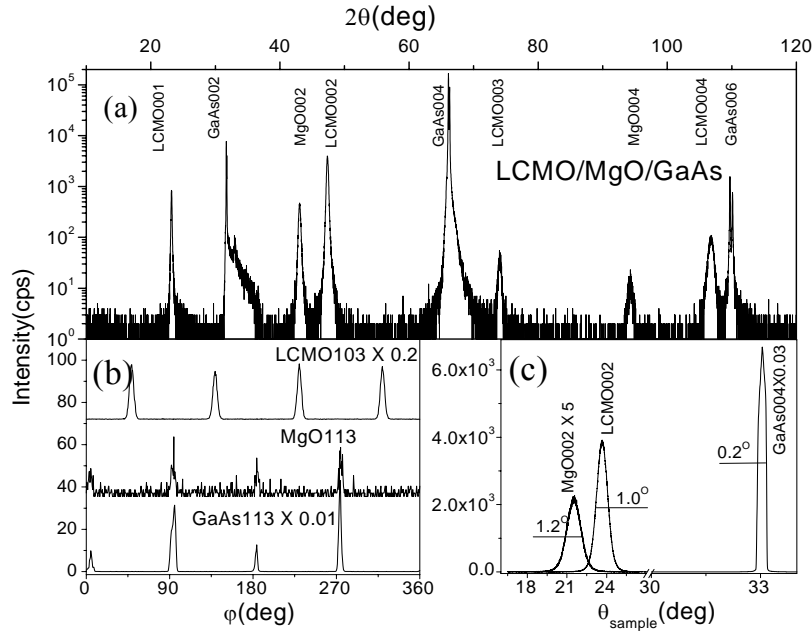


Figure 4-4. XRD of La_{0.67}Ca_{0.33}MnO₃ on GaAs with MgO buffer layers (a) θ - 2θ scan (b) ϕ scan (c) ω scan.

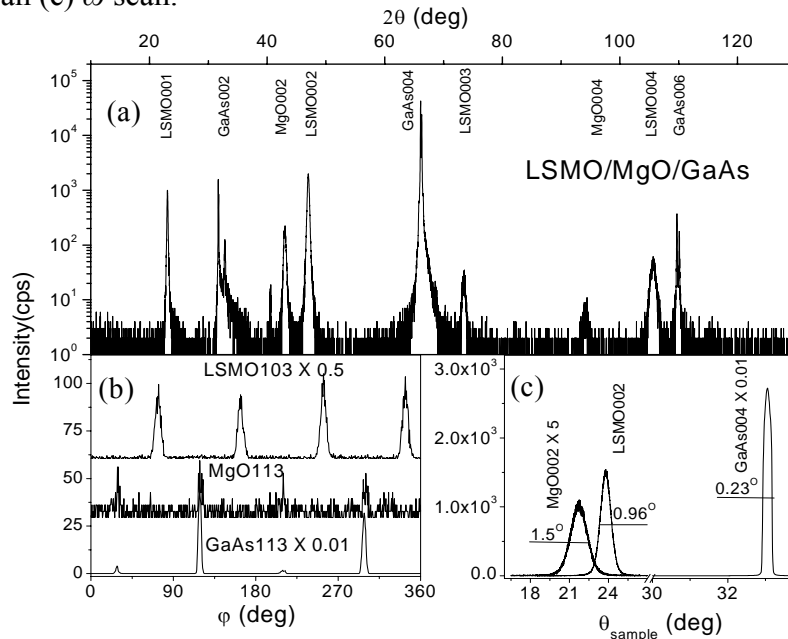


Figure 4-5. X-ray diffraction of various LSMO on MgO buffered GaAs (a) θ - 2θ scan (b) ϕ scan (c) ω scan. All measurements were performed by Siemens D 5000.

The evolution of layer quality of $\text{La}_{0.75}\text{Sr}_{0.25}\text{MnO}_3$, $\text{Si}_{1-x}\text{Ge}_x$ and $\text{Si}_{1-y}\text{C}_y$ layers are in Fig. 4-6 by $\omega/2\theta$ scan. Lattice parameter of the unstrained $\text{Si}_{1-x}\text{Ge}_x$ on Si can be calculated by the following equation [2, 3]

$$a_{\text{Si}_{1-x}\text{Ge}_x} = a_{\text{Si}} \cdot (1 - x) + a_{\text{Ge}} \cdot x - 0.0239x + 0.0196x^2 + 0.0044x^3 \dots (4-2)$$

where a_{Si} , a_{Ge} and x are lattice parameters of Si (= 5.4308 Å), Ge (= 5.5657 Å), and Ge contents of $\text{Si}_{1-x}\text{Ge}_x$, respectively.

The estimated lattice parameters of grown $\text{Si}_{0.95}\text{Ge}_{0.05}$, $\text{Si}_{0.9}\text{Ge}_{0.1}$ and $\text{Si}_{0.8}\text{Ge}_{0.2}$ layers in Fig. 4-6(a) are 5.441 Å, 5.451 Å and 5.472 Å, respectively, while 5.395 Å is obtained for $\text{Si}_{0.99}\text{C}_{0.01}$ as determined by software. After the PLD process of the $\text{La}_{0.75}\text{Sr}_{0.25}\text{MnO}_3/\text{BTO}/\text{CeO}_2/\text{YSZ}$ stack structures, the intensities of the $\text{Si}_{1-x}\text{Ge}_x$ and $\text{Si}_{0.99}\text{C}_{0.01}$ layer peaks in all RPCVD grown samples decreases. A significant increase of full-width-half-maximum (FWHM) values of the layer peaks with no layer fringes indicates a decrease of both $\text{Si}_{1-x}\text{Ge}_x$ layer and interface qualities shown in Fig. 4-6(b).

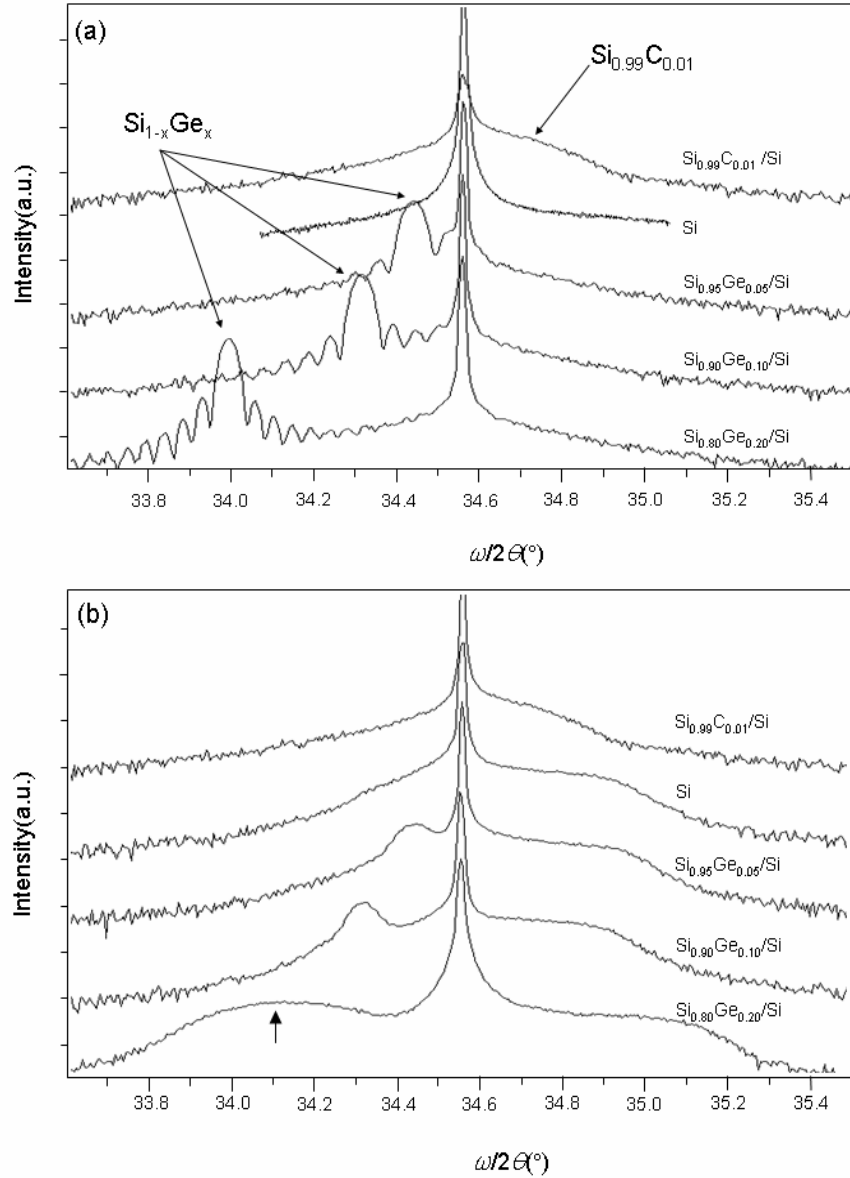


Figure 4-6. X-ray diffraction of $\text{Si}_{1-x}\text{Ge}_x/\text{Si}$, Si and $\text{Si}_{0.99}\text{C}_{0.01}/\text{Si}$. (a) as grown samples (b) after PLD process of LSMO/BTO/CeO₂/YSZ multi-structure.

The calculated shift (arrow marked) of the $\text{Si}_{0.8}\text{Ge}_{0.2}$ peak towards higher angle of $\omega/2\theta$ scan in Fig. 4-6(b) is $0.1302 \pm 0.002^\circ$, which indicates significant strain relaxation whereas all other $\text{Si}_{1-x}\text{Ge}_x$ and $\text{Si}_{1-y}\text{C}_y$ reflections occupy the same initial positions. Therefore, by post-oxygen annealing treatment after PLD, the $\text{Si}_{0.8}\text{Ge}_{0.2}$ layer may be relaxed since it is in meta-stable region whereas the $\text{Si}_{1-x}\text{Ge}_x$ layers with low Ge content are below the Matthew-Blackselee region [4].

4.2 Reciprocal lattice mapping (RLM)

Two-dimensional reciprocal lattice mapping (RLM) can be obtained by $\omega/2\theta$ scan for a range of incident angles $\omega \pm \Delta\omega$. From measured RLMs, relative positions and features of layer peaks compared to substrate peak can provide mismatch and defect density of layer. Moreover, an asymmetric reflection measurement is so sensitive to separation of overlapped peaks between substrate and layers or layer-to-layer due to similar lattice parameters [5]. Fig. 4-7 presents a reciprocal space of symmetric Si (004) and asymmetric Si (113) reflection measurements.

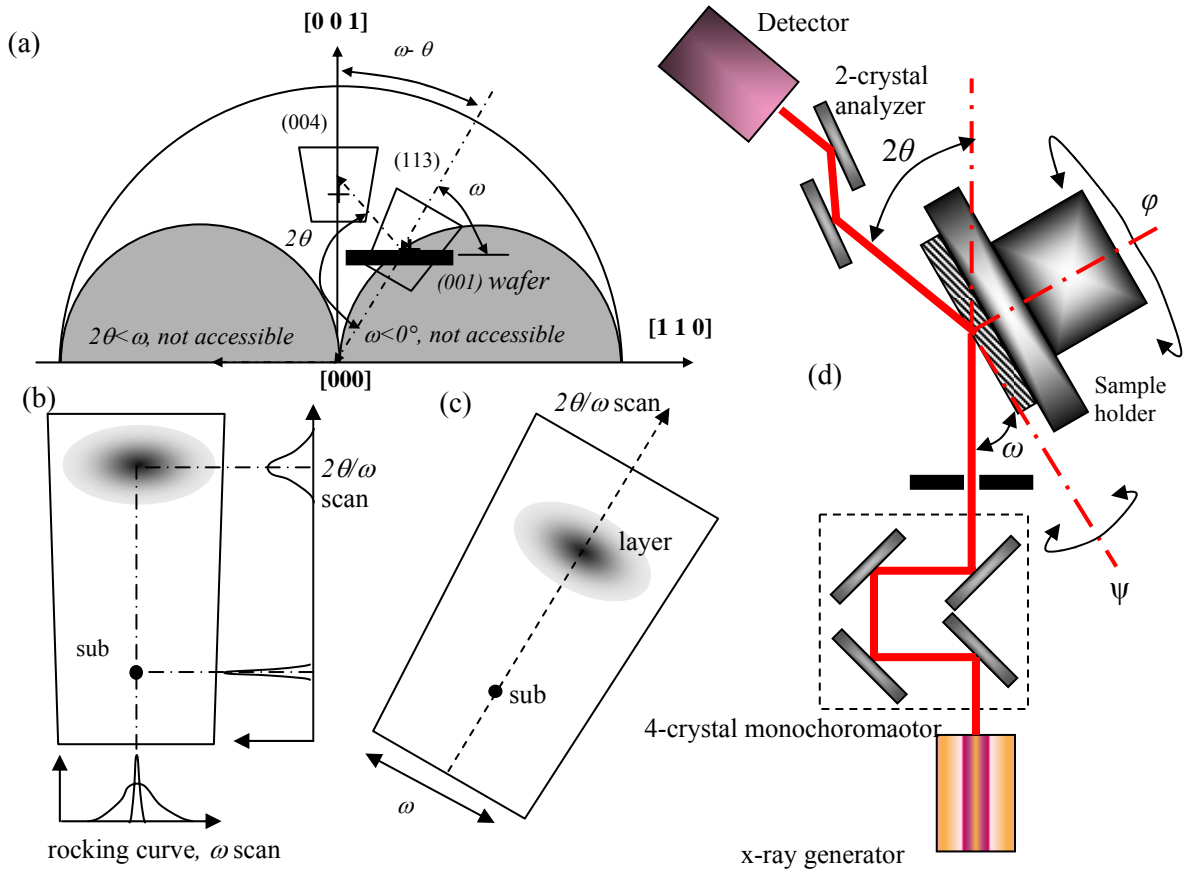


Figure 4-7. Schematic representation of (a) reciprocal lattice points of Si (001) wafer (b) symmetric (004) reflection (c) asymmetric (113) reflection (d) schematic of high resolution Philips MRD system.

The measured RLMs of $\text{La}_{0.67}(\text{Sr,Ca})_{0.33}\text{MnO}_3$ films on oxide-buffered Si substrates are shown in Fig. 4-8. In order to obtain a high intensity from these thin layers, the measurements were performed by applying only the receiving slit in the secondary optics. All of the LSCMO/BTO/CeO₂/YSZ layer peaks, around the (004) Bragg reflection in Fig. 4-8(a), have a highly *c*-oriented relations already shown in Fig. 4-3(a). Although layer peaks of CeO₂ (004) and YSZ (004) are overlapped, in Fig. 4-3(a) and 4-6(b), due to similar lattice parameter among Si, YSZ and CeO₂, they can be recognized by peak separation in asymmetric reflection in Fig. 4-8(b).

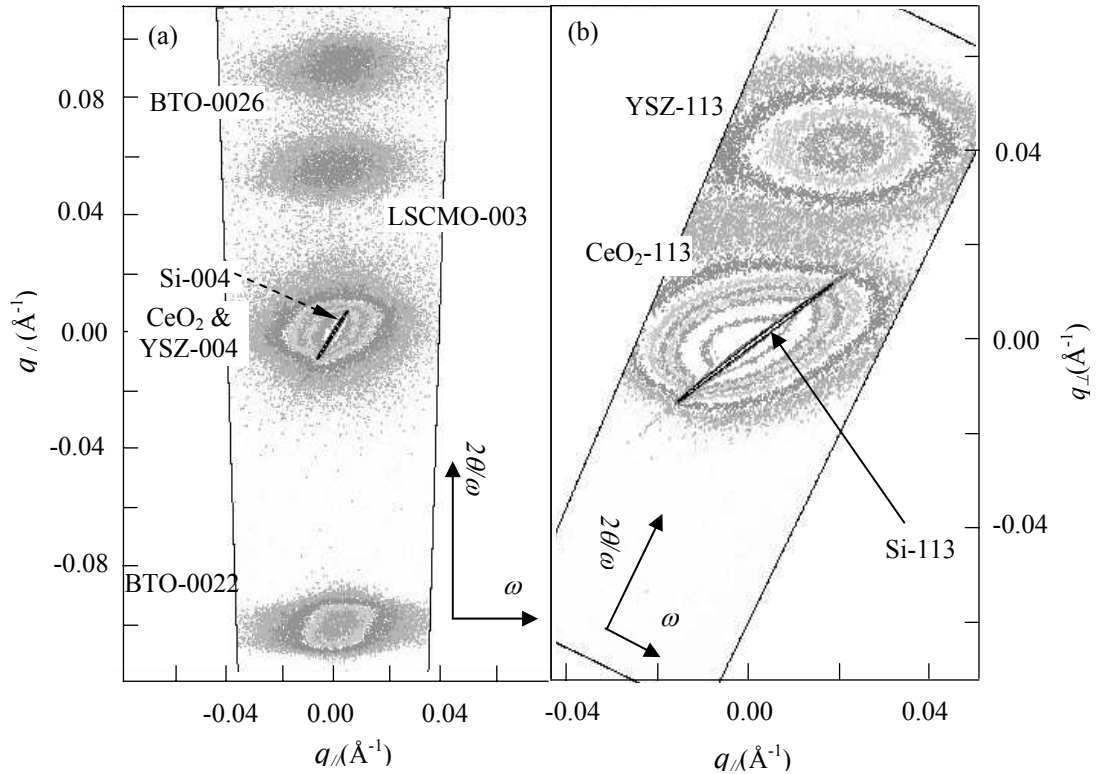


Figure 4-8. Reciprocal lattice mapping of $\text{La}_{0.67}(\text{Sr,Ca})_{0.33}\text{MnO}_3$ on oxide buffered Si substrate (a) symmetric (004) reflection (b) asymmetric (113) reflection.

In order to investigate the thermal stability of the LSCMO films on Si, rapid thermal annealing (RTA, Mattson RTP-100) were performed in N₂ gas ambient (10 sccm). The ramping speed and duration time were fixed by 50°C/sec and 10 sec, respectively. After RTA process, RLMs of LSCMO films on Si were measured and shown in Fig. 4-9. Under the condition of 800 °C, BTO peaks strongly related to the crystal quality of LSCMO films becomes better than as grown sample, however over 850 °C, many defects between LSCMO and Si peaks are easily recognized. These results may originate from the differences in thermal expansion of each layer.

Kanai *et al* investigated the annealing effect on out-of plane lattice parameter, *c* of $\text{La}_{0.8}\text{Ba}_{0.2}\text{MnO}_3$ on STO substrate. In higher annealing condition, over 900 °C, the *c*-parameter is changed drastically compared to lower temperature condition (below 800 °C) [6]. Moreover, they observed weakening of diffraction layer peaks as shown in Fig. 4-9(d).

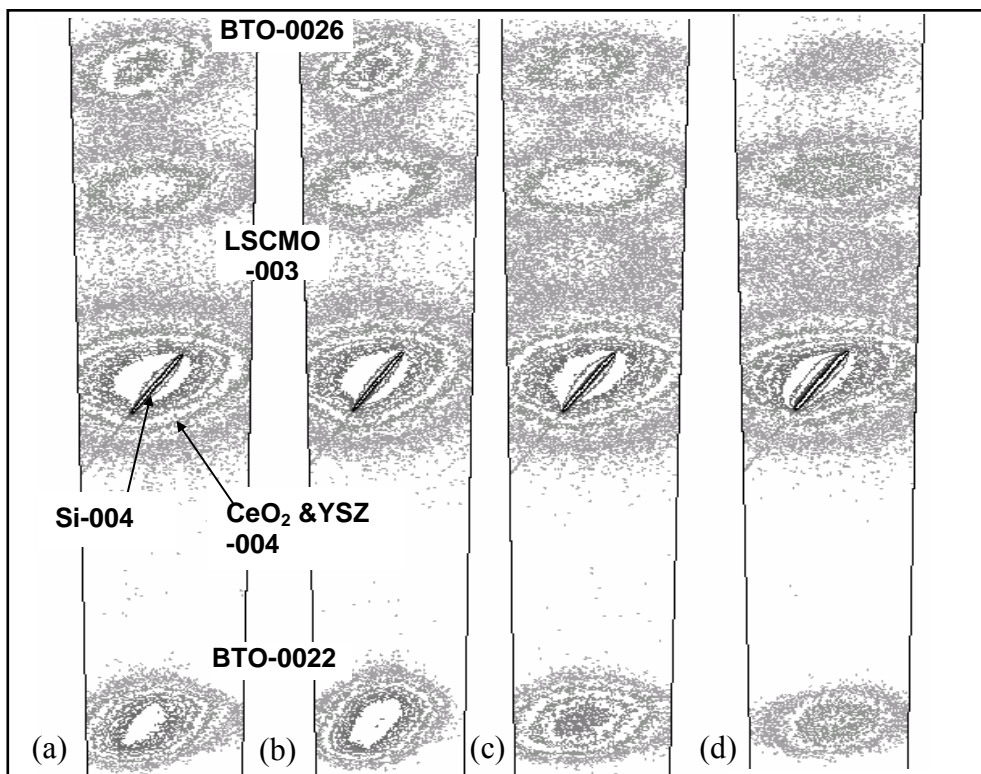


Figure 4-9. Rapid thermal annealing (RTA) effects of $\text{La}_{0.67}(\text{Sr,Ca})_{0.33}\text{MnO}_3$ films on oxide buffered Si substrate in N_2 gas. (a) as grown (b) 800 °C and 10 sec (c) 850 °C and 10 sec and (d) 900 °C and 10 sec. Ramping speed was fixed with 50 °C/sec.

For strain effects on structural properties of CMR manganite films, RLMs measurement can provide more information than conventional rocking curve measurement. Fig. 4-10 shows RLMs around Si (004) Bragg reflection of $\text{La}_{0.75}\text{Sr}_{0.25}\text{MnO}_3$ (LSMO) films on $\text{Bi}_4\text{Ti}_3\text{O}_{12}$ (BTO)/ CeO_2 /YSZ buffered $\text{Si}_{1-x}\text{Ge}_x/\text{Si}$ and $\text{Si}_{0.99}\text{C}_{0.01}/\text{Si}$. All the layers in the multilayer stack are distinguished by peak positions.

There is a clear difference in the intensity of the main contours and the shape of the BTO (0022) and LSMO (003) peaks shown in Fig. 4-10(a) and (b). The shape of BTO (0022) peaks changes from ellipsoid for both $\text{Si}_{0.8}\text{Ge}_{0.2}/\text{Si}$ and $\text{Si}_{0.99}\text{C}_{0.01}/\text{Si}$ samples in Fig. 4-10(a) and (d) to more rhombic shape for $\text{Si}_{0.9}\text{Ge}_{0.1}/\text{Si}$ and Si in Fig. 4-10(b)-(c). Due to no shift in the position of these peaks, in Fig. 4-10(b), therefore there is no change in c parameter of lattice. The shape changes of BTO layer is believed to be caused by alteration in a and b parameters (causing a change in biaxial strain). Consequently, from the strain modification in buffer layers, the LSMO layers in samples containing $\text{Si}_{0.99}\text{C}_{0.01}/\text{Si}$ and Si samples are more defined with higher intensity (less diffused). This is an indication of a decrease in defect density in these LSMO layers.

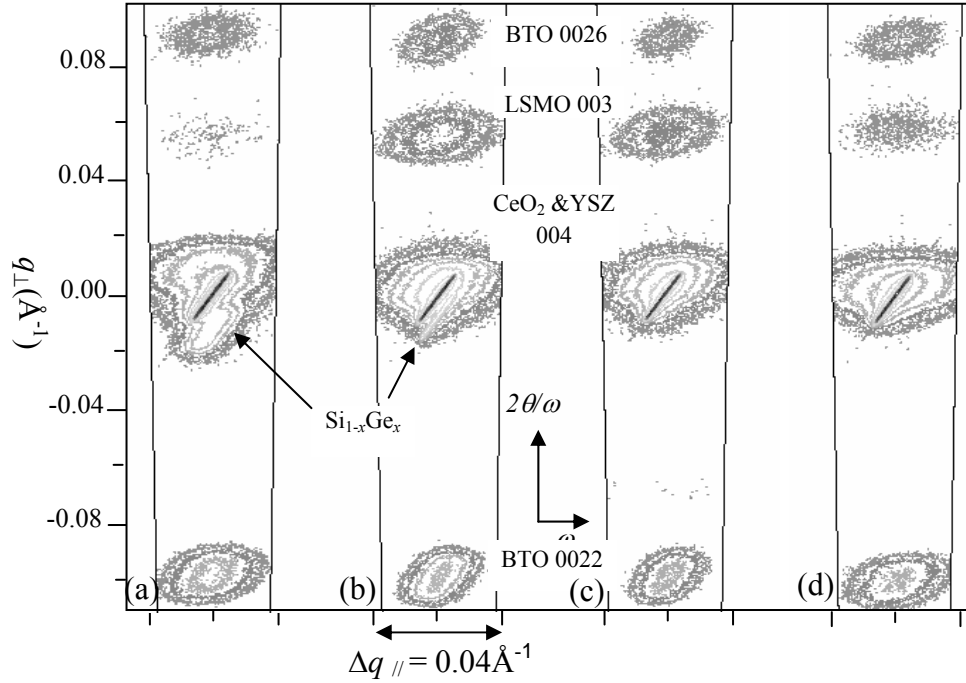


Figure 4-10. Strain effect of thin $\text{La}_{0.75}\text{Sr}_{0.25}\text{MnO}_3$ films on $\text{Bi}_4\text{Ti}_3\text{O}_{12}/\text{CeO}_2/\text{YSZ}$ buffered (a) $\text{Si}_{0.8}\text{Ge}_{0.2}/\text{Si}$ (b) $\text{Si}_{0.9}\text{Ge}_{0.2}/\text{Si}$ (c) Si and (d) $\text{Si}_{0.99}\text{C}_{0.01}/\text{Si}$.

4.3 Rutherford backscattering spectroscopy (RBS)

Rutherford backscattering spectroscopy (RBS), discovered in 1911, is used to investigate a stoichiometric composition of thin films and corresponding thickness.

The principle of RBS is energy detecting of the backscattered ions sprung from a target material by kinetic collision between source atom and target material. The number of the backscattered ions is proportional to the atomic number of the target elements.

Giesen *et al* investigated composition of LCMO/LSMO multilayer on MgO substrates with RBS experiment [7]. Park *et al* also studied RBS spectra and channeling measurement of La-Sr-Mn-O, La-(Ca,Sr)-Mn-O, La-Ca-Mn-O films on MgO, LAO and Si with comparison of RF sputtering and sol-gel methods. The composition of RF-sputtered grown LCMO had higher content of La than the target composition, while sol-gel method of LCMO films is believed to transfer same stoichiometric composition [8, 9].

The composition and thickness of PLD grown CMR manganite LSCMO films were investigated with the RBS system. The incident source atom and detecting angle of detector are accelerated 2.0 MeV He^{+2} and 15° , respectively. The best fit of the experimental RBS spectrum from SIMNRA 4.4b software, shown in Fig. 4-11, yields the ultimate composition of manganite: $\text{La}_{0.66}\text{Sr}_{0.17}\text{Ca}_{0.17}\text{MnO}_3$. It appears to be very close to the ratio of the laser pulsed shots $\text{La}_{0.67}\text{Sr}_{0.33}\text{MnO}_3 : \text{La}_{0.67}\text{Ca}_{0.33}\text{MnO}_3 = 27 : 31$ per cycle used in the PLD process.

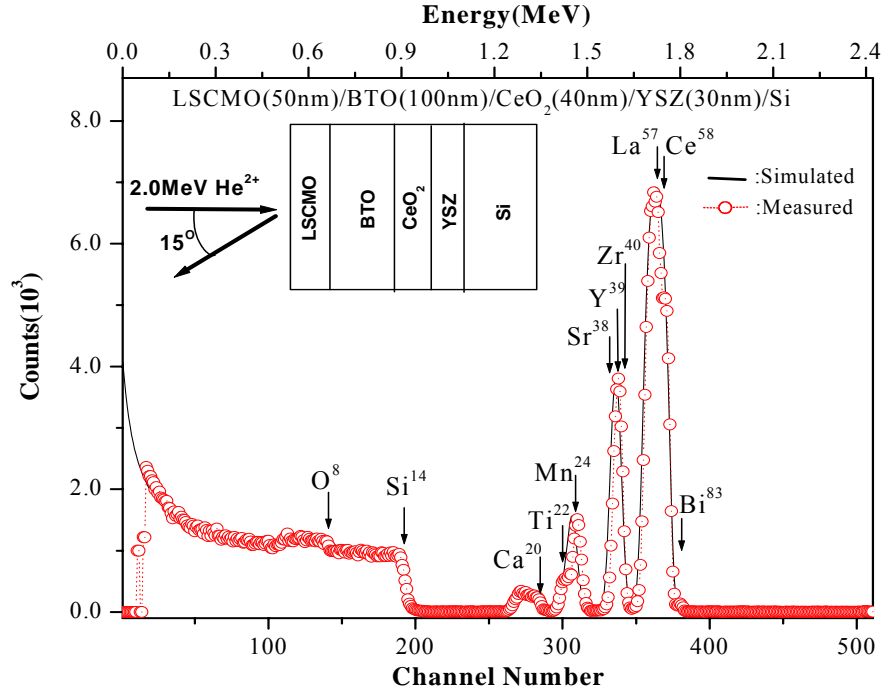


Figure 4-11. RBS spectrum of $\text{La}_{0.66}\text{Sr}_{0.17}\text{Ca}_{0.17}\text{MnO}_3/\text{Bi}_4\text{Ti}_3\text{O}_{12}/\text{CeO}_2/\text{YSZ}$ on Si.

The detailed data of composition and thickness measured by RBS is listed in Table VI. The measured thickness and composition of YSZ is slightly different compared to the target composition. It may be caused by interface reaction between the YSZ and SiO_2 layers including the silicon substrates.

Table VI. Simulation results of composition and thickness by RBS measurement.

	YSZ	CeO_2	$\text{Bi}_4\text{Ti}_3\text{O}_{12}$	$\text{La}_{0.67}(\text{Sr},\text{Ca})_{0.33}\text{MnO}_3$
Measured composition	$\text{Y}_{0.10}\text{Zr}_{0.20}\text{O}_{0.70}$ → $(\text{Y}_{0.34}\text{Zn}_{0.66})\text{O}_{2.33}$	$\text{Ce}_{0.33}\text{O}_{0.67}$ → CeO_2	$\text{Bi}_{0.2}\text{Ti}_{0.15}\text{O}_{0.65}$ → $\text{Bi}_4\text{Ti}_3\text{O}_{12}$	$\text{La}_{0.132}\text{Sr}_{0.034}\text{Ca}_{0.034}\text{Mn}_{0.199}\text{O}_{0.601}$ → $\text{La}_{0.66}(\text{Sr},\text{Ca})_{0.34}\text{MnO}_3$
Thickness (nm)	26.1	41.2	96.7	50.4

4.4 Transmission electron microscopy (TEM)

In order to investigate the crystallographic and interfacial relation of epitaxial layers and substrate, cross-sectional transmission electron microscopy (TEM) is widely used. Recently, the TEM technique is also able to be used on the atomic level to detect the elemental composition. The accelerated electron visualizes an image on a fluorescent screen by penetrating the surface. Therefore, high vacuum condition and very thin sample preparation are essential for TEM measurement.

For spin devices, Sun *et al* investigated thin CMR manganite junction of LSMO/STO/LSMO by TEM [10]. Using TEM map technique by defocusing, systematic studies of interface properties were performed to understand the main features that can affect the spin polarization property of STO/LSMO junction [11]. Recently, CMR LCMO nanowire on MgO substrates was successfully demonstrated by PLD technique including structural study of nanowire by XRD and TEM by Han *et al* [12].

The interface and crystal quality of heteroepitaxial LSCMO/BTO/CeO₂/YSZ on Si substrates was proved by high resolution TEM in Fig. 4-12. Cross-sectional TEM revealed the sharp and smooth interfaces of each layers. There are no traces of overgrowth and inter-diffusion. YSZ layers well ordered onto the amorphous 3 nm thick SiO₂. There are few misfit dislocations, marked 'a', on the CeO₂/YSZ layers due to lattice mismatch. Perfect crystalline matching of BTO layer on CeO₂ is shown due to similar *a* and *b* lattice parameters. Highly ordered LSCMO films on BTO layer are caused by completely accommodated mismatch strain through 45° rotation.

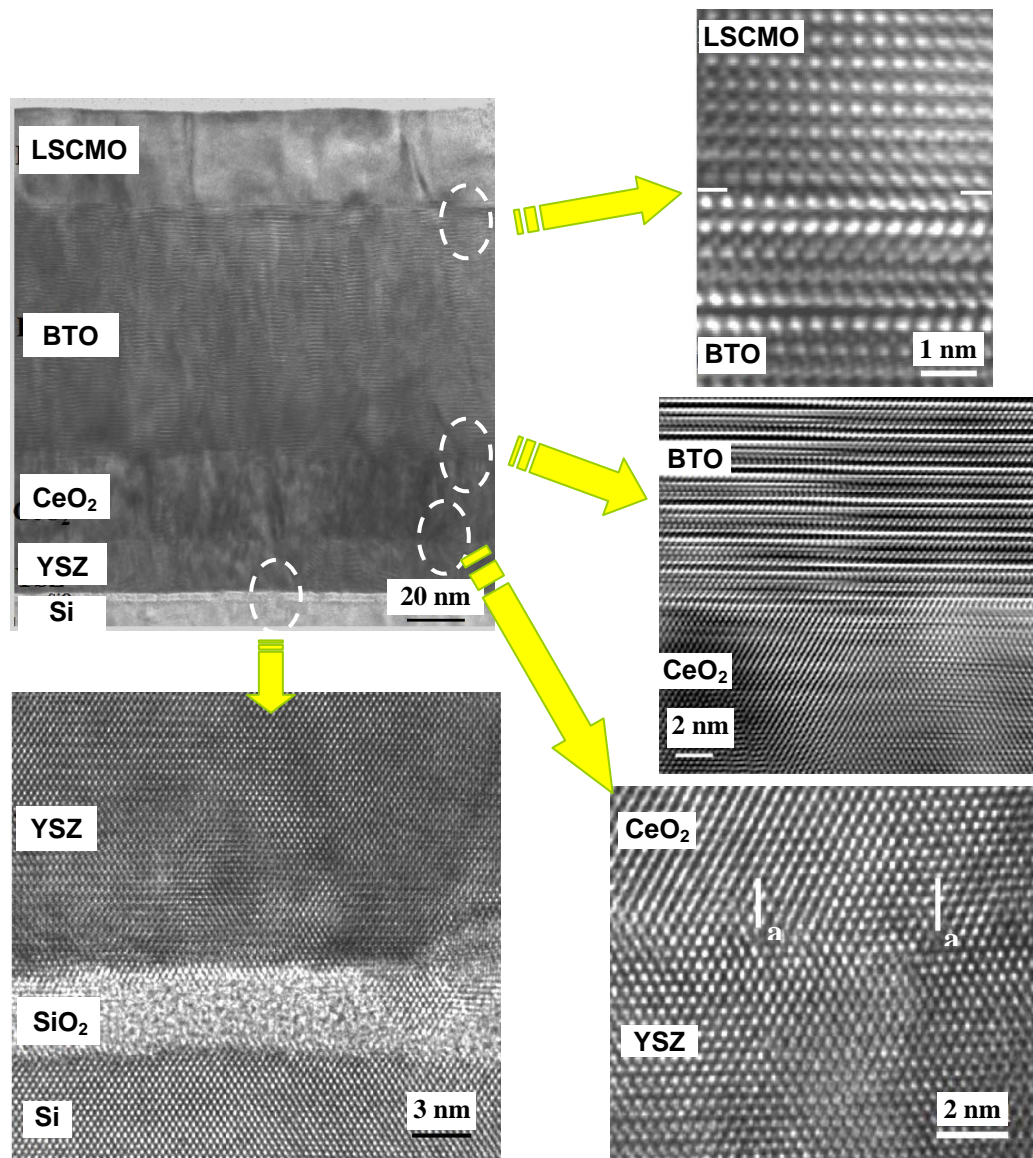


Figure 4-12. TEM images of La_{0.66}Sr_{0.17}Ca_{0.17}MnO₃/Bi₄Ti₃O₁₂/CeO₂/YSZ on Si(001). Mark 'a' represents misfit location on CeO₂/YSZ interface.

4.5 Atomic force microscopy (AFM)

AFM is one method of scanning probe microscopy (SPM) technique. A sharp tip located at the end of a cantilever is used to scan a sample surface within a very short distance (= tapping mode) or in contact mode. The interaction force between the sample surface and the sharp tip is monitored by detecting of a reflected laser beam focused onto the tip [13]. Small changes of the cantilever can be converted to a vertical movement of measurement data. Therefore, a 3-dimensional image of the scanned surface can be obtained by combining both vertical and horizontal movement. Fig. 4-13 shows the simple concept of AFM imaging.

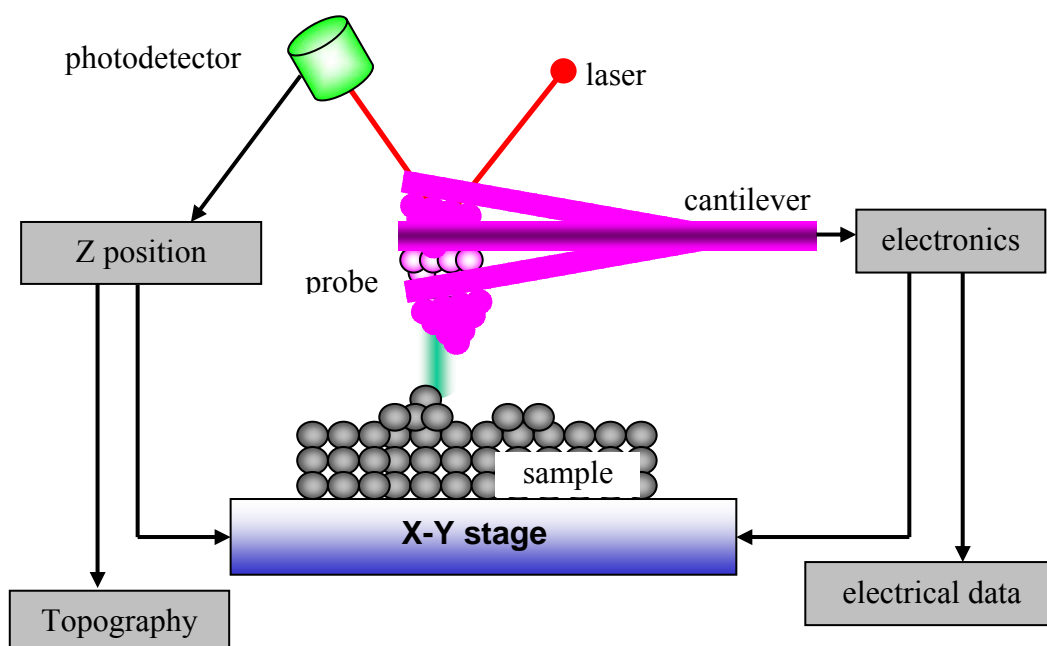


Fig. 4-13. Principle of atomic force microscopy measurement.

The roughness of films is strongly related to structural and electrical properties of manganite thin films due to the lattice mismatch [14]. Biswas *et al* studied the relation between morphology and electrical/magnetic properties of LCMO/LAO. Under biaxial compressive strain, the strain distribution is not uniform due to islands growth. The edges of islands are highly strained regions while the top are strain free areas. This non-uniform strain may be strongly related to a large MR and field-induced insulator-metal transition [15].

The surface morphologies of thin CMR $\text{La}_{0.75}\text{Sr}_{0.25}\text{MnO}_3/\text{BTO}/\text{CeO}_2/\text{YSZ}$ grown on $\text{Si}_{1-x}\text{Ge}_x/\text{Si}$, Si and $\text{Si}_{0.99}\text{C}_{0.01}/\text{Si}$ shown in Fig. 4-6(b) are illustrated in Fig. 4-14 by tapping mode AFM. The scan size and scan rate in these analyses were $2 \times 2 \mu\text{m}^2$ and 1 Hz, respectively. The root mean square (RMS) roughness of LSMO film of the samples containing $\text{Si}_{0.99}\text{C}_{0.01}$, Si, $\text{Si}_{0.95}\text{Ge}_{0.05}$, $\text{Si}_{0.9}\text{Ge}_{0.1}$ and $\text{Si}_{0.8}\text{Ge}_{0.2}$ was 1.51, 2.10, 1.61, 1.79 and 1.86 nm, respectively. This shows RMS roughness of $\text{Si}_{1-x}\text{Ge}_x$ layers is smoother than Si and it has an increasing tendency according to added content of Ge. Compared to Fig. 4-14(b) showed the layer quality of all $\text{Si}_{1-x}\text{Ge}_x$ layers became poor

after deposition of stack structure then it was expected that these defected layers should have rough interface and also cause the whole structure will have rough surface. Therefore, this surface morphology may be traced to the presence of strain or diffusion of defects. In these structures, the generated defects during the growth of the buffer layers can be diffused into the $\text{Si}_{1-x}\text{Ge}_x$ layers and they cause mosaicity or relaxation. In this case, the Ge amount and the layer thickness determine the amount of relaxation.

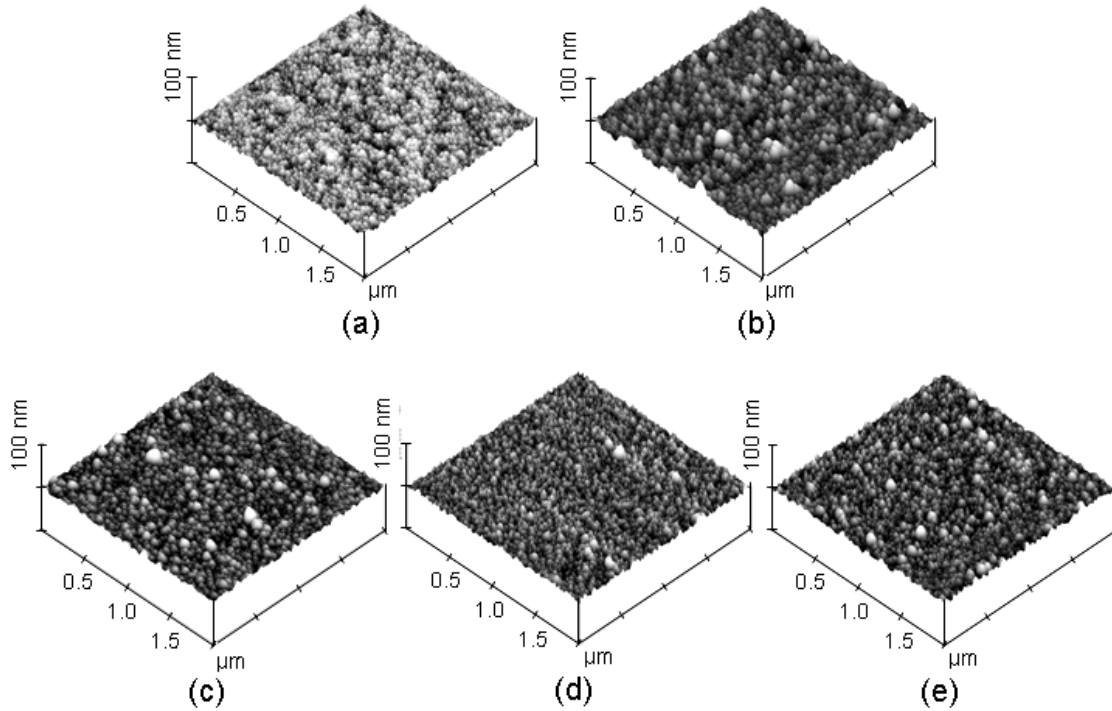


Figure 4-14. AFM images of PLD-deposited $\text{La}_{0.75}\text{Sr}_{0.25}\text{MnO}_3$ on $\text{Bi}_4\text{Ti}_3\text{O}_{12}/\text{CeO}_2/\text{YSZ}$ buffered on (a) $\text{Si}_{0.99}\text{C}_{0.01}/\text{Si}$ (b) Si (c) $\text{Si}_{0.95}\text{Ge}_{0.05}/\text{Si}$ (d) $\text{Si}_{0.9}\text{Ge}_{0.1}/\text{Si}$ (e) $\text{Si}_{0.8}\text{Ge}_{0.2}/\text{Si}$.

4.6 Scanning spreading resistance microscopy (SSRM)

Scanning spreading resistance microscopy (SSRM, Nanoscope 3100 with Application Module System) enables to measure electrical conductivity or resistivity of sample. Using an electrically conductive probe in contact mode, the electrical resistance was calculated by measuring voltage, which has an increasing tendency with decreasing resistance.

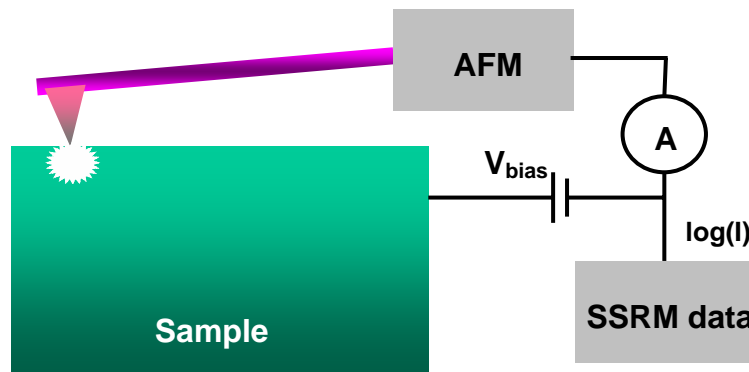


Figure 4-15. Set-up of scanning spreading resistance microscopy.

The electrical information and image data can be obtained in contact mode by measurement of the voltage between conductive SSRM tip and sample with selectable applied bias [16, 17]. Schematic of SSRM measurement is shown in Fig. 4-15. The resistivity of sample, ρ_{sample} can be expressed in case of perfect ohmic contact [17].

$$R_{sp} = \frac{\rho_{sample}}{4 \cdot r_{tip}} \quad (4-3)$$

where R_{sp} and r_{tip} are for the measured spreading resistance and SSRM tip radius.

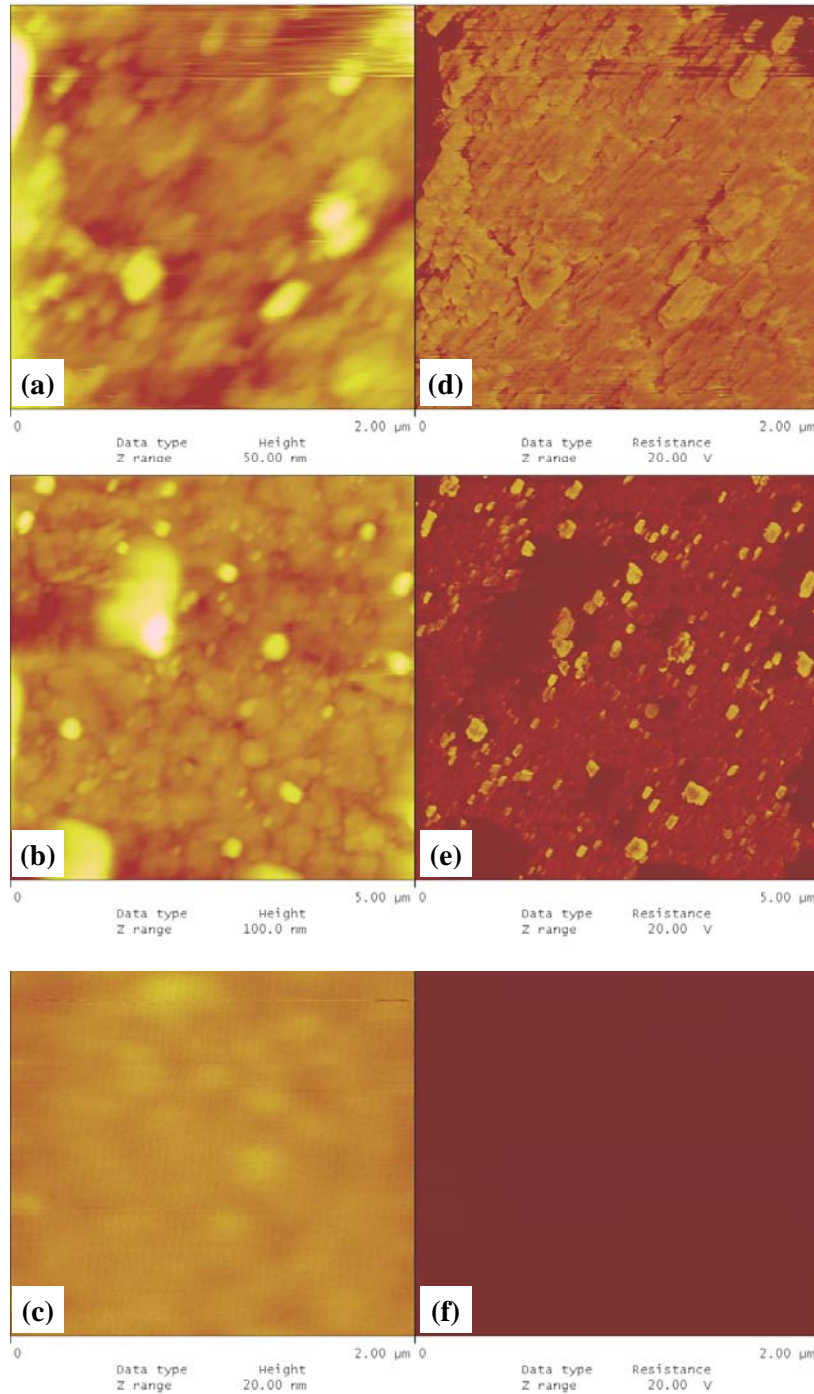


Figure 4-16. Topography of (a) as grown $\text{La}_{0.75}\text{Sr}_{0.25}\text{MnO}_3/\text{Bi}_4\text{Ti}_3\text{O}_{12}/\text{CeO}_2/\text{YSZ}$ on Si (b) after 1 min Ar ion beam etching (IBE) (c) after 3 min Ar IBE . The corresponding SSRM resistances of (d) as grown (e) 1 min etching and (f) 3 min etching.

Until now, most of SSRM related reports are for 2- or 3-dimensional carrier distributions of III-V materials [18, 19], doping profiles and actual nanosize-channel dimension of field effect transistor (FET) [20, 21] however there is no publications of SSRM data for CMR manganite thin films. Furthermore, SSRM technique is also very useful to investigate electrical properties of *micro*-scale free standing area where conventional electrical measurement technique cannot be applied.

To investigate the electrical property of CMR manganite films by dry etching process, SSRM measurements were executed on $\text{La}_{0.75}\text{Sr}_{0.25}\text{MnO}_3/\text{BTO}/\text{CeO}_2/\text{YSZ}/\text{Si}$,

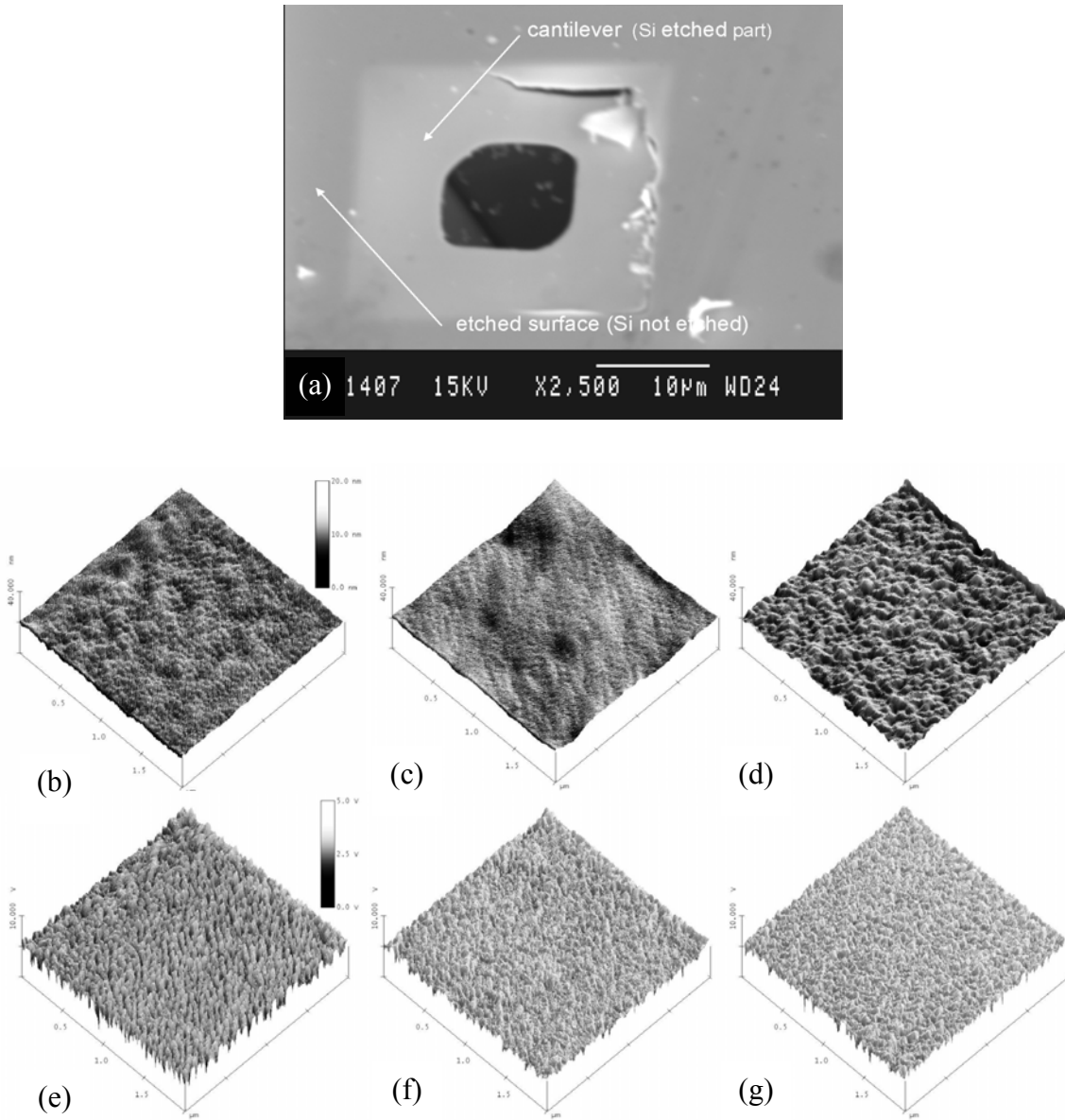


Figure 4-17. Results of KOH wet etching experiment of LSCMO/BTO/CeO₂/YSZ on Si. (a) SEM image of LSCMO etched surface after 3 hours. (b) AFM topographic images of as grown (c) LSCMO etched surface (d) free standing LSCMO cantilever part in etched sample. The corresponding SSRM data of (e) as grown (f) LSCMO surface and (g) LSCMO cantilever.

after 1 min and after 3 min of Ar ion beam etching (IBE), respectively. The scanned topographies and SSRM resistances of as grown and etched samples are shown in Fig. 4-16. In case of as-grown sample, SSRM image is brightest due to the lowest resistivity shown in Fig. 4-16(a). However, as elapsed time of Ar IBE process, the SSRM images become dark color that represents insulating property of films.

For KOH wet etching, the surface morphology and electrical properties of free standing LSCMO films were also investigated by SSRM technique. The etch rate for LSCMO films in the KOH of 23% w.t and 80 °C condition was lower than 0.2 nm/min. Free standing area in etched LSCMO sample is slightly deflected in Fig. 4-17(a) due to wet etching process effects and stress release. The initial applied bias to the surface was 0 V (= equivalent to 10^6 Ohm with internal reference resistor) and increased until optimal SSRM image. The scan area and scan rate were $2 \times 2 \mu\text{m}^2$ and 1 Hz. The surface morphology and resistance results are shown in Fig. 4-17(b)-(f). The root mean square (RMS) and peak to valley ($R_p - R_v$) roughness of topography and SSEM data were summarized in Table VII.

After 3 hours KOH etching, RMS roughness of etched LSCMO films is larger than of as-grown. Moreover, $R_p - R_v$ value has an increasing tendency. These results indicate that KOH makes LSCMO films rougher during etching process. For electrical measurement, SSRM RMS roughness of etched cantilever LSCMO area were 0.34 and 1.8 V lower than of as-grown sample shown in Fig. 4-17. These results indicate that there are different etch rates for between fully stoichiometric area (slow etch rate) and partially less homogenous area (fast etch rate) in LSCMO films. Therefore, increasing of KOH etching time, the surface roughness of the LSCMO films has an increasing tendency with decreasing resistance roughness.

Table VII. Summarized RMS and electrical SSRM roughness of as-grown and KOH-etched $\text{La}_{0.67}(\text{Sr,Ca})_{0.33}\text{MnO}_3$ on oxide-buffered Si substrates.

		$\text{La}_{0.67}(\text{Sr,Ca})_{0.33}\text{MnO}_3$		
measurement		as-grown	etched surface	etched cantilever
RMS roughness (nm)		0.5	1.1	0.7
Topography	$R_p - R_v$ (nm)	3.6	6.4	4.2
RMS roughness (V)		0.68	0.35	0.34
SSRM	$R_p - R_v$ (V)	3.4	1.6	1.8

The estimated resistivity of as grown and 3 hours etched LSCMO films by KOH are about 76 and 189 $\text{m}\Omega\cdot\text{cm}$ using Eq. 4-3, where the tip radius is about 10 nm. Higher resistivity value than electrical results (see Chap. 4-9) may stem from tip-surface contact resistance, spreading resistance of films, back contact resistance and various instruments terms [18]. Finally, the etched free standing membrane shows a little higher resistivity than the etched surface due to deflection related to different strain effects.

4.7 Magnetic force microscopy (MFM)

Magnetic force microscopy (MFM) is a special measurement technique to characterize magnetic properties of sample with high spatial resolution.

The principle of the MFM measurement is that a tapping cantilever with special magnetized tip scans over the sample surface in order to obtain topography information and magnetize the sample surface at the same time. Then, the tip is slightly lifted, called *LiftMode*, just above the sample surface and re-scans the surface to monitor the magnetic influence between tip and magnetized surface. This magnetic influence can react with the free resonating frequency of the cantilever (f_x) by altering the frequency $f_{x\pm\delta}$. Therefore, bigger alternation of frequency represents stronger magnetic influenced area. Fig. 4-18 shows the concept of MFM LiftMode technique [22].

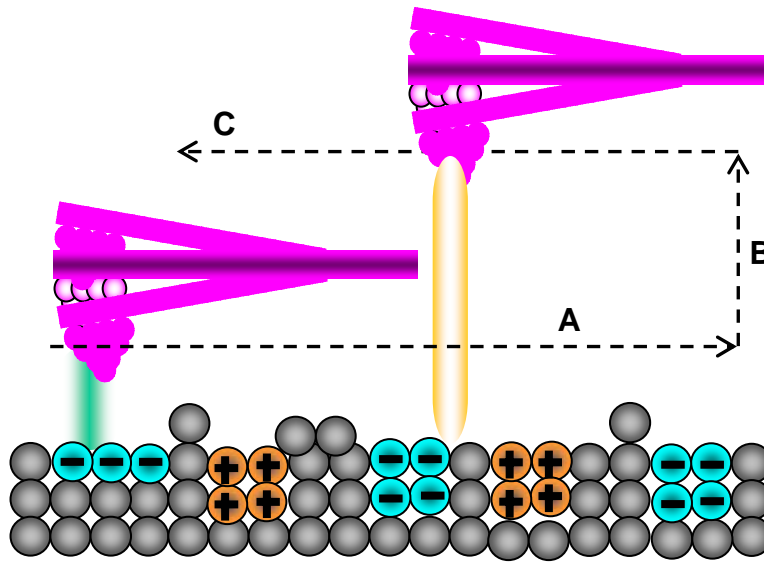


Figure 4-18. Principle of magnetic force microscopy imaging. The cantilever moves along the surface to obtain topography and magnetize surface (A). Then, cantilever is slightly lifted (B) over surface and re-profiles topography to get the magnetic influence (C).

Zhang *et al* studied the temperature dependant magnetic properties of $\text{La}_{0.33}\text{Pr}_{0.34}\text{Ca}_{0.33}\text{MnO}_3$ (LPCMO) using MFM technique [23]. With decreasing temperature (Fig. 4-19 A), isolated ferromagnetic (FM) domain occurs, and merge each other near the transition temperature, resulting in a rapidly drop of resistivity (Fig. 4-19 B), whereas the FM domain size seems not to be changed with elevated temperature (Fig. 4-19 C). As early discussed in Chap. 2-4, this magnetic domain can be changed by the strain induced from the lattice mismatch.

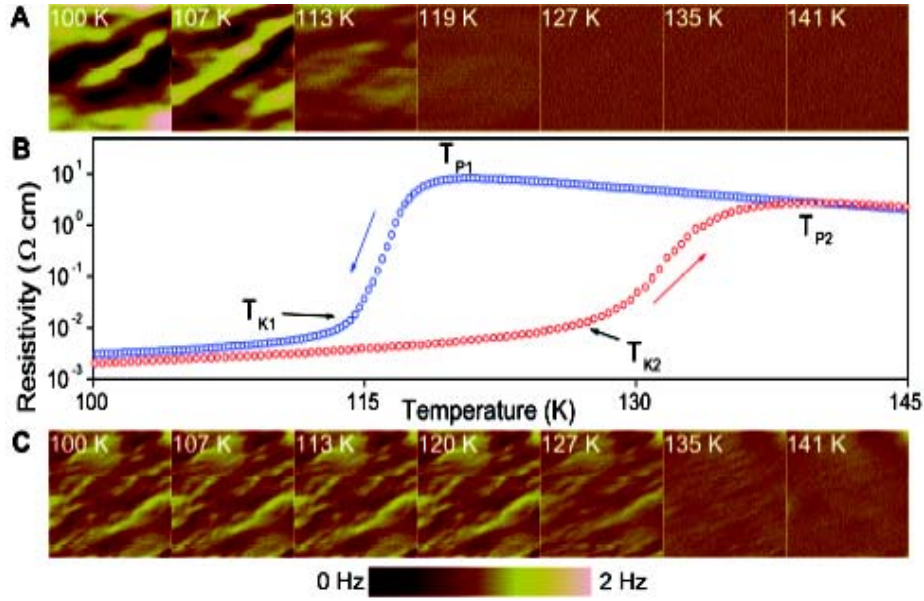


Figure 4-19. Sequential temperature-dependant MFM images of LPCMO films in cooling (c) in warming (b) correspond resistivity curve cycle (after [23]).

Induced tensile or compressive strain from substrates shows different magnetic domain shapes. Desfeux *et al* observed *bubble magnetic* pattern with out-of-plane magnetization for LSMO/LAO (compressive strain), while *feather-like* pattern appeared with in-plane magnetization for LSMO/STO (tensile) and LSMO/NGO (compressive). Moreover, Dho *et al* demonstrated the change of magnetic domain of LSMO films by applying magnetic field [24].

The MFM image of CMR thin LSCMO/BTO/CeO₂/YSZ on Si is shown in Fig. 4-20. This image looks like '*maze-like domain*' similar to LSMO/STO in chap. 2.4. Therefore, this result is accordance with tensile strain on LSCMO films from silicon substrates.

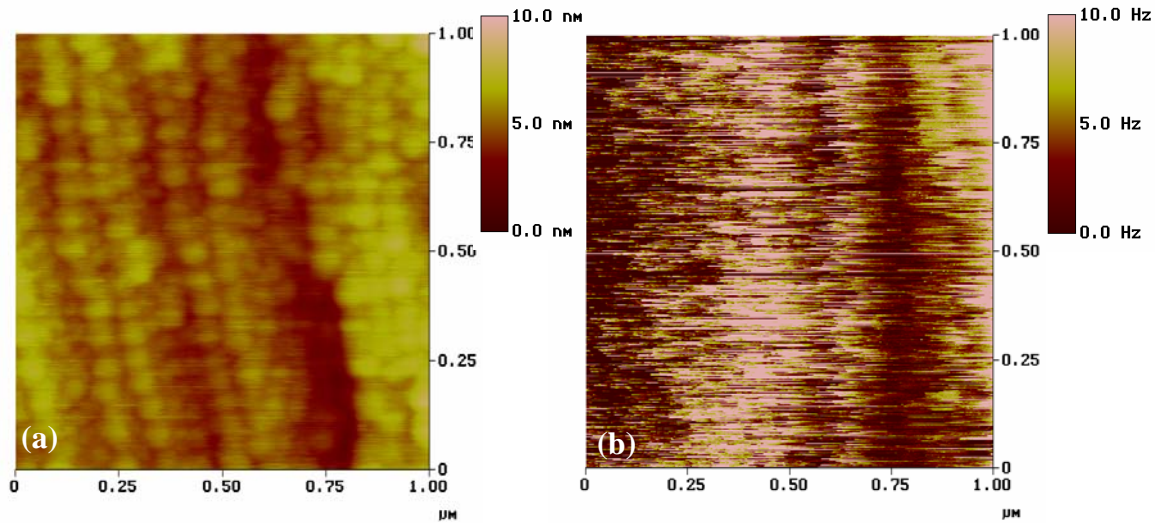


Figure 4-20. The images of (a) topography on thin LSCMO/BTO/CeO₂/YSZ/Si (b) MFM by magnetic tip using LiftMode.

4.8 Noise measurement

Noise measurement of CMR manganite films is one of the important characteristics for bolometric application. The minimum noise level, called *Johnson noise*, does not depend on other noise sources. Therefore, noise measurement includes three kinds of noise: *Johnson noise* (thermal noise), measurement system noise and excessive (additional) noise.

Rajeswari *et al* investigated $1/f$ electrical excessive noise in $\text{La}_{0.67}\text{Ca}_{0.33}\text{MnO}_3$ (LCMO) and $\text{Pr}_{0.67}\text{Sr}_{0.33}\text{MnO}_3$. The noise level of manganites is 5 ~ 6 orders larger than for YBCO. Noise source strength, called as Hooge's parameter, of CMR manganites are also 5 orders larger than for GMR metallic layers [25]. In addition, they revealed that oxygen annealing in LCMO and $\text{Nd}_{0.67}\text{Sr}_{0.33}\text{MnO}_3$ decreased the magnitude of $1/f$ noise and increased the TCR values [26]. Reutler *et al* studied the relation of strain and $1/f$ noise of $\text{La}_{2/3}\text{Ca}_{1/3}\text{MnO}_3$ (LCMO) films on different substrates. The noise level in strain free LCMO films grown on NdGaO_3 (NGO) was comparable to conventional metals, while large lattice mismatched LCMO on STO is several orders larger [27]. Lissauskas *et al* investigated the noise characterization of $\text{La}_{0.7}(\text{Pb}_{0.63}\text{Sr}_{0.37})_{0.3}\text{MnO}_3$ (LPSMO) for bolometric application with $7.4\% \cdot \text{K}^{-1}$ higher TCR values [28]. Recently Palanisami *et al* showed a noise study in $\text{La}_{0.7}\text{Ca}_{0.3}\text{MnO}_3$ films on NGO. For $T < T_c$, the peak of excessive noise was shown to be near and below T_c whereas $1/f$ noise drops to a very low level in case of $T > T_c$. This result was interpreted by strain effect and effect of fluctuator size [29].

Noise, in general, can be expressed by the amount of incident power on sensing area, which can create corresponding signal equal to noise power. Lissauskas *et al* intensively studied the electrical fluctuation (= noise) in manganite and ferroelectric films [30].

To characterize noise in CMR manganite films, empirical Hooge's relation is expressed by

$$\frac{S_R(f)}{R^2} = \frac{\alpha_{\text{Hooge}}}{n_c \cdot f^\alpha} \quad (4-4)$$

where $S_R(f)$, R , α_{Hooge} , n_c are spectral density of resistance fluctuations at frequency f , resistance, Hooge's parameter of material and the number of charge carriers in homogeneous material, respectively. Hooge's parameter in manganite films, due to uncertainty in the number of charge carriers, can be obtained by

$$\frac{\alpha_{\text{Hooge}}}{n} = \frac{f \cdot \text{Vol} \cdot S_R(f)}{R^2} \quad (4-5)$$

where, Vol is the sensing material volume. The normalized α_{Hooge}/n varies according to the sensing materials.

For temperature and magnetic applications of CMR manganites, the sensitivity of materials can be characterized with noise equivalent difference. The noise equivalent

temperature difference (NETD) without optical system and readout can be given by [28, 30]

$$\blacksquare \quad NETD \approx \frac{\sqrt{I_{bias}^2 S_R(f)}}{I_{bias} \frac{dR}{dT}} = \frac{\sqrt{S_R(f)}}{\frac{dR}{dT}} = \frac{\sqrt{S_v(f) + 4kTR(T)}}{I \cdot dR/dT} \quad (4-6)$$

where I_{bias} , R , $S_R(f)$ and $S_v(f)$ are the biased current, resistance of CMR manganite films, spectral density of resistance and voltage fluctuations at frequency f , respectively.

■ Noise equivalent magnetic field difference (NEMFD, Oe/ $\sqrt{\text{Hz}}$)

$$NEMFD \approx \frac{\sqrt{S_R(f)}}{\frac{dR}{dH}} = \frac{\sqrt{S_v(f) + 4kTR(T)}}{I \cdot dR/dH} \quad (4-7)$$

For precise noise characterization, the thermal noise and system noise must be distinguished from measurement data. The schematic of the noise measurement system at low frequency is shown in Fig. 4-21. More details for detecting noise power of CMR manganite films, preamplifier noise and thermal noise are presented in reference [30].

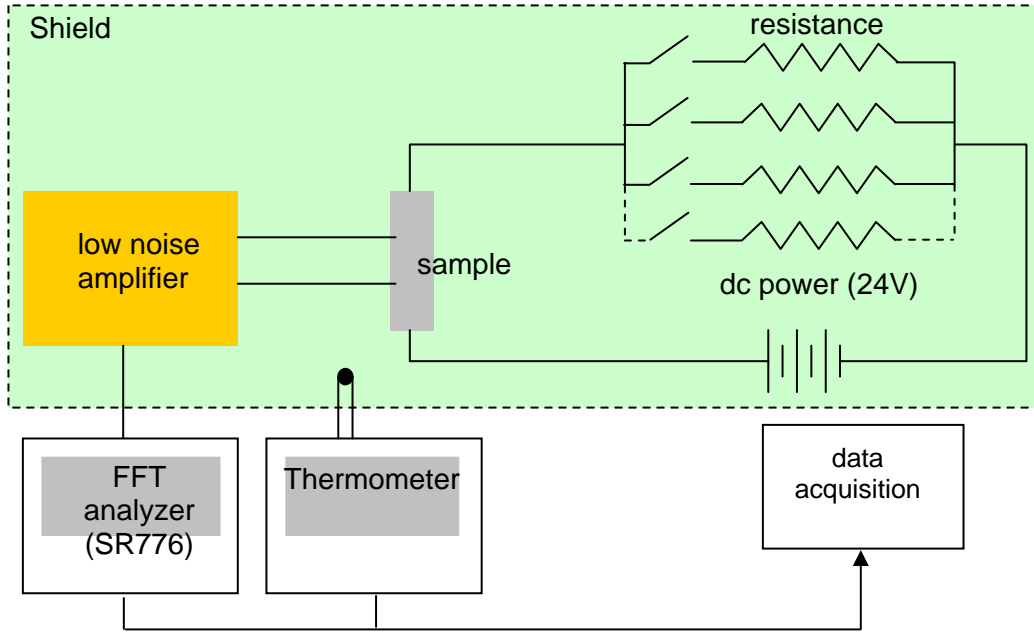


Figure 4-21. Noise measurement system used in this study.

The level of intrinsic electrical noise is another factor, which determines the performance of resistive temperature/magnetic field sensor. As it is shown in Fig. 4-22, there are two components in the noise spectra: *Johnson noise* $S_v = 4kTR(T)$ and excess noise parameterized by Hooge's relation from Eq. 4-4:

$$S_v(f) = \frac{\gamma}{n} \frac{I^2 \cdot R^2}{V \cdot f} \quad (4-8)$$

Here S_v is the voltage fluctuations spectral density, γ is the material Hooge's parameter, n is the charge carrier density, I is the bias current fed into the sample, R is the sample resistance, V is the sample volume and f is the frequency. S_v was measured using a nearly placed preamplifier using a field effect transistor with a short junction noise of 2.6 nV/ $\sqrt{\text{Hz}}$.

Spectral density, $S_v(f)$ at various bias currents j (or I in Eq. 4-8) are shown in Fig. 4-22. They are fitted to $S_v \propto f^{-1.2}$ and $S_v \propto j^{1.7}$, respectively. At 294K and 30 Hz, the normalized noise power is found to be $\gamma/n = 1.6 \times 10^{-20} \text{ cm}^3$. This value is five times higher than in LPSMO/LaAlO₃ IR bolometer exhibiting a noise equivalent temperature difference (NETD) as low as 120 nK/ $\sqrt{\text{Hz}}$ [28].

The NETD and NEMFD, the main figures of merit for the sensing materials in Eq. 4-6 and 4-7 show the minimal fluctuations of temperature/magnetic field strength resolvable on the electric noise background. For 2 mm \times 2 mm \times 50 nm LSCMO CMR films on silicon substrates, NETD = 1.18 $\mu\text{K}/\sqrt{\text{Hz}}$ and NEMFD = 260 $\mu\text{Oe}/\sqrt{\text{Hz}}$ are obtained at 30 Hz and 1 kHz in room temperature. Inverse values of NETD and NEMFD define the signal to noise ratio (SNR). Assuming a thermal conductance $G = 10^{-6} \text{ W/K}$ and relaxation $\tau = 1 \text{ msec}$ for typical microbolometer arrays [28], the 50 $\mu\text{m} \times 50\mu\text{m} \times 0.5\mu\text{m}$ LSCMO microbolometer with the absorptivity $\eta = 0.7$ will get the responsivity $\mathfrak{R} = 1.4 \times 10^3 \text{ V/W}$, noise equivalent power NEP = $1.7 \times 10^{-11} \text{ W}/\sqrt{\text{Hz}}$, and detectivity $D = 2.9 \times 10^8 \text{ cm} \cdot \text{W}/\sqrt{\text{Hz}}$.

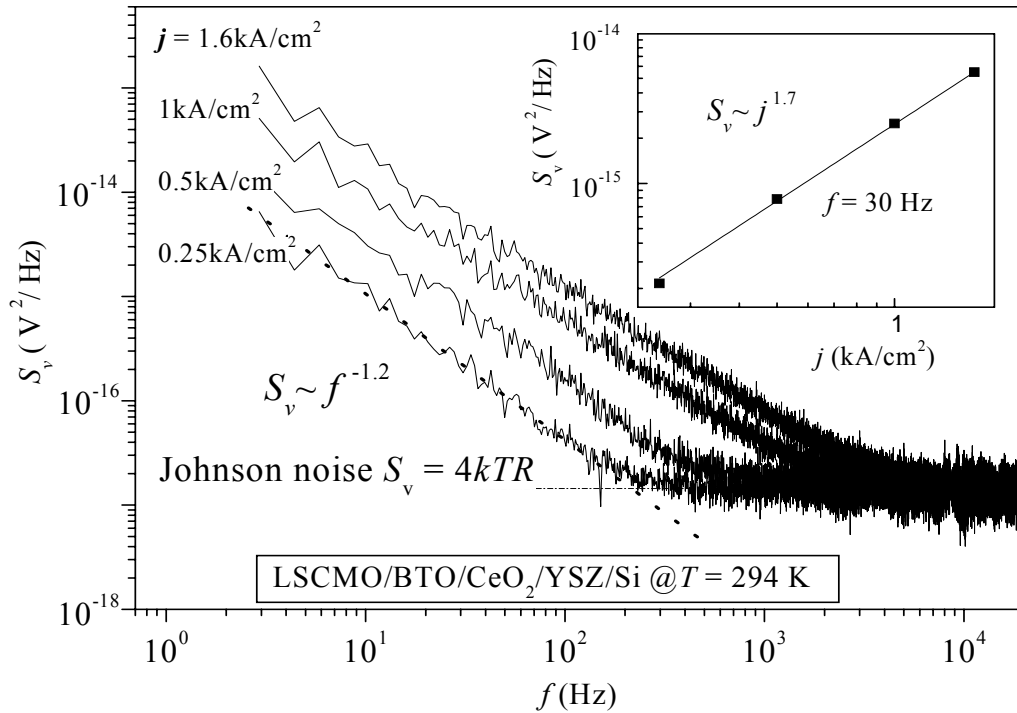


Figure 4-22. Noise measurement of LSCMO CMR films on Si. Insert represents voltage fluctuation spectral density S_v vs. current density at 30 Hz.

4.9 Electrical/Magnetic transport measurements

Electrical resistivity of CMR manganite film was obtained by the four-point technique with a temperature-controlled holder. Fig. 4-23 shows normalized resistivity of $\text{La}_{0.67}\text{Ca}_{0.33}\text{MnO}_3$ (LCMO), $\text{La}_{0.67}(\text{Sr},\text{Ca})_{0.67}\text{MnO}_3$ (LSCMO) and $\text{La}_{0.67}\text{Sr}_{0.33}\text{MnO}_3$ (LSMO) films with the same sequence of BTO/CeO₂/YSZ buffers on silicon substrates. All three films demonstrate abrupt increase of resistivity at ferro-to-paramagnetic phase transition temperature T_c . The absolute values of resistivity maximum, ρ_{\max} and T_c , for LCMO and LSMO films are in a good agreement with those of the deposited onto single crystal oxides substrates. The peak value of the temperature coefficient of resistivity has an increasing tendency with T_c decreasing. For optimized composition between LSMO and LCMO, LSCMO shows that TCR as high as $4.4\% \text{K}^{-1}$ is reached at 294 K.

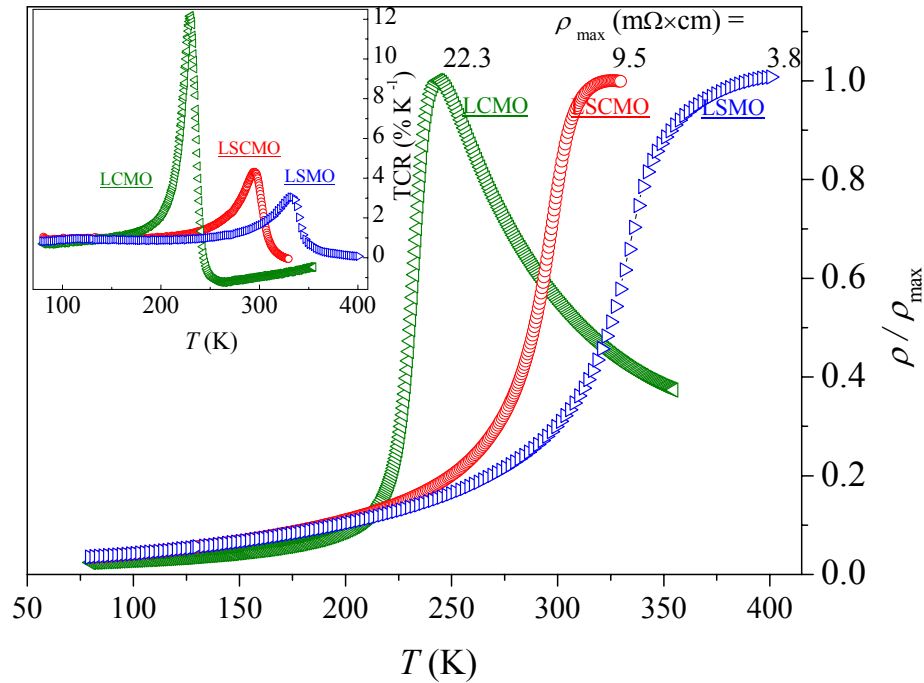


Figure 4-23. Temperature dependant resistivity of LSMO, LSCMO and LCMO on oxide buffered Si. Insert represents corresponding TCR values.

The magnetoresistance (MR), $\Delta\rho/\rho = [1 - \rho(H)/\rho(0)] \times 100\%$, of LSCMO film on Si, demonstrates remarkable linearity with $\Delta\rho/\rho = 2.9\% \text{kOe}^{-1}$ except negligible hysteresis with the coercive field as low as 4 Oe. Fig. 4-24 shows temperature dependent resistivity, TCR of $\text{La}_{0.67}(\text{Sr},\text{Ca})_{0.33}\text{MnO}_3$ on Si wafer. Inset of Fig. 4-24 represents magnetoresistance of LSCMO films.

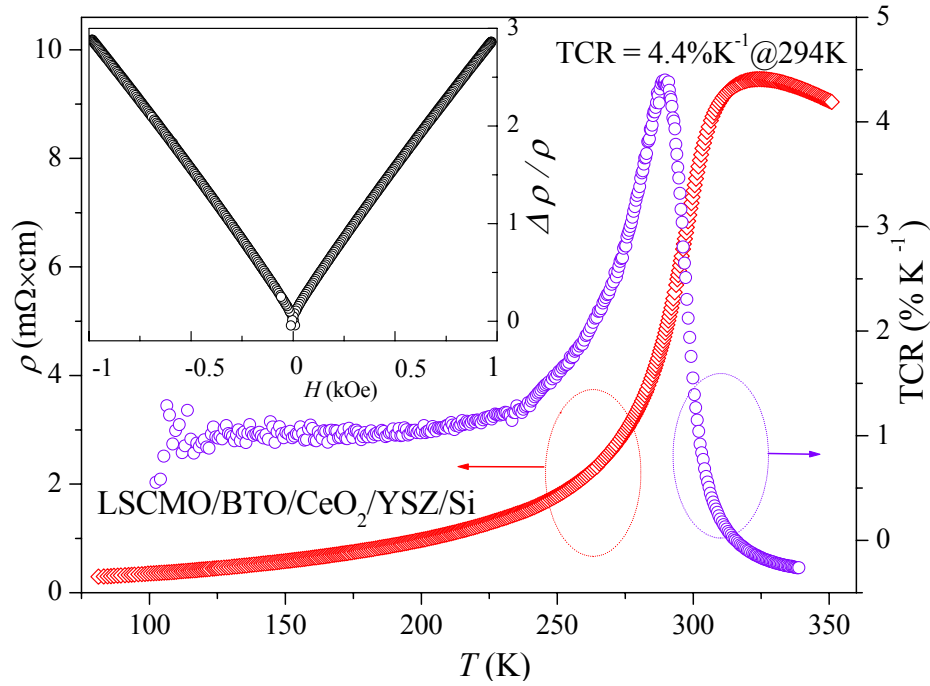


Figure 4-24. Temperature dependence of TCR and resistivity of $\text{La}_{0.67}(\text{Sr,Ca})_{0.33}\text{MnO}_3$ film on Si wafer. The insert shows magnetoresistance.

Fig. 4-25 shows the transport characterization of heteroepitaxial LCMO and LSMO thin manganite films on MgO buffered GaAs substrates.

Both LCMO and LCMO films exhibit metal to insulator phase transition. The maximum TCR and MR for LCMO films in Fig. 4-25(a) are 9.0 %K⁻¹ at 223 K and -7.95 %kOe⁻¹ at 209 K, respectively. However without 590 °C treatment, LCMO film quality became worse resulting in a low TCR value. For the LSMO films in Fig. 4-25(b), maximum 2 %K⁻¹ TCR at 327 K and -1.47 %kOe⁻¹ MR and 295 K were obtained, respectively. The insets present MR by applying magnetic field for LCMO and LSMO films in Fig. 4-25(a) and (b), respectively.

The hysteresis of MR at weak magnetic field yields coercive field $H_c = 67$ and 32.1 Oe for LCMO and LSMO films, respectively. This hysteresis indicates dislocations which release the strain. Therefore higher coercive field means higher lattice mismatch between CMR films and substrates.

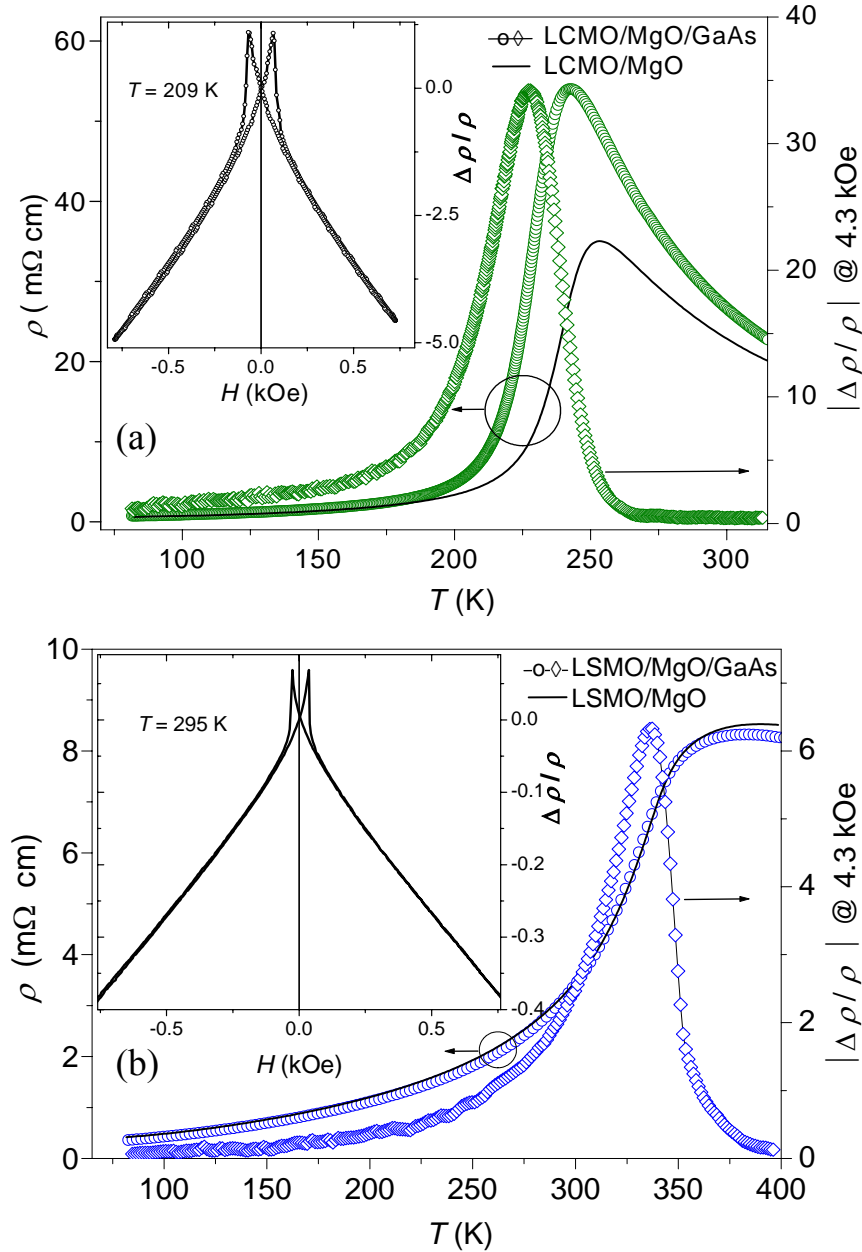


Figure 4-25. Temperature dependence of the resistivity and the magnetoresistance of (a) $\text{La}_{0.67}\text{Ca}_{0.33}\text{MnO}_3$ (LCMO) on GaAs. The insert is magnetoresistance ($\text{MR} = \Delta\rho/\rho$) of LCMO/MgO/GaAs. (b) $\text{La}_{0.67}\text{Sr}_{0.33}\text{MnO}_3$ (LSMO) on GaAs. The insert shows MR of LSMO/MgO/GaAs.

Strain induced by lattice mismatch can affect the transport properties of CMR manganites. Fig. 4-26 shows the electrical results of $\text{La}_{0.75}\text{Sr}_{0.25}\text{MnO}_3$ films grown on various strained $\text{Si}_{1-x}\text{Ge}_x/\text{Si}$ and $\text{Si}_{1-y}\text{C}_y/\text{Si}$. The inset presents the corresponding temperature dependant resistivity of LSMO films on oxide buffered $\text{Si}_{0.8}\text{Ge}_{0.2}/\text{Si}$, $\text{Si}_{0.9}\text{Ge}_{0.1}/\text{Si}$, $\text{Si}_{0.95}\text{Ge}_{0.05}/\text{Si}$, and Si substrates.

The $\text{Si}_{0.99}\text{C}_{0.01}$ layer shows a significant deviation of the resistivity values, however, all normalized resistivity curves of LSMO films on $\text{Si}_{1-x}\text{Ge}_x/\text{Si}$ except $\text{Si}_{0.8}\text{Ge}_{0.2}/\text{Si}$ shows very close traces of Si sample. Table VIII shows the relation between Ge contents and electrical/structural quality of LSMO films.

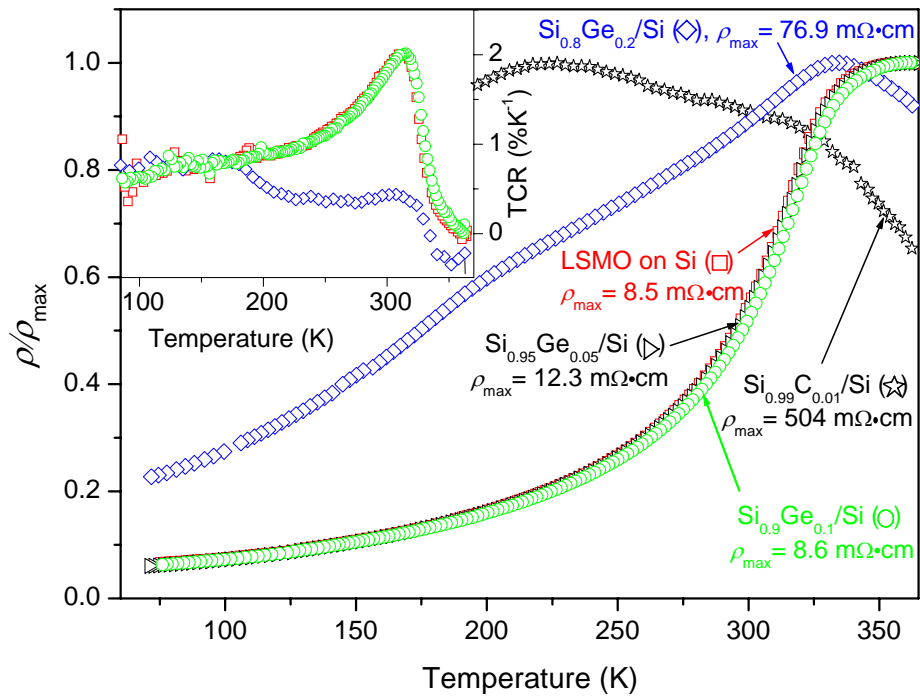


Figure 4-26. Temperature dependence of normalized resistivity $\rho(T)$ of $\text{La}_{0.75}\text{Sr}_{0.25}\text{MnO}_3$ films on various strained substrates. Inset is the corresponding TCR values of LSMO on $\text{Si}_{0.9}\text{Ge}_{0.2}/\text{Si}$, $\text{Si}_{0.9}\text{Ge}_{0.1}/\text{Si}$, and Si , respectively.

Table VIII. TCR and FWHM of $\text{La}_{0.75}\text{Sr}_{0.25}\text{MnO}_3$ films on various substrates.

	$\text{Si}_{0.8}\text{Ge}_{0.2}/\text{Si}$	$\text{Si}_{0.9}\text{Ge}_{0.1}/\text{Si}$	$\text{Si}_{0.95}\text{Ge}_{0.05}/\text{Si}$	Si	$\text{Si}_{0.99}\text{C}_{0.01}/\text{Si}$
$\text{Si}_{1-x}\text{Ge}_x$ and $\text{Si}_{1-y}\text{C}_y$ layers thickness (nm)	120	103	105		120
$\text{Si}_{1-x}\text{Ge}_x$ and $\text{Si}_{1-y}\text{C}_y$ lattice parameters a (Å)	5.472	5.451	5.441	5.431	5.395
$\text{Si}_{1-x}\text{Ge}_x$ and $\text{Si}_{1-y}\text{C}_y$ FWHM of (004) (deg)	1.10	0.81	0.95	0.85	1.10
LSMO film RMS roughness (nm)	1.86	1.79	1.61	2.10	1.51
ρ_{\max} ($\text{m}\Omega\cdot\text{cm}$)	76.9 @ 334 K	8.6 @ 362 K	12.3 @ 362 K	8.5 @ 360 K	504 @ 229 K
TCR_{\max} ($\%\cdot\text{K}^{-1}$)	0.09 @ 156 K	2.03 @ 314 K	2.02 @ 310 K	2.01 @ 311 K	0.04 @ 154 K

References

- [1] B. D. Cullity, S. R. Stock, *Elements of X-Ray Diffraction*, 3rd ed., Prentice Hall, New Jersey, (2001).
- [2] J. P. Dismukes, L. Ekstrom, E. F. Steigmeier, I. Kudman, and D. S. Beers, *J. Appl. Phys.* **35**(10), 2899 (1964).
- [3] Erdal Suvar, *SiGeC Heterojunction Bipolar Transistor*, Doctoral Thesis, Royal Institute of Technology, (2003).
- [4] R. People and J. C. Bean, *Appl. Phys. Lett.* **47**(3), 322 (1985); J. W. Matthews, A. E. Blakeslee, *J. Crystal Growth* **27**, 118 (1974).
- [5] E. Koppensteiner, G. Bauer, H. Kibbel, E. Kasper, *J. Appl. Phys.* **76**(6), 3489 (1994).
- [6] M. Kanai, H. Tanaka, T. Kawai, *Phys. Rev. B* **70**, 125109 (2004).
- [7] F. Giesen, B. Damaschke, V. Moshnyaga, K. Samwer, G. A. Müller, *Phys. Rev. B* **69**, 014421 (2004).
- [8] S.-I. Park, J.-H. Son, S.-S. Cho, C.-S. Kim, *IEEE Tran. Magn.* **36**(5), 2933 (2000).
- [9] S.-I. Park, K.-H. Jeong, Y.-S. Cho, C.-S. Kim, *J. Magn. Magn. Mater.* **242-245**, 692 (2002).
- [10] J. Z. Sun, *Phi. Trans. R. Soc. Lond. A* **356**, 1693(1998); Yu Lu, X. W. Li, G. Q. Gong, G. Xiao, A. Gupta, P. Lecoeur, J. Z. Sun, Y. Y. Wang, V. P. Dravid, *Phys. Rev. B* **54**(12), R8357 (1996).
- [11] F. Pailloux, D. Imhoff, T. Sikora, A. Barthélémy, J.-L. Maurice, J.-P. Contour, C. Colliex, A. Fert, *Phys. Rev. B* **66**, 014417 (2002).
- [12] S. Han, C. Li, Z. Liu, B. Lei, D. Zhang, W. Jin, X. Liu, T. Tang, C. Zhou, *Nano Letters* **4**(7), 1241 (2004).
- [13] Oliver Douheret, *High Resolution Electrical Characterization of III-V Materials and Devices*, Doctoral Thesis, Royal Institute of Technology, (2004).
- [14] M. Paranjape, A. K. Raychaudhuri, N. D. Mathur, M. G. Blamire, *Phys. Rev. B* **67**, 214415 (2003).
- [15] A. Biswas, M. Rajeswari, R. C. Srivastava, Y. H. Li, T. Venkatesan, R. L. Greene, A. J. Millis, *Phys. Rev. B* **61**, 9665 (2000).
- [16] P. De Wolf, E. Brazel, A. Erickson, *Mater. Sci. Semicond. Process.* **4**, 71 (2001); D. Álvares, J. Hartwich, J. Kretz, M. Fouchier, W. Vandervorst, *Microelectron. Eng.* **67-68**, 945 (2003); *Scanning Spreading Resistance Microscopy, Support Note No. 294. Rev. A*, Digital Instrument, (2000).
- [17] J. Osterman, L. Abtin, U. Zimmermann, M. S. Janson, S. Anand, C. Hallin, A. Hallén, *Mater. Sci. Eng. B* **102**, 128 (2003); John Österman, *Characterization of Electrical Properties of 4H-SiC by Imaging Technique*, Doctoral Thesis, Royal Institute of Technology, (2004).
- [18] R. P. Lu, K. L. Kavanagh, St. J. Dixon-Warren, A. J. SpringThorpe, R. Streater, I. Calder, *J. Vac. Sci. Technol. B* **20**(4), 1682 (2002); R. P. Lu, K. L. Kavanagh, St. J. Dixon-Warren, A. Kuhl, A. J. SpringThorpe, E. Griswold, G. Hillier, I. Calder, R. Arés, R. Streater, *J. Vac. Sci. Technol. B* **19**(4), 1662 (2001).
- [19] K. Maknys, O. Douhéret and S. Anand, *Appl. Phys. Lett.* **83**(11), 2184 (2003).
- [20] P. Eyben, D. Alvarez, M. Jurczak, R. Rooyackers, A. De Keersgieter, E. Augendre, W. Vandervorst, *J. Vac. Sci. Technol. B* **22**(1), 364 (2004).
- [21] M. Mizukami, O. Takikawa, M. Murooka, S. Imai, K. Kinoshita, T. Hatakeyama, M. Tsukuda, W. Saito, I. Omura, T. Shinohe, *Mat. Sic. Forum* **457-460**, 1217 (2004).

- [22] *Instruction manual* V. 4.11, Digital Instruments, Feb. 1996; *Command reference manual* V.5.12 Rev. B, April (2003).
- [23] L. Zhang, C. Israel, A. Biswas, R. L. Greene, A. De Lozanne, Sciencexpress, 1077346 (2002).
- [24] R. Desfeux, S. Bailleul, A. De Costa, W. Prellier, A. M. Haghiri-Gosnet, Appl. Phys. Lett. **78**(23), 3681 (2001); Joonghoe Dho, Y. N. Kim, Y. S. Hwang, J. C. Kim, and N. H. Hur, Appl. Phys. Lett. **82**(9), 1434 (2003).
- [25] M. Rajeswari, A. Goyal, A. K. Raychaudhuri, M. C. Robson, G. C. Xiong, C. Kwon, R. Ramesh, R. L. Greene, T. Venkatesan, Appl. Phys. Lett. **69**(6), 851 (1996).
- [26] M. Rajeswari, R. Shreekala, A. Goyal, S. E. Lofland, S. M. Bhagat, K. Ghosh, R. P. Sharma, R. L. Greene, R. Ramesh, T. Venkatesan, T. Boettcher, Appl. Phys. Lett. **73**(18), 2672 (1998).
- [27] P. Reutler, A. Bensaid, F. Herbstritt, C. Höfener, A. Marx, R. Gross, Phys. Rev. B **62**(17), 11619 (2000).
- [28] A. Lisauskas, S. I. Khartsev, A. M. Grishin, Appl. Phys. Lett. **77**(5), 756 (2000); A. Lisauskas, J. Bäck, S. I. Khartsev, A. M. Grishin, J. Appl. Phys. **89**(11), 6961 (2001).
- [29] A. Palanisami, M. B. Weissman, N. D. Mathur, Phys. Rev. B **71**, 014423 (2005).
- [30] A. Lisauskas, S. I. Khartev and A. M. Grishin, J. Low Temp. Phys. **117**, 1647 (1999); Alvydas Lisauskas, *Electrical Noise in Colossal Magnetoresistors and Ferroelectrics*, Doctoral Thesis, Royal Institute of Technology, (2001).

5. Microfabrication of IR CMR bolometer

5.1 General aspects

To fabricate CMR manganite IR detector, there are three main steps for micro patterning. Fig. 5-1 shows the basic micromachining process.

After deposition of CMR films on substrate, described in chapter 3, lithography process was executed to transfer patterns on photoresist or metal mask layer through photomask or direct pattern writing. Finally, desired micro patterning was obtained by optimized etching process. By etching process, patterned area of films, substrates or both of them, are etched. This process can be repeated until reaching the final goal of micromachining [1, 2].

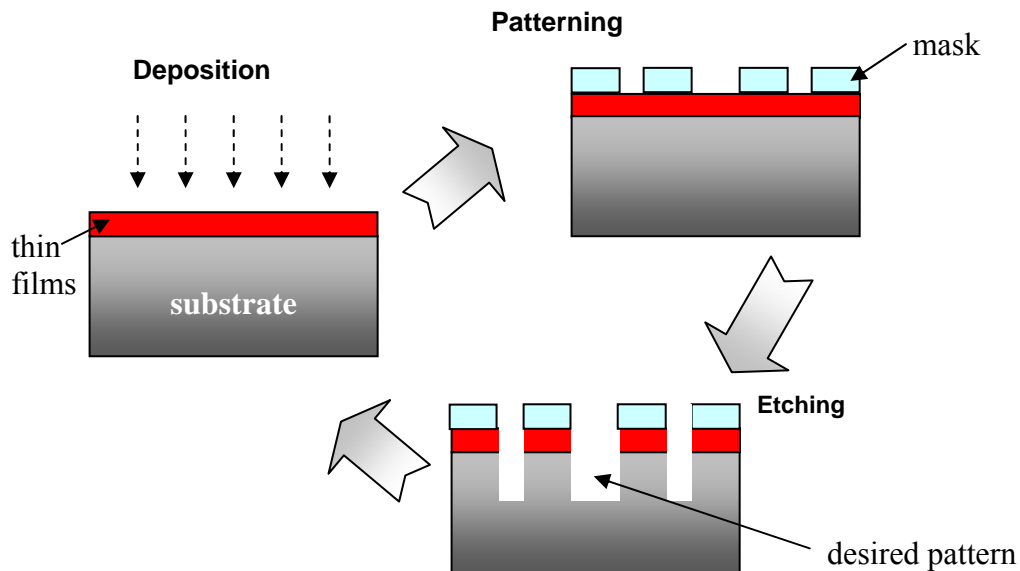


Figure 5-1. Basic micromachining processes.

5.2 Patterning for CMR manganites

Patterning process is transferring of desired image to films or substrate. Two parameters of patterning are important: patterning method (= lithography) and mask material. Lithography process is to define the pattern shape of mask on layer by optical exposure with short wavelength. Recently other techniques, electron beam lithography (EBL) [3, 4], x-ray lithography (XRL) [5] and nano-imprint lithography (NIL) [6] have been used for nanoscale patterning. Wolfman *et al* demonstrated a nanoscale- domain wall of $\text{La}_{0.7}\text{Sr}_{0.3}\text{MnO}_3$ (LSMO) films by EBL and Ar ion beam etching (IBE) for manganite-based devices [3]. Also, Ono *et al* fabricated 10 μm LSMO wire by 30 keV Ga^+ focused ion beam (FIB) etching [7].

For mask layers, photoresist (PR), metal films or dielectric SiO_2 and Si_3N_4 are widely used. In general, Al metal mask is widely used for manganite and magnetic

materials with lift-off technique. But Al layers are easily oxidized and selectivity is around 2 over CMR manganites films by Ar ion beam etching (IBE), where selectivity is the ratio of etch rate for films over etch rate for mask [8, 9]. Another metal mask, Cr by IBE was studied by Bowen *et al* [10]. Alternatively, Ti mask with reactive ion etching (RIE) was investigated by Naoe *et al* with high selectivity (~ 4.7) over LSMO films grown on STO substrates [11].

However, there are two problems for micro patterning with metal masks. First, manganite oxide films can be also attacked by solutions to etch the metal mask on manganite films. Second, metal mask processing is more complex compared to conventional PR patterning. Barth *et al* fabricated 3 μm -wide YBCO microbolometer on YSZ buffered Si substrates with PR patterning [12]. Wang *et al* utilized preannealed PR technique to etch superconducting oxides with thick PR mask by Ar IBE. The etch rate for a preannealed PR is lower than oxide layer [13]. Soulimane *et al* studied manganite Mott field effect transistor (FET) with PR masking technique. The etch rate for PR is 2~3 times higher than manganite films [14]. Recently, Li *et al* demonstrated nanosize patterning of $\text{La}_{0.8}\text{Ba}_{0.2}\text{MnO}_3$ with contact mode atomic force microscopy (AFM) technique [15].

5.3 Etching of CMR manganites

There are three important issues for successful etching: selectivity, mask choice and etching method. In general, etching types can be classified by four categories. isotropic, anisotropic in dry and wet methods. The two former are related to the crystallographic planes and the latter to etching mediums. Fig. 5-2 shows the schematics of different etching methods.

The etching methods for the high CMR manganites are few even though their promising device potential. The first reason of that is deposition difficulty of the CMR films on conventional semiconductor substrates, second is that CMR manganites, compared with conventional semiconductor materials, are hard materials not easy to be etched. The main etching technique of CMR manganite is Ar IBE. Another alternative etching techniques are pulsed excimer laser etching [16], reactive ion etching (RIE) [11], and focused ion beam (FIB) etching [7]. Dry etching of thin manganite films on SrTiO_3 by the CO/NH_3 RIE was studied and 15~70 nm/min etch rate and high selectivity (~ 4.7) over Ti mask are achieved [11].

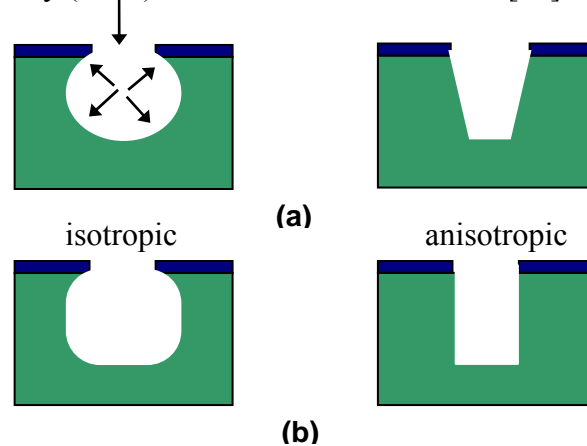


Figure 5-2. Schematic drawing of trench cross-section by different type (a) wet etching and (b) dry etching.

For wet etching of manganite films grown on silicon substrates, a concentrated buffered hydrofluoric acid (BHF) and potassium hydroxide (KOH) solutions were used. KOH is common applied in Si etching processes. Because the etching mechanism of KOH is reaction rate limited, the etch rate for Si varies according to etching condition, such as concentration, temperature and substrate orientation [17, 18]. Here for the purpose of fast etch rate in bulk/surface micromachining, 23% w.t (weight percent) KOH concentration and 80°C was determined. BHF (87.5% NH_4F : 12.5% HF) is also well known for oxide etching solution with PR mask, therefore etching of LSCMO films on Si was performed in room temperature. For this purpose, Clariant AZ 1813 (thin PR) and Shipley 5740 (thick PR) were used for etching and preannealed PR technique for manganite oxide and buffer layers with lithography step (*i*-line, Karl Süss MA6).

For comparison with wet etching, dry etching was performed by using Ar ion beam etching (IBE, Veeco Microetch). The normal incident Ar IBE process was performed under 10^{-7} Torr background and 2×10^{-4} Torr working pressure of Ar gas. The 600 V accelerated potential with ion beam current density 1.2 and 1.6 mA/cm^2 for buffer layers and Si was applied.

To get etch rates for LSCMO manganite films on oxide buffered Si substrates, four sequential samples, LSCMO/BTO/ CeO_2 /YSZ/Si, BTO/ CeO_2 /YSZ/Si, CeO_2 /YSZ/Si and YSZ/Si, were prepared. Properties of selected materials are shown in Table IX.

Table IX. Properties of selected materials [1, 19]

	Si	SiO_2	Si_3N_4	YSZ	CeO_2	$\text{Bi}_4\text{Ti}_3\text{O}_{12}$
Thermal conductivity @ 300K ($\text{W}/\text{cm}\cdot\text{K}$)	1.57	0.014	3.1	0.015	0.12	-
Specific heat ($\text{J}/\text{g}\cdot\text{K}$)	0.7	1.0	0.7	0.63	0.46	0.61
Density (g/cm^3)	2.33	2.3	3.1	5.97	7.28	8.05
Bonding strength (KJ/mol)	325 (Si-Si)	798 (Si-O)	470 (Si-N)	776 (Zr-O)	795 (Ce-O)	672 (Ti-O)

5.4 Fabrication of free standing manganite membrane

The schematics of the fabrication process of free standing LSCMO microbolometer on Si is shown in Fig. 5-3.

The processing begins with spin coating of 10.5 μm -thick photoresist (PR, Shipley 5740) on LSCMO films grown on Si. Using slow temperature increase with $15^\circ\text{C}/\text{min}$, the PR layer was preannealed on 100°C hot plate during 30 min. After that, additional slow-cooling process was necessary to minimize thermal shock on preannealed PR. To absorb more moisture from the environment, 1 hour duration in air followed after cooling.

In order to transfer the microbolometer pixels on preannealed PR layer, *i*-line lithography process was used.

As mentioned before, oxide buffer layers and CMR manganites are very strong materials, Ar IBE process was employed to etch the LSCMO films/oxide buffers down to silicon substrates.

At this stage, $\text{SF}_6/\text{C}_4\text{F}_8$ inductively coupled plasma (ICP, STS Multiplex) was executed for anisotropic Si etching to make deep trenches. Then isotropic Si etching with SF_6 was performed to remove the silicon substrates beneath the pixel areas. The isotropic etch rate for silicon substrates in ICP process were around $3.0 \mu\text{m}/\text{min}$ in following conditions: 600 W coil power, 12 W platen power and 130 sccm of SF_6 gas flow.

At the final stage, the residual PR on the patterned LSCMO surface was removed by oxygen plasma and a self-supported free standing CMR manganite microbolometer arrays were obtained.

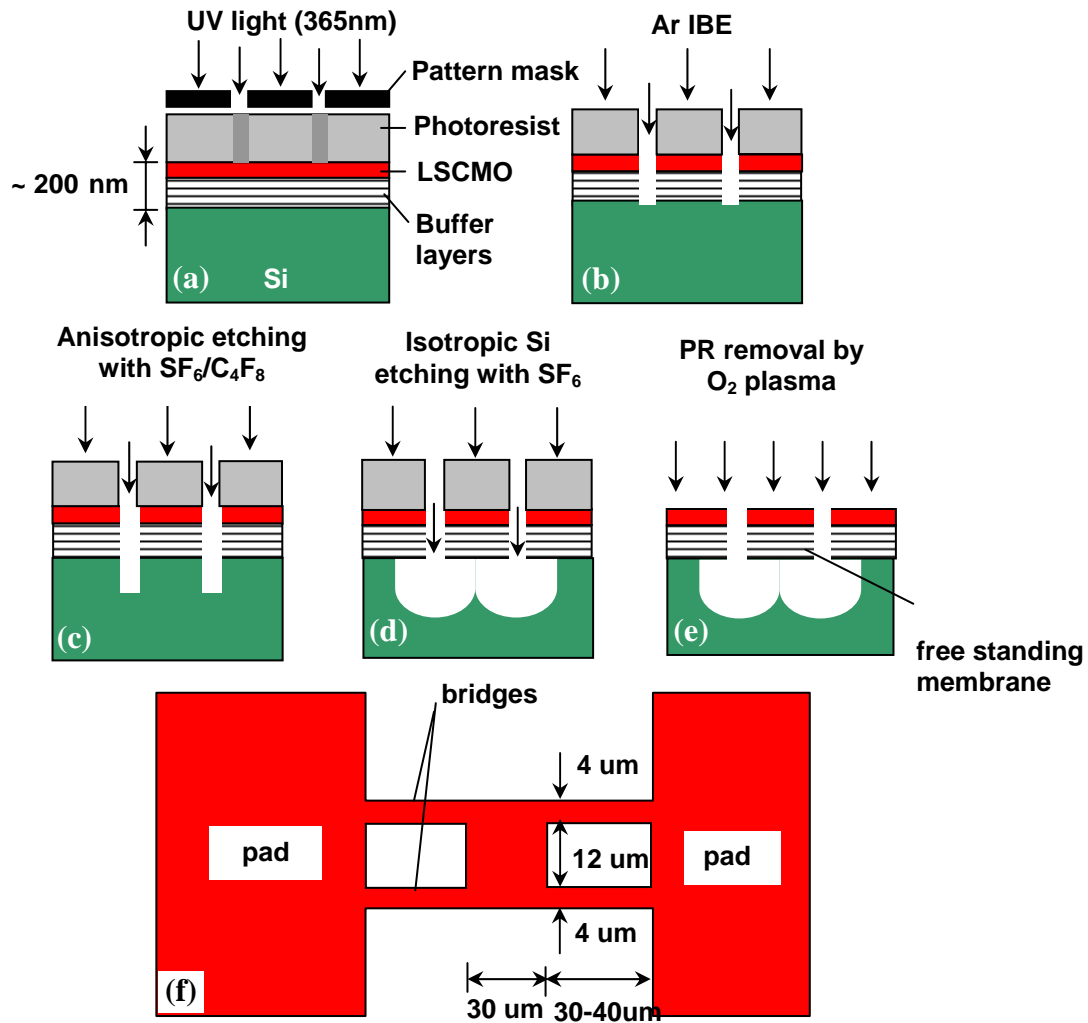


Figure 5-3. Process flow of free standing CMR microbolometer on Si. (a) pixel patterning (b) Ar ion beam etching of manganite and buffer oxides (c) deep trench on Si substrates by $\text{SF}_6/\text{C}_4\text{H}_8$ passivation (e) isotropic etching to remove Si beneath pixel structure (e) PR removal (f) microbolometer pixel geometry.

References

- [1] Nadim Maluf, *An Introduction to Microelectromechanical System Engineering*, Artech House, Boston and London, (2000).
- [2] P. Rai-Choudhury, *MEMS and MOEMS Technology and Application*, SPIE Press, Washington, (2000).
- [3] J. Wolfman, A. M. Haghiri-Gosnet, B. Raveau, C. Vieu, E. Cambril, A. Cornette, H. Launois, J. Appl. Phys. **89**(11), 6955 (2001).
- [4] T. Niizeki, H. Kubota, Y. Ando, T. Miyazaki, J. Magn. Mater. **272-276**, 1947 (2004).
- [5] F. Cerrina, J. Phys. D: Appl. Phys. **33**, R103 (2000).
- [6] J. I. Matín, J. Nogués, Kai Liu, J. L. Vicent, Ivan K. Schuller, J. Magn. Mater. **256**, 449 (2003).
- [7] T. Ono, A. Kogusu, S. Morimoto, S. Nasu, A. Masuno, T. Terashima, M. Takano, Appl. Phys. Lett. **84**(13), 2370 (2004).
- [8] A. M. Haghiri-Gosnet, T. Arnal, R. Soulimane, M. Koubaa, J. P. Renard, Phys. Stat. Sol. (a) **201**, 1392 (2004).
- [9] J. Wolfman, A. M. Haghiri-Gosnet, B. Raveau, C. Vieu, E. Cambril, A. Cornette, H. Launois, J. Appl. Phys. **89**(11), 6955 (2001).
- [10] M. Bowen, M. Bibes, A. Barthélémy, J.-P. Contour, A. Anane, Y. Lemaître, A. Fert, arXiv:cond-mat. **1**, 0211158 (2002).
- [11] M. Naoe, K. Hamaya, N. Fujiwara, T. Taniyama, Y. Kitamoto, Y. Yamazaki, J. Magn. Mater. **235**, 223 (2001).
- [12] R. Barth, J. Siewert, B. Spangenberg, Ch. Jaekel, H. Kurz, B. Utz, W. Prusseit, H. Kinder, IEEE Tran. Appl. Supercond. **5**(2), 2423 (1995).
- [13] Y. M. Wang, A. Zettl, S. Ooi, T. Tamegai, Phys. Rev. B **65**, 184506 (2002).
- [14] R. Soulimane, M. Koubaa, A. M. Haghiri-Gosnet, B. Mercey, W. Prellier, Ph. Lecoeur, G. Poullain, R. Bouregba, Phys. Stat. Sol. (c) **1**(7), 1687 (2004).
- [15] R.-W. Li, T. Kanki, H.-A. Tohyama, M. Hirooka, H. Tanaka, T. Kawai, Nanotechnology **16**, 28 (2005); R.-W. Li, T. Kanki, H.-A. Tohyama, J. Zhang, H. Tanaka, A. Takagi, T. Matsumoto, T. Kawai, J. Appl. Phys. **95**(11), 7091 (2004).
- [16] A. M. Dhote, R. Shreekala, S. I. Patil, and S. B. Ogale, T. Venkatesan, C. M. Williams, Appl. Phys. Lett. **67**(24), 3644 (1995).
- [17] H. Seidel, L. Csepregi, A. Heuberger, H. Baumgarel, J. Electrochem. Soc. **137**(11), 3626 (1990).
- [18] K. R. Williams, R. S. Muller, J. Microelectromech. Sys. **5**(4), 256 (1996); K. R. Williams, K. Gupta, M. Wasilik, J. Microelectromech. Sys. **12**(6), 761 (2003).
- [19] David R. Lide, ed., *CRC Handbook of Chemistry and Physics*, Internet Version 2005, <<http://www.hbcpnetbase.com>>, CRC Press, Boca Raton, FL, (2005).

6. Free standing micromachined epitaxial CMR membrane for uncooled infrared bolometer

To obtain high sensitive IR bolometer at room temperature, there are many attempts to develop new sensing materials and microfabrication of structures. The electrical, magnetic and noise properties are related to materials whereas microfabrication of structures affects the working properties of bolometers: relaxation time τ_{th} , responsivity \mathcal{R}_V and detectivity D of microbolometer.

Due to the thermo-electrical link between supporting structure and sensing material via thermal conductance G_{th} , micromachining of the free standing membrane is necessary to achieve high detective bolometer at room temperature [1]. The expected highest possible detectivity of thermal detector in room temperature is $1.8 \times 10^{10} \text{ cm} \cdot \sqrt{\text{Hz/W}}$ [2]. Potentially, pixel-by-pixel tuning by electronic circuit enables the real-time reconfiguration of the focal plane arrays (FPA) providing spectral tuning as well as high temporal and spatial resolution of the scene sampling. Therefore, all previous research of bolometric applications can be classified: materials and microfabrication techniques to enhance the bolometric sensitivity.

For microfabrication of bolometer, to minimize the thermal effect G_{th} from the surrounding, Méchin *et al* fabricated suspended epitaxial YBCO bolometer on CeO_2/YSZ buffered Si and SIMOX substrates [3]. Later, Rice *et al* demonstrated free standing antenna-coupled YBaCuO microbolometer on YSZ buffered Si [4]. Cole *et al* constructed monolithic VO_x microbolometer with SiN membrane [5]. Fuflyigin *et al* suggested free standing $\text{PbSc}_{0.5}\text{Ta}_{0.5}\text{O}_3$ (PST) films on Si for uncooled infrared detector [6]. Lakew *et al* demonstrated suspended YBaCuO microbolometer on sapphire substrate [7]. Recently, Dayeh *et al* showed the micromachined YBaCuO bolometer on flexible polyimide substrates using carrier substrate technique [8]. Han *et al* developed free standing tungsten substituted VO_x microbolometer on SiN membrane with high detectivity $1.0 \times 10^9 \text{ cm} \cdot \sqrt{\text{Hz/W}}$ [9].

In spite, several papers related to growth of CMR manganite films were published [10-14]; still, there are very few publications for microfabrication of the epitaxial CMR manganite bolometer. Therefore, in this chapter, microfabrication of self-supported epitaxial LSCMO bolometer on Si substrates including wet/dry etching studies will be presented. Note that the micromachined CMR manganite bolometer was evaluated without readout circuit and optical system.

6.1 Wet and dry etching results

As mentioned before, KOH and concentrated BHF were used for wet etching the CMR manganite films. For Si (001) substrate, etch rate was about $1.12 \mu\text{m}/\text{min}$ after 3 hours KOH etching, consistent with many references [15, 16]. However, the KOH etchant did not etch the LSCMO films and buffer oxide layers. After 1 hour KOH etching, etch rate measurement of LSMO and buffer layers was very difficult due to

very low rate. X-ray analysis was performed at this stage to ensure the existence of the CMR films shown in Fig. 6-1.

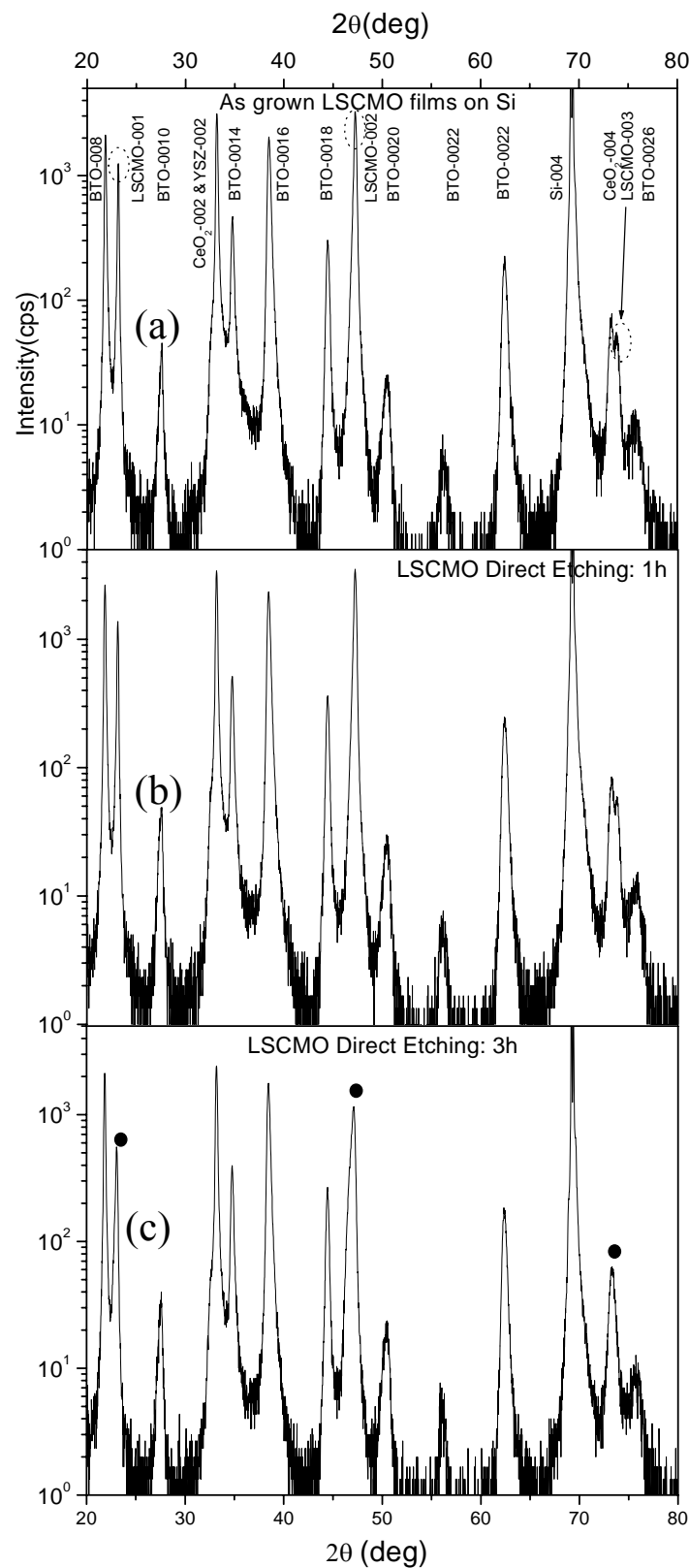


Figure 6-1. XRD results of (a) as grown LSCMO/BTO/CeO₂/YSZ on Si (b) after 1 hour KOH etching (c) 3 hours KOH etched sample.

After 3 hours KOH wet etching, XRD shows a difference of LSCMO peaks as illustrated in Fig. 6-1. Full width half maximum (FWHM) decreases by elapsed time of KOH etching time (see the circle in Fig. 6-1a, dots in Fig. 6-1c). The FWHM of 3 hours KOH etched LSCMO-002 peak was 40% larger than as grown. Slightly reduced LSCMO peaks indicate an etching evidence for CMR manganite layer by KOH. For more detail investigation of the KOH wet etching, the etched surface was shown by scanning electron microscopy (SEM) in Fig. 6-2.

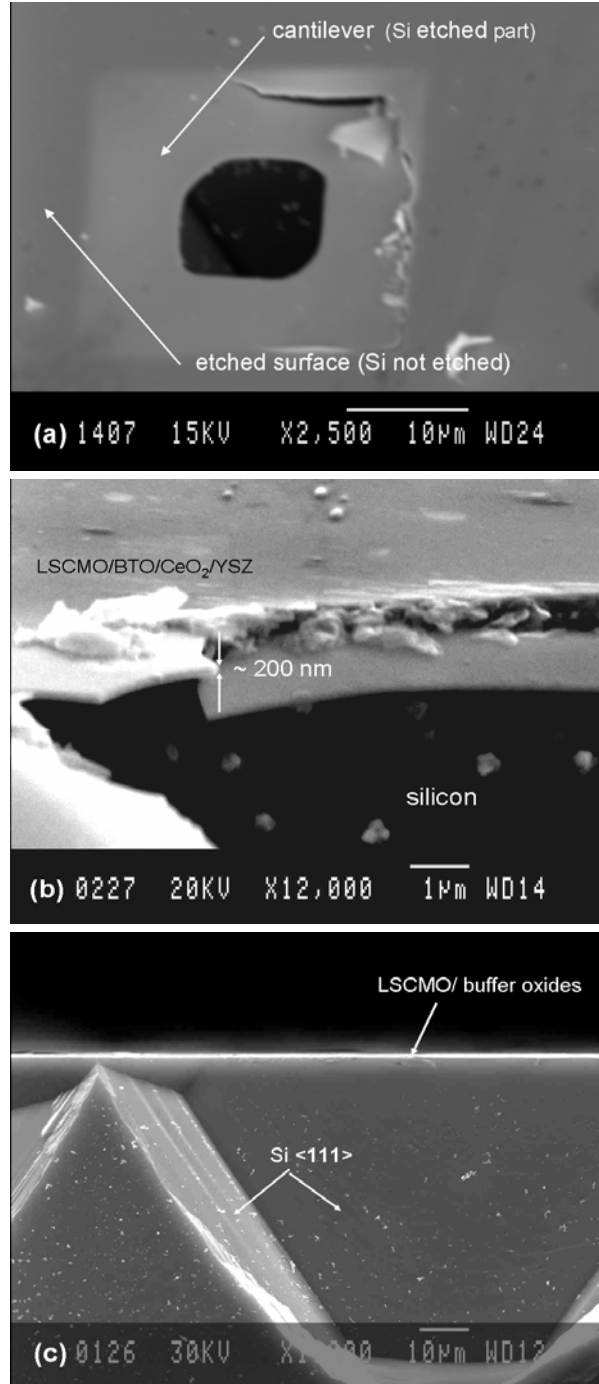


Figure 6-2. SEM images of LSCMO films on BTO/CeO₂/YSZ buffered on Si after 3 hours KOH wet etching (a) 45° tilt view. White area represents LSCMO/oxides films with etched beneath Si. (b) free standing LSCMO cantilever part (c) cross section view.

The etched surface of LSCMO films after 3 hours KOH etching is shown in Fig. 6-2(a). There are different sized holes (= Si cavity) on the surface that indicate KOH penetrated LSCMO films and oxide buffer layers and eventually etched the silicon substrates beneath the CMR films and buffer layers. The reason seems that due to *non*-uniform defect distribution over LSCMO crystal generated some weak areas which were etched by KOH. In the beginning, very small holes appeared on the surface and later they merged to make big holes (= cavity) where thin LSCMO/oxide buffer layer membrane remained as free standing (bright part), partly bent inside due to releasing the tensile strain induced from films-substrates mismatch. However, LSCMO and oxide buffer layers still seems to be reserved due to very low etch rate in Fig. 6-2(b). The thickness of LSCMO/oxide layers seems around 200 nm close to deposited thickness. In Fig. 6-2 (c), the cross-section of 3 hours KOH etched LSCMO sample shows more clear image for KOH wet results.

Therefore, the results of KOH wet etching imply that the LSCMO layer is chemically resistant against KOH. The great advantages of KOH etching is high selectivity micromachining of CMR films on Si. Ultimately, without protecting mask for CMR films on silicon, only silicon substrates can be etched by KOH solution.

In case of BHF etching, the patterned LSCMO films are shown in Fig. 6-3 after 1 min BHF etching. The pattern, in Fig. 6-3(a), was transferred to LSCMO films. Slightly blemish area in the patterned area are due to different thickness caused by etching (see Fig. 6-3b).

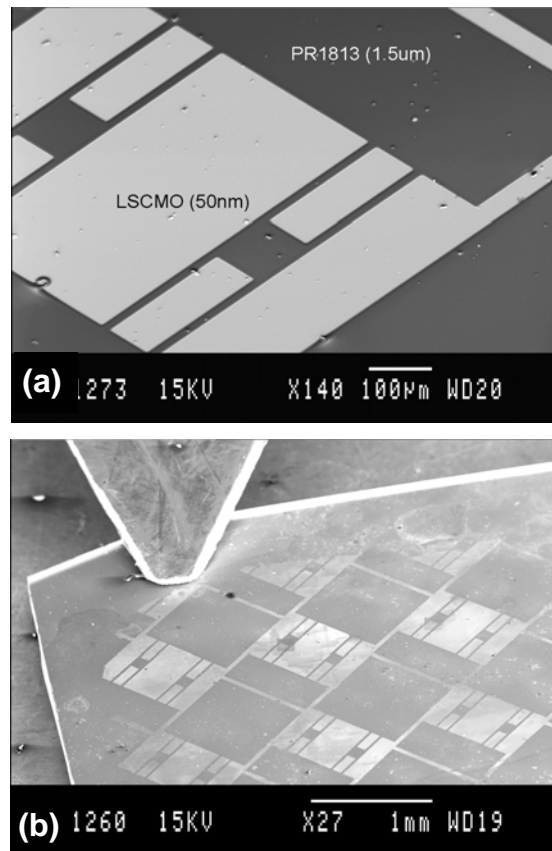


Figure 6-3. SEM images of LSCMO/Bi₄Ti₃O₁₂/CeO₂/YSZ on Si substrates (a) after patterning (b) Etched LSCMO films after 1 min BHF etching. Dark part is PR masked LSCMO area.

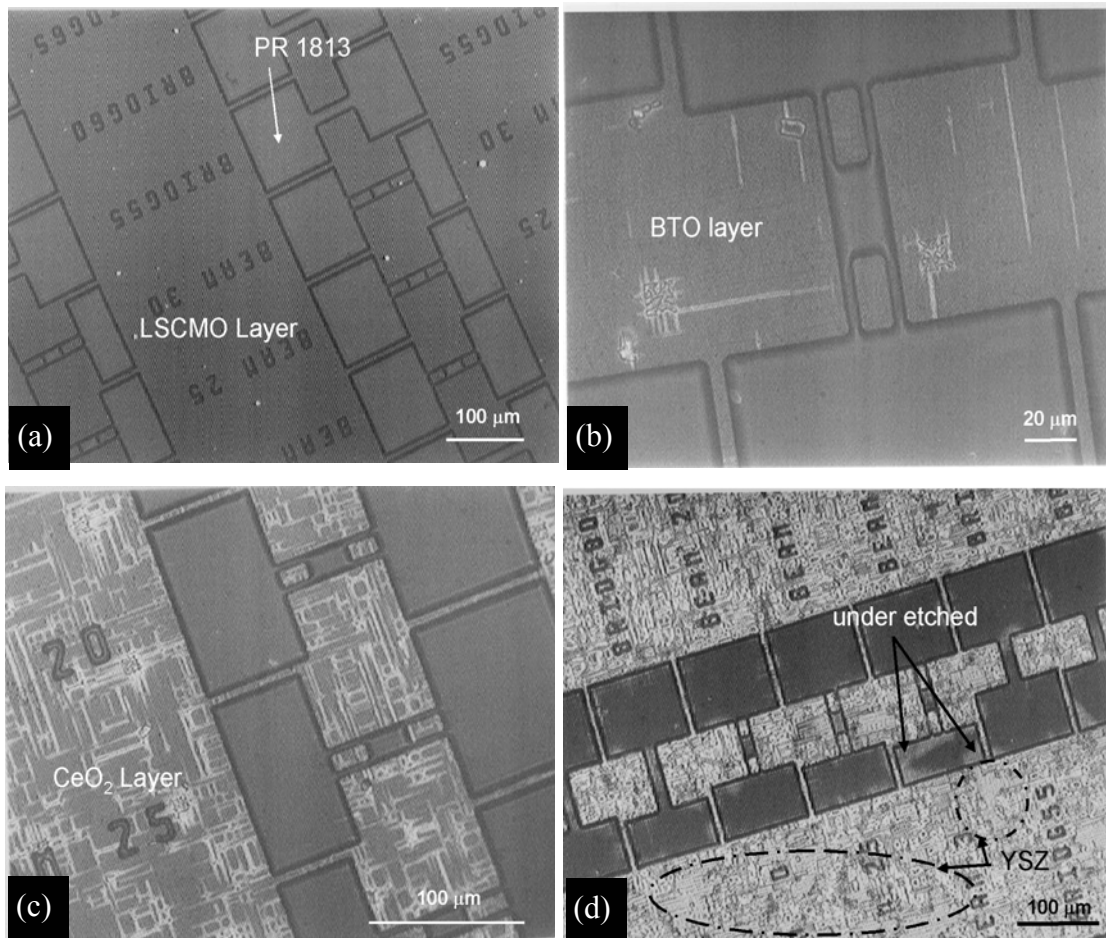


Figure 6-4. BHF wet etching of LSCMO/ $\text{Bi}_4\text{Ti}_3\text{O}_{12}$ / CeO_2 /YSZ on Si substrates (a) after 1 min (LSCMO layer) (b) after 7 min ($\text{Bi}_4\text{Ti}_3\text{O}_{12}$.layer) (c) after 20 min (Ce_2O layer) (d) after 35 min (Ce_2O layer), YSZ layer was recognized by delaminated area of CeO_2 . Also some of PR masked areas were under-etched by BHF.

Fig. 6-4 illustrates microscopic images of the BHF etching progress with elapsed etching time. The etch rates for LSCMO and BTO layers are 22 and 17 nm/min, respectively. PR patterns on LSCMO films, shown Fig. 6-4(a), is easily transferred due to high selectivity and fast etch rate until BTO layer shown in Fig. 6-4(b).

However, due to the low etch rate for CeO_2 , the BHF seems to attack local crystal defects with different etch rates. Fig. 6-4(c) shows the side-etched area of layer beneath the PR pattern. Finally, some of the area of the CeO_2 layer is delaminated and YSZ layer partially appears in Fig. 6-4(d).

Table X. Comparison of etch rates by dry and wet etching methods.

Layers	Etching methods	Etch rate (nm/min)		
		Dry etching (Ar IBE, 600V @ 2×10^{-4} Torr)	Wet etching	
			KOH (23% w.t and 80°C)	BHF (7 NH ₄ F : 1 HF)
La _{0.67} (Sr,Ca) _{0.33} MnO ₃		16 ± 1.0	low	22 ± 1.0
Bi ₄ Ti ₃ O ₁₂		15 ± 1.5	very low	12 ± 1.0
CeO ₂		17 ± 1.0	very low	1.5 ± 0.5
YSZ		17 ± 0.7	very low	low
Si		24 ± 0.5	1100 ± 20	low

The etching results by dry and wet methods for LSCMO and oxide buffer layers including Si are summarized in Table X.

For Ar IBE, the obtained etch rates for LSCMO and buffer oxides are lower than for silicon substrates, mainly due to the higher strength of ionic bonds in oxides compared to the covalent in Si shown in Table XI. Calculating the obtained etch rates for LSCMO and buffer oxides, 13-14 min of etching time is required to etch down the LSCMO/buffer oxides to the bare Si substrates.

Table XI. Selected properties of oxides and substrate [17, 18]

	Si	SiO ₂	Si ₃ N ₄	YSZ	CeO ₂	Bi ₄ Ti ₃ O ₁₂
thermal conductivity @ 300 K (W/cm·K)	1.57	0.014	3.1	0.015	0.12	-
specific heat (J/g·K)	0.7	1.0	0.7	0.63	0.46	0.61
density(g/cm ³)	2.33	2.3	3.1	5.97	7.28	8.05
bonding strength (KJ/mol)	325 (Si-Si)	798 (Si-O)	470 (Si-N)	776 (Zr-O)	795 (Ce-O)	672 (Ti-O)

6.2 Microfabrication of free standing epitaxial manganite films for IR bolometer

To realize free standing LSCMO membrane on Si substrates, thick PR (Shipley 5740) was used as a protective layer against Ar IBE and ICP. While the hard baked photoresist (10 min at 105 °C hot plate) was burnt during the Ar IBE process in Fig. 6-

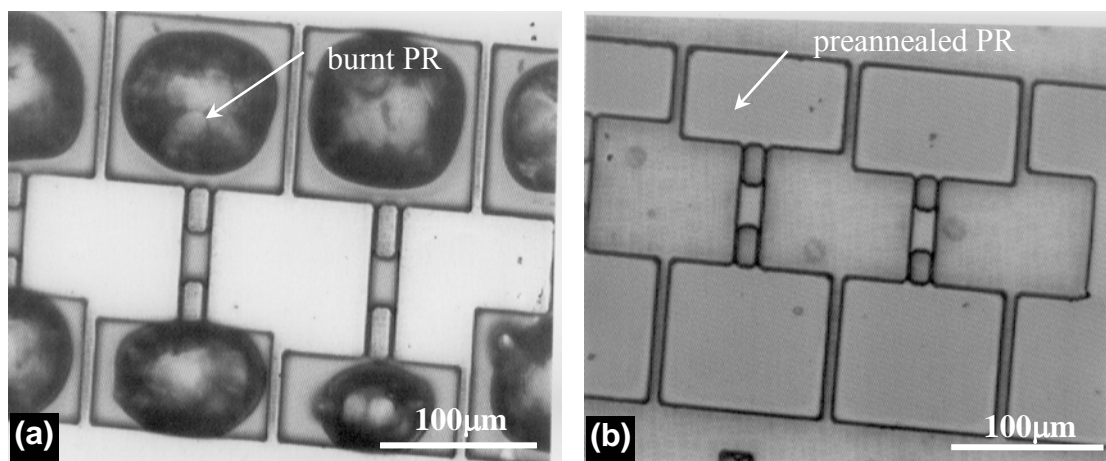


Figure 6-5. Microscopic images of hard baked and pre-annealed photoresist after IBE process (a) hard baked PR. Dark is burned PR area (b) pre-annealed sample.

5(a), the preannealed photoresist (30 min at 100 °C at hot plate), in Fig. 6-5(b), shows the absence of any burning traces in preannealed photoresist after Ar IBE [19].

Fig. 6-6 shows the etched LSCMO/BTO/CeO₂/YSZ on Si after 13 min Ar IBE process. The preannealed PR is still well preserved during Ar IBE process.

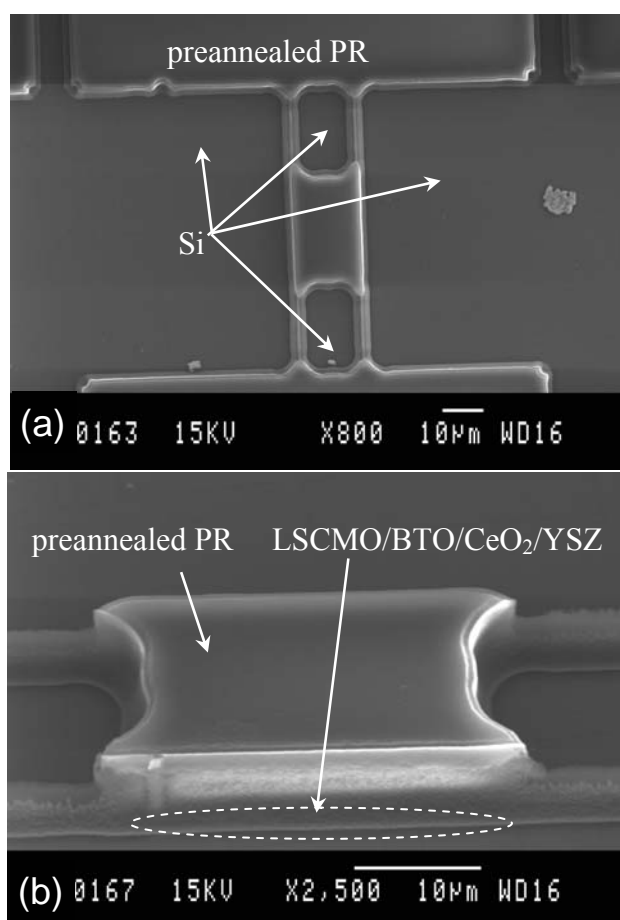


Figure 6-6. SEM images of pre-annealed photoresist (a) top view of pre-annealed photoresist sample (b) 45° tilt side view.

For the free standing membrane, etching/passivation process was executed to make 20~30 μm deep trenches into the silicon substrates by inductively coupled plasma (ICP) process using $\text{SF}_6/\text{C}_4\text{F}_8$ cycle. Then, isotropic etching was performed with SF_6 gas to remove the silicon substrates beneath the oxide multi-layer and form free standing membranes. At the final stage, the residual PR on the patterned LSCMO surface was removed by oxygen plasma.

After successive etching process, arrays of 20 $\mu\text{m} \times 30 \mu\text{m}$ free standing LSMO ($\text{La}_{0.75}\text{Sr}_{0.25}\text{MnO}_3$) pixels were fabricated on silicon substrates. The 45° side views of self-supported free standing multi-layered oxide film membranes are shown in Fig. 6-7.

The underlying Si was completely etched by the ICP process and the LSMO film with buffer oxide layers appeared to be suspended onto the legs leaning upon the pads on the non-etched part of silicon substrates. The border of the pads shows under-etched area (white color) and middle part (dark) represents not etched. Due to strain release of the thin film, border parts of the pads are slightly bent. Specially, in Fig. 6-7(b), the membrane tore-off one leg from the Si substrates and rolled up as the tensile film-to-substrate mismatch strain was released.

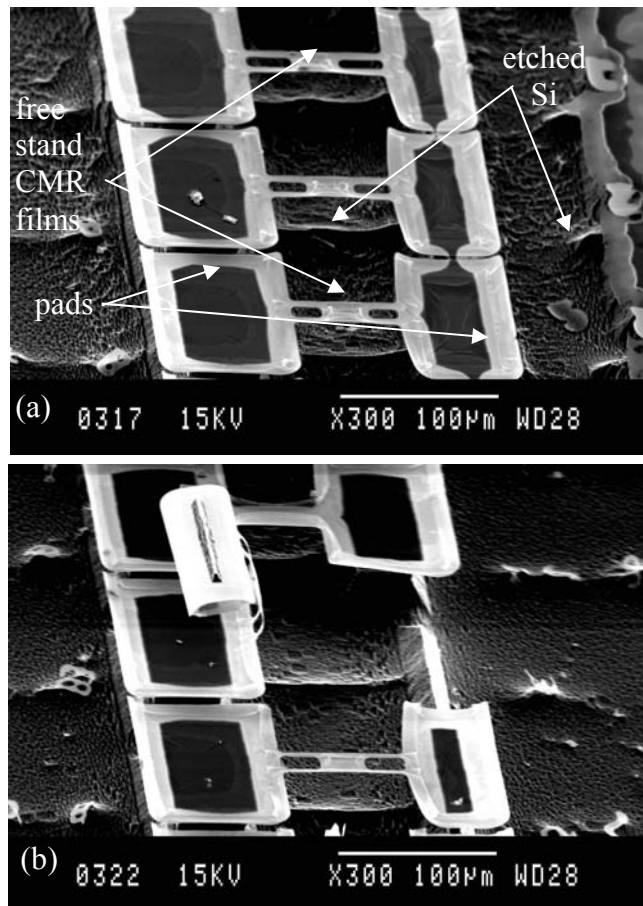


Figure 6-7. SEM images of (a) array of 20 $\mu\text{m} \times 30 \mu\text{m}$ free standing heteroepitaxial LSMO/ $\text{Bi}_4\text{Ti}_3\text{O}_{12}$ / CeO_2 /YSZ membranes onto the etched Si substrate. (b) tear-off leg from Si substrate by strain release.

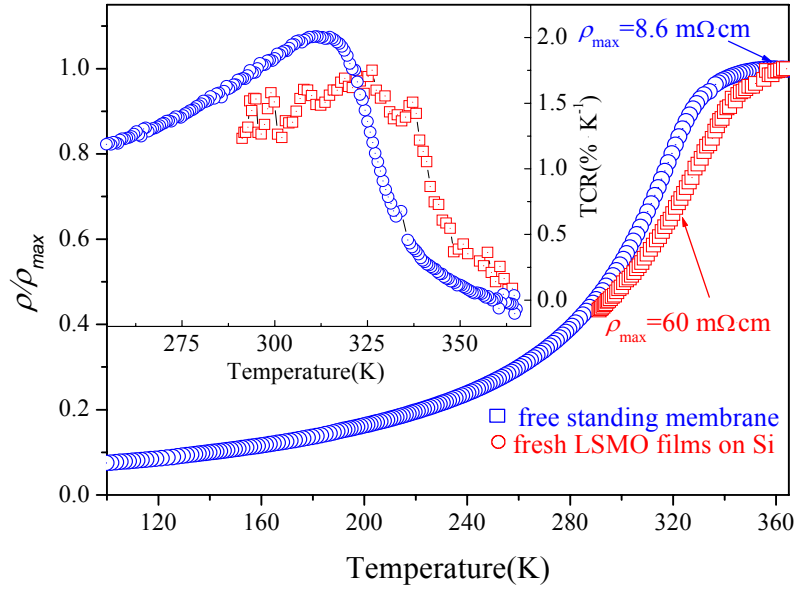


Figure 6-8. Temperature dependant resistivity of free standing $\text{La}_{0.75}\text{Sr}_{0.25}\text{MnO}_3$ films and as-grown sample. Inset is the corresponding TCR values of both samples.

The corresponding temperature dependency of the resistivity and TCR of LSMO films on silicon substrates before the micromachining and in free standing LSMO membrane by four-point measurements are represented in Fig. 6-8. 10 K increase of T_c and 20% decrease of the TCR of LSMO films would stem from the release of tensile strain and the affect of multi micromachining process. However, the self-supported free standing CMR membrane presents a possible feasibility of the perovskite CMR manganite films on silicon substrates for bolometric applications [20].

Therefore, this microfabrication technique for CMR materials will open the way for spin-related devices with the matured semiconductor technology.

References

- [1] A. Rogalski, *Progress in Quantum Electronics* **27**, 59 (2003).
- [2] J. C. Brasunas, B. Lakew. R. Fettig, *Sensors and Actuators A* **96**, 211 (2002).
- [3] L. Méchin, J.-C. Villégier, D. Bloyet, *J. Appl. Phys.* **81**(10), 7039 (1997).
- [4] J. P. Rice, E. N. Grossman, D. A. Rudman, *Appl. Phys. Lett.* **65**(6), 773 (1994).
- [5] B. E. Cole, R. E. Higashi, R. A. Wood, *Proc. IEEE* **86**, 1679 (1998); B. E. Cole, R. E. Harashi, J. A. Ridley, US Patents 6287940B1, Sep. 11, 2001.
- [6] V. Fuflygin, E. Salley, P. Vakhutinsky, A. Osingsky, J. Zhao, I. Gergis, K. Whiteaker, *Appl. Phys. Lett.* **78**(3), 365 (2001).
- [7] B. Lakew, J. C. Brasunas, S. Aslam, D. E. Pugel, *Sensors and Actuators A* **114**, 36 (2004).
- [8] S. A. Dayeh. D. P. Butler, Z. Çelik-Butler, *Sensors and Actuators A* **118**, 49 (2005).
- [9] Y.-H. Han, K.-T. Kim, H.-J. Shin, S. Moon, I.-H. Choi, *Appl. Phys. Lett.* **86**, 254101 (2005).
- [10] A. Goyal, M. Rajeswari, R. Shreekala, S. E. Lofland, S. M. Bhagat, T. Boettcher, C. Kwon, R. Ramesh, T. Venkatesan, *Appl. Phys. Lett.* **71**(17), 2535 (1997).
- [11] J. Y. Gu, C. Kwon, M. C. Robson, Z. Trajanovic, K. Ghosh, R. P. Sharma, R. Shreekala, M. Rajeswari, T. Venkatesan, R. Ramesh, T. W. Noh, *Appl. Phys. Lett.* **70**(13), 1763(1997).
- [12] A. Lisauskas, S. I. Khartsev, A. Grishin, *Appl. Phys. Lett.* **77**(5), 756(2000).
- [13] L. Méchin, F. Yang, J.-M. Routoure, D. Robbes, *J. Appl. Phys.* **93**(10), 8062 (2003).
- [14] R. J. Choudhary, A. S. Ogale, S. R. Shinde, S. Hullavarad, S. B. Ogale, R. N. Bathe, S. I. Patil, R. Kumar, *Appl. Phys. Lett.* **84**(19), 3846 (2004).
- [15] K. R. Williams, K. Gupta, M. Wasilik, *J. Microelectromech. Sys.* **12**(6), 761 (2003).
- [16] H. Seidel, L. Csepregé, A. Heuberger, H. Baumgarel, *J. Electrochem. Soc.* **137**(11), 3626 (1990); G. T. A. Kovacs, N. I. Maluf, K. E. Petersen, *Proc. IEEE* **86**(8), 1536 (1998).
- [17] Nadim Maluf, *An Introduction to Microelectromechanical System Engineering*, Artech House, Boston and London, 2000.
- [18] David R. Lide, ed., *CRC Handbook of Chemistry and Physics, Internet Version 2005*, <<http://www.hbcpnetbase.com>>, (CRC Press, Boca Raton, FL, 2005).
- [19] Y. M. Wang, A. Zettl, S. Ooi, T. Tamegai, *Phys. Rev. B* **65**, 184506 (2002).
- [20] J.-H. Kim, A. M. Grishin, *Appl. Phys. Lett.* **87**, 033502 (2005).

7. Summary and conclusions

This thesis presents the growth of CMR manganite films on Si and GaAs substrate and also material characterization including structural, electrical, magnetic and noise analysis of thin films. Furthermore, wet and dry etching processes in a whole microfabrication scheme of self-supported CMR manganite microbolometer arrays are also demonstrated.

■ Epitaxial CMR manganite films growth on Si and GaAs:

$\text{La}_{0.67}(\text{Sr,Ca})_{0.33}\text{MnO}_3$ (LSCMO) films were grown by PLD technique on Si with $\text{Bi}_4\text{Ti}_3\text{O}_{12}$ (BTO)/ CeO_2 /YSZ buffer layers. The film quality and relations between layers was revealed *cube-on-cube* for $\text{Bi}_4\text{Ti}_3\text{O}_{12}$ / CeO_2 /YSZ/Si and *diagonal-on-side* for LSCMO layer on (BTO) buffer layers. Temperature coefficient of resistivity (TCR) $4.4\% \text{K}^{-1}$ and colossal magnetoresistance (CMR) $\Delta\rho/\rho \sim 2.9\% \text{kOe}^{-1}$ have been reached at room temperature. Assuming a prototype of magnetic field and temperature sensor, noise equivalent magnetic field difference (NEMFD) as low as $260\text{ }\mu\text{Oe}/\sqrt{\text{Hz}}$ at 1 kHz and noise equivalent temperature difference (NETD) of $1.2\text{ }\mu\text{K}/\sqrt{\text{Hz}}$ at 30 Hz were expected at 294K.

In case of GaAs, introducing MgO buffer layer, $\text{La}_{0.67}\text{Ca}_{0.33}\text{MnO}_3$ films show $9.0\% \text{K}^{-1}$ TCR and $7.95\% \text{kOe}^{-1}$ at 223 K and 209 K, respectively. For $\text{La}_{0.67}\text{Sr}_{0.33}\text{MnO}_3$ films $2\% \text{K}^{-1}$ of TCR at 327 K and $1.47\% \text{kOe}^{-1}$ of MR at 295 K were obtained.

■ Strain effect on CMR manganites by $\text{Si}_{1-x}\text{Ge}_x\text{C}_y$ layers on Si:

Strain effect on structural/electrical properties of LSMO on oxide buffered $\text{Si}_{1-x}\text{Ge}_x/\text{Si}$ (compressive, $x=0.05-0.20$) and $\text{Si}_{0.99}\text{C}_{0.01}/\text{Si}$ was studied. Relaxation in the buffer stacks is strongly dependent on the Ge content, which also affects the LSMO layer quality. Strain induced from $\text{Si}_{1-x}\text{Ge}_x$ and $\text{Si}_{1-y}\text{C}_y$ layers tends to decrease the roughness of LSMO films compared to silicon substrates. High resistivity and low TCR values are resulted from samples containing $\text{Si}_{0.8}\text{Ge}_{0.2}$ or $\text{Si}_{0.99}\text{C}_{0.01}$ layers due to higher strain, whereas $\text{Si}_{0.9}\text{Ge}_{0.1}$ and $\text{Si}_{0.95}\text{Ge}_{0.05}$ layers show a slightly improvement in the layer quality and TCR values compared to Si.

■ Wet and dry etching experimental for micro-patterning:

For micropatterning of LSCMO films on Si, wet etching with KOH and BHF and dry etching with Ar IBE were studied. For KOH wet etching, LSCMO layers was strongly chemical resistant against KOH with lower than 0.2 nm/min after 3 hours wet etching. Due to etching effect, wet etched LSCMO films show higher resistivity than as grown by SSRM technique. BHF wet etching showed high etching selectivity over photoresist mask and silicon substrates.

The etch rate LSCMO and BTO by BHF was 22 and 12 nm/min, respectively. For dry Ar etching under gas condition of 2×10^{-4} Torr with 600V, The LSCMO films and oxide buffer layers show similar Ar IBE rates about 16-17 nm/min that are lower compared to 24 nm/min in Si. This difference is caused by higher strength of covalent bonds in oxides compared to ionic bonds in silicon substrates.

■ **Microfabrication free standing CMR membrane bolometer on Si:**

Self-supported free standing heteroepitaxial LSCMO membranes grown on oxide buffered Si was fabricated by Ar IBE and $\text{SF}_6/\text{C}_4\text{F}_8$ ICP etching with a combination of preannealed photoresist technique. The structural investigation by TEM revealed sharp interfaces between layers. The electrical properties of free standing membrane was degraded due to strain release and multi-step etching effect.

Therefore based on this work and appended papers, the major conclusions are

- (1) The heteroepitaxial CMR manganite thin films on silicon substrates were successfully achieved by introducing of proper buffer layers. 4.4 \%K^{-1} high TCR and 2.9 \%kOe^{-1} CMR values for LSCMO on oxide buffered silicon substrates shows the feasibility for bolometric application.
- (2) The LCMO films were successfully grown on MgO buffered GaAs substrates with 9.0 \%K^{-1} of TCR at 223 K and -7.95 \%kOe^{-1} of MR at 209 K whereas LSMO films showed 2 \%K^{-1} at 327 K and -1.47 \%kOe^{-1} at 295 K.
- (3) The induced strain effect has a strong relation to electrical and structural properties of the CMR films on oxide buffered $\text{Si}_{1-x}\text{Ge}_x/\text{Si}$ and $\text{Si}_{1-y}\text{C}_y/\text{Si}$. Therefore, optimized structural and electrical properties of CMR films will be produced by the minimized induced strain.
- (4) LSCMO CMR manganite films are very resistant against KOH wet etching, however it shows 17 nm/min etch rate by BHF. This is great advantage to fabricate CMR structure on Si with high selectivity in wet etching method compare to plasma etching.
- (5) Microfabrication revealed the feasibility of perovskite manganite films on semiconductor substrate for bolometric and other novel device applications. The microfabrication technique of CMR manganites will give open the way for spintronics with accordance to conventional semiconductor technology.

8. Future works

CMR manganite films are interesting materials due to their huge devices potential for bolometric and spintronics applications. Therefore, a number of scientific reports related to the CMR film growth and corresponding microfabrication have been increased in recent years. However, few investigations of CMR films grown on semiconductor materials and microfabrication have been published.

To merge CMR manganite thin films with well-matured semiconductor technology, large area deposition techniques such as metal organic chemical vapor deposition (MOCVD), magnetron sputtering, sol-gel method, and large area PLD technique have to be developed for mass production. Moreover, low temperature growth technique for CMR films is also another important issue to be compatible with CMOS technology and flexible substrates.

Moreover, further investigations of fabrication techniques are necessary for the CMR devices, e.g. bolometer, field effect transistor, non-volatile MRAM, magnetic sensors. To achieve all possibilities of the CMR manganite device applications, effective pattern techniques have to be investigated from microsize to nanoscale. For transferring of the pattern, lithography technology with x-ray lithography (XRL), electron beam lithography (EBL) and nano-imprint (NI) must be introduced for nano-devices. Also wet etching techniques, due to their cheap and easy controlled advantages, is an interesting theme for microfabrication. For nanosize-patterning and vertical etching, reactive ion etching (RIE) or chemical assist ion beam etching (CAIBE) and other dry etching methods are required.

Finally, this thesis partially fulfilled the topics discussed above. Our next goal will be related to extended work based on this thesis. At first, CMR manganite FET on Si will be fabricated. After that, another spin control device, such as CMR manganite magnetic memory (MRAM) will appear.

9. Summary of appended papers

The appended papers are chronologically sorted from the colossal magnetoresistive (CMR) manganite film growth on Si and GaAs substrates to microfabrication of free standing self-supported membrane for uncooled IR microbolometer applications. For systematic strain effects on thin CMR manganite films, the thin manganite films on strained $\text{Si}_{1-y}\text{Ge}_y/\text{Si}$ and $\text{Si}_{1-y}\text{C}_y/\text{Si}$, were investigated.

In the beginning of this study, for infrared bolometer applications, high performance epitaxial $\text{La}_{0.67}(\text{Sr,Ca})_{0.33}\text{MnO}_3$ (LSCMO) films on $\text{Bi}_4\text{Ti}_3\text{O}_{12}/\text{CeO}_2/\text{YSZ}$ buffered Si grown by pulsed laser deposition (PLD) technique were investigated with structural, electrical and noise characterizations.

Later on, for the microfabrication, wet and dry etching studies of CMR manganite films were performed by KOH, BHF and Ar IBE. Different etch rates for CMR LSCMO films, buffer oxide layers and silicon substrates were obtained and compared. To simplify the patterning process, preannealed technique of photoresist (PR) was introduced to prevent from burning by dry etching.

Structural and electrical properties of the etched LSCMO surface and free standing membrane by wet and dry etching were studied by x-ray diffraction (XRD), scanning electron microscopy (SEM), scanning spreading resistance microscopy (SSRM) and magnetic force microscopy (MFM).

For another semiconductor substrate GaAs, using MgO buffer layers, the structural, electrical and magnetic properties of $\text{La}_{0.67}\text{Sr}_{0.33}\text{MnO}_3$ (LSMO) and $\text{La}_{0.67}\text{Ca}_{0.33}\text{MnO}_3$ (LCMO) films were studied.

Strain effects of $\text{Si}_{1-y}\text{Ge}_y/\text{Si}$ and $\text{Si}_{1-y}\text{C}_y/\text{Si}$ on $\text{La}_{0.75}\text{Sr}_{0.25}\text{MnO}_3$ (LSMO) were studied by structural and electrical characterization.

Finally, free standing self-supported CMR manganite membrane microbolometer arrays were demonstrated using conventional Si technology process.

Paper I. This paper presents the colossal magnetoresistive (CMR) $\text{La}_{0.67}(\text{Sr,Ca})_{0.33}\text{MnO}_3$ (LSCMO) films on oxide buffered Si for infrared bolometer by structural, electrical and noise investigation. The author performed structural, electrical and noise measurement including manuscript writing.

Paper II. This paper includes structural, electrical and noise characterization of LSCMO films on $\text{Bi}_4\text{Ti}_3\text{O}_{12}/\text{CeO}_2/\text{YSZ}$ buffered Si. The author contributed structural, electrical, noise measurement. This paper was presented as an invited talk in the international symposium of integrated ferroelectrics (ISIF 2004).

Paper III. This paper shows microfabrication of LSCMO films on Si (001) substrate for bolometer application by Ar ion beam etching (IBE) and SF_6

inductively couple plasma (ICP). The author performed the whole processing and manuscript writing.

Paper IV. This paper shows free standing epitaxial $\text{La}_{1-x}(\text{Sr,Ca})_x\text{MnO}_3$ (LSCMO) pixels on Si for uncooled infrared microbolometer by Ar IBE and ICP process. Stoichiometric and electrical properties of LSCMO films were investigated and compared. The author performed the complete processing, characterization and manuscript writing.

Paper V. This paper includes structural/electrical properties of CMR $\text{La}_{0.67}\text{Sr}_{0.33}\text{MnO}_3$ and $\text{La}_{0.67}\text{Ca}_{0.33}\text{MnO}_3$ films on GaAs semiconductor substrate. The author contributed the optimized deposition condition of CMR films and structural measurement.

Paper VI. This paper discloses the strain effect on structural and electrical properties of $\text{La}_{0.75}\text{Sr}_{0.25}\text{MnO}_3$ films by grown $\text{Si}_{1-x}\text{Ge}_x$ and $\text{Si}_{1-y}\text{C}_y$ layers on silicon substrates. The author performed the whole processes except chemical vapor deposition (CVD) of $\text{Si}_{1-x}\text{Ge}_x$ and $\text{Si}_{1-y}\text{C}_y$ layers, characterization and manuscript writing.

Paper VII. This paper includes microfabrication of self-supported free standing $\text{La}_{1-x}(\text{Sr,Ca})_x\text{MnO}_3$ membrane pixels on Si by dry etching method with preannealed photoresist techniques. The author performed the all processing, characterization and manuscript writing.

Paper VIII. This paper reveals the wet etch rate and selectivity for $\text{La}_{0.67}(\text{Sr,Ca})_{0.33}\text{MnO}_3$ films on Si by potassium hydroxide (KOH) and buffered hydrofluoric (BHF). Electrical properties of KOH etched LSCMO were investigated by scanning spreading resistance microscopy (SSRM). The author performed the whole processes, characterization and manuscript writing.

Paper IX. This paper presents the etch rates for $\text{La}_{0.67}(\text{Sr,Ca})_{0.33}\text{MnO}_3$ on oxide buffered Si substrates using wet (= KOH and BHF) and dry (= Ar ion beam) etching methods. The author worked for all experiments, characterization and manuscript writing.

APPENDED PAPERS

Epitaxial colossal magnetoresistive $La_{0.67}(Sr,Ca)_{0.33}MnO_3$ films on Si

J.-H. Kim, S. I. Kharsev, and A. M. Grishin, Appl. Phys. Lett. **82**(24), 4295 (2003).

Epitaxial Colossal Magnetoresistive/Ferroelectric Heterostructures

A. M. Grishin, S. I. Kharsev, J.-H. Kim and Jun Lu, Integrated Ferroelectrics
67, 69 (2004).

Microfabricated heteroepitaxial oxide structures on silicon for bolometric arrays

J.-H. Kim, A. M. Grishin, NSTI Nanotech 2005 Proceedings, Vol. 3, 521 (2005).

Free standing epitaxial $\text{La}_{1-x}(\text{Sr,Ca})_x\text{MnO}_3$ membrane on Si for uncooled infrared microbolometer

*J.-H. Kim, A. M. Grishin, *Appl. Phys. Lett.* **87**, 033502 (2005).*

Integration of colossal magnetoresistors with GaAs

S. I. Kharsev, J.-H. Kim and A. M. Grishin, J. Crystal Growth 284, 1-5 (2005).

The effect of strained $\text{Si}_{1-x}\text{Ge}_x$ and $\text{Si}_{1-y}\text{C}_y$ layers for $\text{La}_{0.75}\text{Sr}_{0.25}\text{MnO}_3$ films grown on oxide-buffered Si substrates

J.-H. Kim, A. M. Grishin, H. H. Radamson, will be published in J. Appl. Phys.

Microfabrication of epitaxial $\text{La}_{1-x}(\text{Sr,Ca})_x\text{MnO}_3$ IR bolometer on Si
Joo-Hyung Kim, Alexander M. Grishin, will be published in Integrated
Ferroelectrics (2005).

Wet etching study of $\text{La}_{0.67}(\text{Sr}_{0.5}\text{Ca}_{0.5})_{0.33}\text{MnO}_3$ films on silicon substrates
Joo-Hyung Kim, Alexander M. Grishin, submitted to J. Microelectromech.
Systems (2005).

Wet and dry etching of $\text{La}_{0.67}(\text{Sr,Ca})_{0.33}\text{MnO}_3$ films on Si
Joo-Hyung Kim and Alexander M. Grishin, submitted to Thin Solid Films
(2005).